# Study of glass resistive plate chambers for the INO-ICAL detector

By

**Raveendrababu Karnam**

**PHYS01201004019**

**Bhabha Atomic Research Centre, Mumbai - 400 085**

*A thesis submitted to the*

*Board of Studies in Physical Sciences*

*In partial fulfillment of requirements*

*for the Degree of*

**DOCTOR OF PHILOSOPHY**

*of*

**HOMI BHABHA NATIONAL INSTITUTE**



**October, 2016**

# Homi Bhabha National Institute

## Recommendations of the Viva Voce Committee

As members of the Viva Voce Committee, we certify that we have read the dissertation prepared by Raveendrababu Karnam entitled "Study of glass resistive plate chambers for the INO-ICAL detector" and recommend that it may be accepted as fulfilling the thesis requirement for the award of Degree of Doctor of Philosophy.

_____ Date: 24.3.17
Chairperson - Prof. D. Indumathi

_____ Date: 24.3.17
Guide/Convener - Prof. Prafulla Kumar Behera

_____ Date: 24-3-2017
Examiner - Prof. Gagan B. Mohanty

_____ Date: 24/3/2017
Member 1 - Prof. Jim Libby

_____ Date: 24/3/2017
Member 2 - Prof. Nagendra Krishnapura

---

Final approval and acceptance of this dissertation is contingent upon the candidate's submission of the final copies of the dissertation to HBNI.

I hereby certify that I have read this dissertation prepared under my direction and recommend that it may be accepted as fulfilling the dissertation requirement.

**Date:** 24.3.17

**Place:** Chennai

_____
**Prof. Prafulla Kumar Behera**

iii

# Statement by Author

This dissertation has been submitted in partial fulfillment of requirements for an advanced degree at Homi Bhabha National Institute (HBNI) and is deposited in the Library to be made available to borrowers under rules of the HBNI.

Brief quotations from this dissertation are allowable without special permission, provided that accurate acknowledgement of source is made. Requests for permission for extended quotation from or reproduction of this manuscript in whole or in part may be granted by the Competent Authority of HBNI when in his or her judgement the proposed use of the material is in the interests of scholarship. In all other instances, however, permission must be obtained from the author.

*K. Raveendrababu*

Raveendrababu Karnam

**Date:** 24|03|2017

**Place:** Chennai

# Declaration

I, hereby declare that the investigation presented in the thesis has been carried out by me. The work is original and has not been submitted eralier as a whole or in part for a degree/diploma at this or any other Institution/University.

*K. Raveendrababu*

Raveendrababu Karnam

Date: 24|03|2017

Place: Chennai

# List of publications arising from the thesis

## Journal

1. **K. Raveendrababu**, P.K. Behera and B. Satyanarayana, "Effect of electrical properties of glass electrodes on the performance of RPC detectors for the INO-ICAL experiment", *JINST* 11 (2016) P08024.

2. **K. Raveendrababu**, P.K. Behera, B. Satyanarayana, S. Mukhopadhyay, and N. Majumdar, "Effect of water vapor on the performance of glass RPCs in avalanche mode operation", *JINST* 11 (2016) C08001.

3. **K. Raveendrababu**, P.K. Behera, B. Satyanarayana and Jafar Sadiq, "Study of glass properties as electrode for RPC", *JINST* 11 (2016) C07007.

4. J. Sadiq, **K. Raveendrababu** and P.K. Behera, "Effect of glass thickness variations on the performance of RPC detectors", *JINST* 11 (2016) C10003.

## Conference proceedings

1. **K. Raveendrababu**, P.K. Behera and B. Satyanarayana, "Glass RPC and Its Electrode Characterization", Springer Proceedings in Physics 174, DOI 10.1007/978-3-319-25619-1_57.

2. **K. Raveendrababu**, P.K. Behera, "Gas proportion studies on the operation of resistive plate chambers". The proceedings are submitted to the European Physics Journal C through XXII DAE-BRNS Symposium 2016.

## Others

1. ICAL collaboration, Shakeel Ahmed et al., "Physics Potential of the ICAL detector at the India-based Neutrino Observatory (INO)", arXiv:1505.07380v1.

2. **K. Raveendrababu** et al., "Development of RPC characterization facility". The manuscript is under preparation.


K. Raveendrababu

Raveendrababu Karnam

# Dedicated to

**A. C. Bhaktivedanta Swami Prabhupada**

**&**

**My Sweet Mom.....**

# Acknowledgements

# Contents

# Synopsis

## 0.1 Introduction

The India-based Neutrino Observatory (INO) collaboration has proposed to build a 50 kiloton magnetized Iron Calorimeter (ICAL). The main aims of this experiment are to precisely measure the neutrino oscillation parameter $\theta_{23}$ and determine the sign of mass-squared difference $\Delta m_{32}^2$ using Earth's atmospheric neutrino oscillation data. The ICAL detector will comprise of three modules of $16 \times 16 \times 14.5$ m$^3$. Each module consists of a stack of 151 horizontal layers of 5.6 cm thick iron plates interleaved with 4 cm gaps to house the active detector layers. The collaboration has chosen glass Resistive Plate Chambers (RPCs) of $2 \times 2$ m$^2$ size as the active elements. The ICAL detector is going to use 28,800 such RPCs. The iron plates are magnetized with an average magnetic field of 1.5 T. Therefore, the ICAL can detect the atmospheric neutrinos and antineutrinos separately. The experiment is expected to run for more than 10 years in order to record statistically significant number of neutrino interactions to measure the neutrino mass hierarchy. Therefore, long-term stability and performance of the RPCs over the duration of the experiment are of prime concern.

## 0.2 Resistive plate chamber

Resistive plate chamber (RPC) was first developed by R. Santonico and R. Cardarelli in 1981 [1]. The RPC electrodes are made out of a high resistive material (typically, bakelite or float glass), with a bulk resistivity of $10^{10}$ –$10^{12}$ $\Omega$.cm. The RPCs are parallel plate gaseous detectors, which work on the ionization principle. They are simple to construct, offer two-dimensional readout, provide good efficiency (>95%) and excellent time ($\sim$ps) as well as position ($\sim \mu$m) resolutions. Therefore, they are used as the trigger and/or timing detectors in many high-energy physics experiments.

The basic construction scheme of an RPC is shown in figure 1.

The outer surfaces of RPC electrodes are is coated with a semi-resistive paint, which facilitated applying high voltage across the electrodes. The electrodes are separated by a few millimeters using poly-carbonate spacers to maintain a uniform gap between the two electrodes. The electrodes are applied with high voltages $\sim$10 kV in order to create a uniform electric field in the gap. Conductive readout-strips are orthogonally mounted on the external surfaces of the gap. The electrodes and the readout-strips are separated using a layer of mylar insulator.

An optimized gas mixture of Ar/$C_2H_2F_4$/iso-$C_4H_{10}$ = 30/62/8 or $C_2H_2F_4$/iso-$C_4H_{10}$/$SF_6$ = 95.2/4.5/0.3 is flown through the RPC gap, depending on either streamer or avalanche mode of operation, respectively. When a charged particle passes through the gas gap, it produces the free charge carriers. These free charge carriers multiply into an avalanche under the influence of strong electric field in the gap, propagate toward the electrodes and induce charge on the external readout-strips. Since the readout-strips are orthogonally placed on either side of the gas gap, we get the (x, y) coordinates of the particle using the same active detector volume.
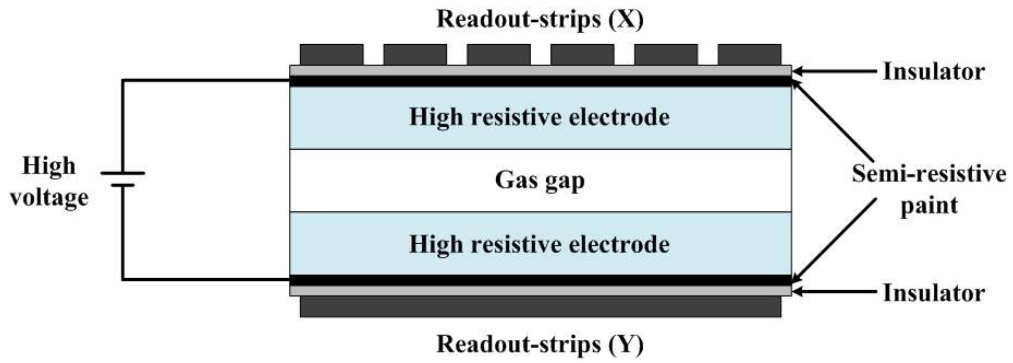


**Figure 1:** Schematic of a Resistive Plate Chamber.

## 0.3 Glass electrode material study for RPCs

Operation and performance of the RPCs mostly depend on the quality and characteristics of the electrode materials. Since the INO collaboration is going to deploy the RPCs for the ICAL detector in an unprecedented scale, it is imperative to study the electrode material aspects in detail. The

collaboration has proposed to use glasses from Asahi and/or Saint-Gobain for producing the RPCs. Therefore, in this thesis the systematic material property studies on the glasses from these two manufacturers were undertaken. The RPCs built using these glasses and their performances were compared with the material properties [51, 72].

## 0.3.1 Surface roughness

The inner surface of the electrode that is facing the gas volume should be as smooth as possible, so that the field emission of electrons from cathode can be minimized [4]. These emitted electrons increase dark current and singles rate of the RPC and thereby deteriorating its performance. Therefore, the surface resistivity of glasses from Asahi and Saint-Gobain was measured using BRUKER ContourGT Optical Microscope. Both the glasses showed identical surface roughness on their smoother sides as shown in figure 2. Therefore, it can be expected that the contribution of dark current due to the field emission of electrons would be identical for the RPCs made from these glass electrodes.



(a) Asahi side-1; Rq = 0.79 nm          (b) Asahi side-2; Rq = 1.28 nm

(c) Saint-Gobain side-1; Rq = 0.93 nm   (d) Saint-Gobain side-2; Rq = 1.97 nm
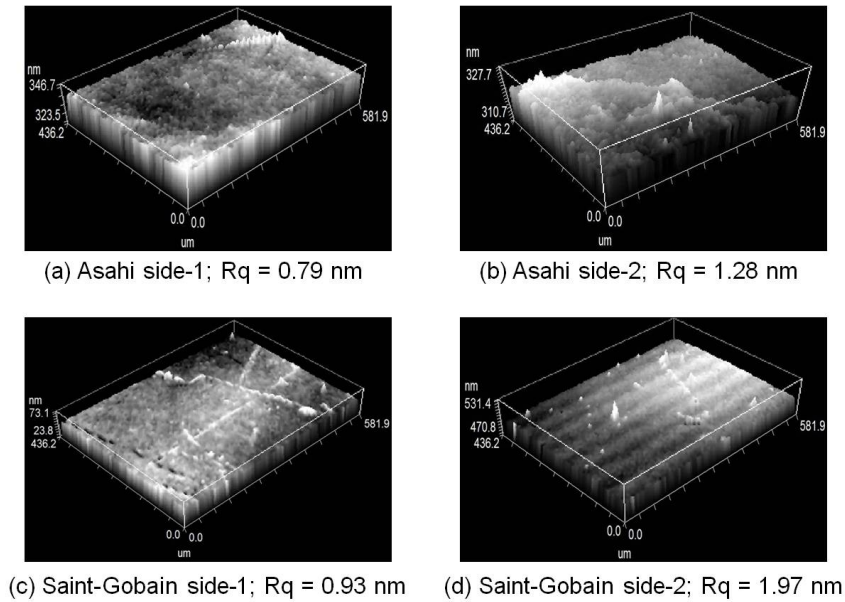
**Figure 2:** Surface roughness measurements of the glasses using BRUKER ContourGT Optical Microscope. Size of each scan is 582 $\mu$m $\times$ 436 $\mu$m.

## 0.3.2 Density

The density of glass plays a role in the weight of RPC detector. The mammoth ICAL detector uses RPCs in an unprecedented scale as the active detector elements. Therefore, the density of glasses was measured using METTLER-AE163 laboratory weighing balance. The measurements were taken on three samples from each manufacturer and the results were averaged out. These results are given in table 1.

**Table 1:** Density measurements of Asahi and Saint-Gobain glasses. $\sigma_d$ is the standard deviation on average density of the glasses.

| Manufacturer | Density (g/cc) | $\sigma_d$ ($\times 10^{-2}$ g/cc) |
|:---:|:---:|:---:|
| Asahi | 2.4996 | 0.85 |
| Saint-Gobain | 2.4963 | 0.72 |

## 0.3.3 Bulk resistivity

The bulk resistivity of glasses was measured using Agilent Technologies B1500A Semiconductor Device Analyzer equipped with B1511B Medium power source/monitor unit. The measurements were taken on three samples from each manufacturer and the results were averaged out. The results are given in table 2. The standard deviation ($\sigma_b$) on the average bulk resistivities of glasses are also given in the table. Asahi glass showed larger bulk resistivity compared to Saint-Gobain glass.

**Table 2:** Bulk resistivity of the glasses.

| Manufacturer | Bulk resistivity ($\times 10^{12}$ $\Omega$.cm) | $\sigma_b$ ($\times 10^{12}$ $\Omega$.cm) |
|:---:|:---:|:---:|
| Asahi | 4.73 | 0.05 |
| Saint-Gobain | 3.65 | 0.17 |

## 0.3.4  Relative permittivity

The relative permittivity of glasses was measured using Novocontrol Broadband Dielectric/Impedance Spectrometer at 20 °C. The results are shown in figure 3. Asahi glass showed larger relative permittivity compared to Saint-Gobain glass. The investigations were made to understand the reason for this difference. From the elemental composition measurements summarized in table 3, it was observed that Asahi glass is having larger amount of sodium (Na) component ($\sim$2%) compared to Saint-Gobain glass. In glass, the presence of sodium in $Si - O - Na$ structure increases the electronic polarizability of oxygen ions and ionic polarizability of sodium ions, which leads to increase of the electric permittivity of glass in an applied electric field [5].
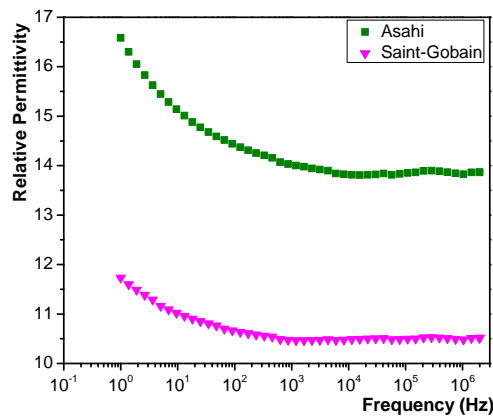


**Figure 3:** Relative permittivities of Asahi and Saint-Gobain glasses using Novocontrol Dielectric/Impedance Spectrometer.

# 0.4  Development and characterization of RPCs

Several numbers of RPCs of $30 \times 30$ cm$^2$ size were built using Asahi and Saint-Gobain glass plates. The outer surfaces of the plates were coated with specially developed conductive graphite paint for the ICAL RPCs [6]. The surface resistance of electrodes maintained to be uniform at $\sim$1 M$\Omega$/$\square$. The electrodes were separated 0.2 cm by means of polycarbonate spacers and gas nozzles.

**Table 3:** Summary of various elemental compositions of glass samples in fractional atomic percentages (%). $\sigma_A$ is the calculated standard deviation for each element of Asahi glass and $\sigma_S$ is that of Saint-Gobain glass.

| Element | Asahi (%) | $\sigma_A$ (%) | Saint-Gobain (%) | $\sigma_S$ (%) |
|---|---|---|---|---|
| Oxygen (O) | 69.96 | 00.75 | 71.40 | 00.60 |
| Silicon (Si) | 15.89 | 00.44 | 16.62 | 00.45 |
| Sodium (Na) | 10.59 | 00.16 | 08.48 | 00.16 |
| Magnesium (Mg) | 02.34 | 00.12 | 02.18 | 00.10 |
| Calcium (Ca) | 00.69 | 00.12 | 00.75 | 00.09 |
| Aluminium (Al) | 00.49 | 00.09 | 00.59 | 00.13 |
| Iron (Fe) | 00.04 | 00.01 | 00.04 | 00.02 |

The bulk resistivity of spacers and gas nozzles is greater than $10^{13}\Omega$.cm [7]. The electrodes, spacers and gas nozzles were assembled with 3M Scotch-Weld DP190 Epoxy Adhesive to isolate the detector volume from the ambient environmental conditions. Readout-strips of 2.8 cm wide with 0.2 cm gap between the consecutive strips were orthogonally mounted on the external surfaces of RPCs. A layer of mylar sheet was inserted between the electrode and the readout-strips. The gas gaps made out of Asahi glass and Saint-Gobain glass were named as A-RPCs and S-RPCs, respectively. A gas mixture of $C_2H_2F_4$/iso-$C_4H_{10}$/$SF_6$ = 95/4.5/0.5 was flown through the RPCs with a total flow rate of 10 SCCM and operated in the avalanche mode. All the RPCs were operated under identical environmental conditions.

## 0.4.1  Experimental setup

A cosmic ray muon telescope was set up with three plastic scintillator counters (cosmic-ray paddles) to get a 3-fold coincidence. The dimensions of scintillator counters in length $\times$ width $\times$

thickness are $30 \times 2 \times 1$ cm$^3$ (top), $30 \times 3 \times 1$ cm$^3$ (middle) and $30 \times 5 \times 1$ cm$^3$ (bottom). The RPCs were stacked between top and middle scintillator counters. The telescope window that is defined by a 2 cm wide finger paddle was centered on the 2.8 cm wide central strip of the RPC. The detailed experimental arrangement of RPCs, scintillator counters and electronic circuit is shown in figure 4.

**Figure 4:** Schematic diagram of the experimental arrangement for characterizing the RPCs.

### 0.4.2 Test results

**Voltage-current characteristics**

The RPCs from Asahi and Saint-Gobain glass electrodes were built with the identical spacers. Therefore for a given bulk resistivity of the spacers, the current flowing in the circuit depends on the bulk resistivity of RPC electrodes. The voltage-current characteristics of RPCs were measured using C.A.E.N Mod. N471A, 2 channel HV Power Supply. The current resolution of module is 1 nA. The currents drawn by RPCs as a function of applied voltage are shown in figure 5. A- RPCs

were found to draw lower bias currents compared to S-RPCs. This could be because of Asahi glass showed larger bulk resistivity compared to Saint-Gobain glass (table 2).



**Figure 5:** Currents drawn by the RPCs as a function of voltage.

**Efficiency studies**

The normal vector component of electric field displacement is continuous at the electrode/gas interface of RPC. This boundary condition is expressed as:

$$\mathbf{D} = \varepsilon_p \mathbf{E_p} = \varepsilon_g \mathbf{E_g}, \tag{1}$$

where, $\varepsilon_p$ and $\varepsilon_g$ are the permittivities, and $\mathbf{E_p}$ and $\mathbf{E_g}$ are the electric fields of the electrode plate and the gas gap, respectively [8]. Equation 1 indicates that the RPCs made out of electrodes with larger relative permittivity can be operated at lower bias voltages.

The efficiencies of RPCs were measured using the cosmic-ray muons. The experimental arrangement for measuring the efficiencies of RPCs is shown in figure 4. The measurements on RPCs were performed using C.A.E.N Mod. V830 Scaler. The telescope trigger pulse was recorded as 3-fold pulse. The efficiency is defined as the ratio of the number of coincident pulses of RPC strip with that telescope trigger (i.e., 4-fold pulses) to the number of trigger pulses (3-fold pulses). This definition is written as:

$$\text{Efficiency} = \frac{\text{4-fold (4F) rate}}{\text{3-fold (3F) rate}} \times 100\%, \tag{2}$$

where, 3F is the telescope trigger pulse, which is generated by time coincidence of three scintillator counters, and 4F is the coincidence pulse of the RPC under test and the telescope trigger pulse.

The measured efficiencies of RPCs as a function of applied high voltage are shown in figure 6. The four RPCs showed greater than 95% efficiencies on the plateau. It is observed that the knee of efficiency plateau of A-RPCs starts at 10.8 kV, whereas that of S-RPCs starts at 12.0 kV. Therefore, A-RPCs can be operated at 1.2 kV lower bias voltage in comparison to S-RPCs. These results are in consistent with equation 1.
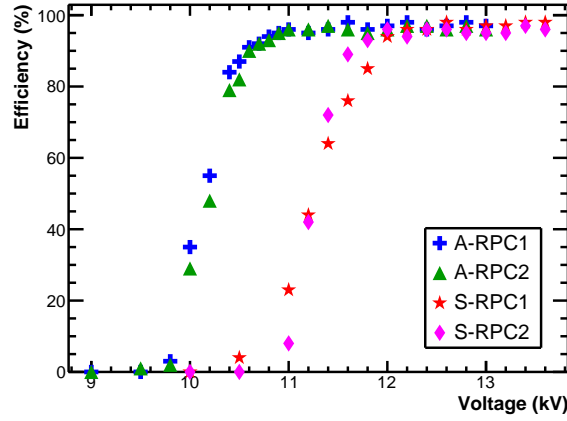


**Figure 6:** Efficiencies of the RPCs as a function of high voltage.

**Time resolution of the RPCs**

From equation 1, it is understood that for a given applied voltage the RPC made out of electrodes with larger relative permittivity will generate a larger electric field in the gas gap. Therefore, the drift velocity of avalanche electrons will be higher, which leads to better time resolutions [9, 10]. The RPCs were operated at 12.0 kV, where they showed greater than 95% efficiency, and measured their time resolutions. A-RPC1, A-RPC2 showed 1.8, 1.7 ns and both S-RPC1, S-RPC2 showed 2.3 ns time resolutions, respectively. These results are shown in figure 7.
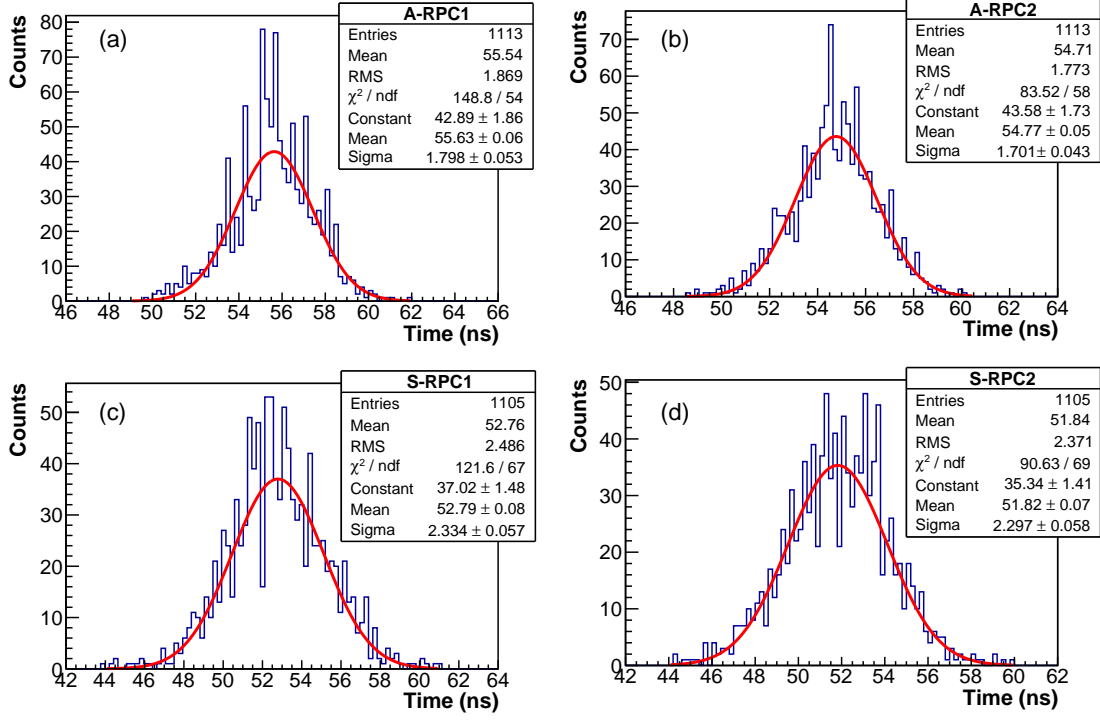
**Figure 7:** Time resolutions of the RPCs at 12 kV: (a), (b) A-RPCs; (c), (d) S-RPCs.

## 0.5 Effect of water vapor on the performance of glass RPCs

In the duration of INO-ICAL experiment, about 200,000 liters of gas is going to be circulating in the RPCs. The gas lines of about 135 km in total length are going to supply (receive) gas to (from) the RPC detectors. In spite of stringent QC during the RPC gas gap making or gas lines plumbing, it is impossible to prevent ambient air or water vapor entering into the gas circuit over these long periods of time. The contaminants are known cause for serious degradation in the performance or permanent damage of the RPCs [11, 12].

Considering the possibility of severe repercussions in the mammoth ICAL detector, a systematic study of this problem was undertaken [95]. Two glass RPCs of $30 \times 30$ cm$^2$ size were simultaneously operated with standard gas mixture in one and with gas mixture along with controlled amount of water vapor in the other. A common cosmic ray muon telescope was set up for studying both the RPCs. Ambient parameters such as temperature and relative humidity (RH) as well as RPCs operating and performance parameters for cosmic ray muon detection were system-

atically recorded throughout the experiment. It was observed that significant deterioration occurs in the performance of RPC in which gas with water vapor was flown. The results are summarized as following.

## 0.5.1 Standard gas studies

The RPCs were operated with standard gas at 10 SCCM flow rate and their currents, efficiencies and singles rates as a function of applied voltage were measured for 32 days. The results are shown in figure 8. At an operating voltage of 12.2 kV, the signal charges of RPC1 and RPC2 were found to be 0.99 pC and 1.24 pC, and the time resolutions were 2.8 ns and 2.3 ns, respectively.
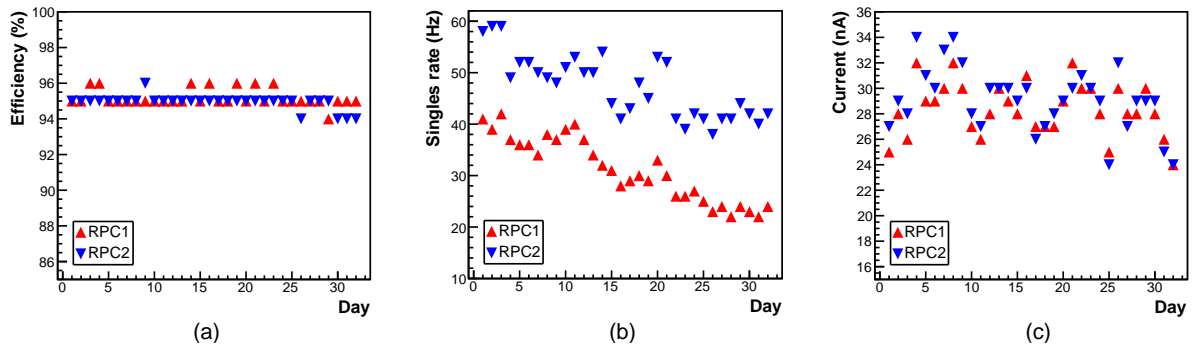


**Figure 8:** (a) Efficiency, (b) singles rate and (c) current of both the RPCs with the standard gas operation for 32 days.

## 0.5.2 Wet gas studies

The water vapor was added to RPC1 gas mixture using a water bubbler. With this wet gas operation for a few days, the efficiency and singles rate of RPC1 degraded to 0% and 1 Hz, respectively. The currents drawn by the detector increased gradually with time. The efficiency, singles rate and current drawn by the RPC1 during the wet gas operation in comparison to RPC2 operated with the standard gas are shown in figure 9. With the wet gas operation, the signal charge and timing distribution of RPC1 got deteriorated.
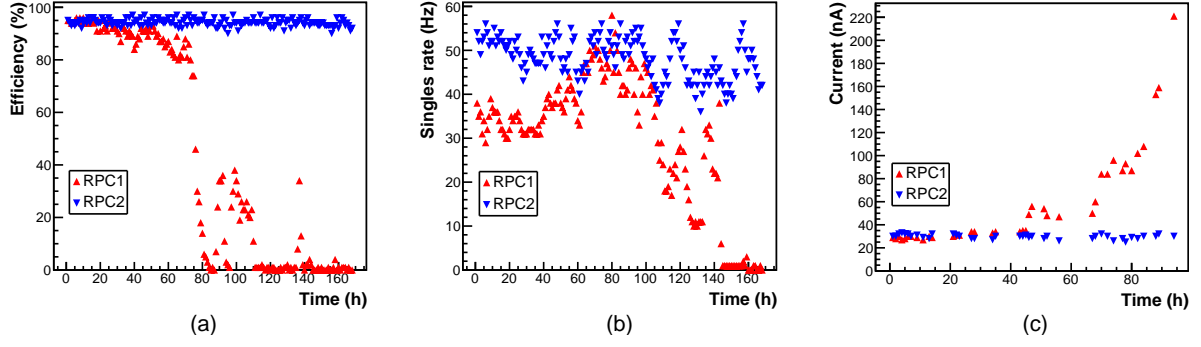
**Figure 9:** (a) Efficiency, (b) singles rate and (c) current of RPC1 with the wet gas operation and those of RPC2 with the standard gas operation.

### 0.5.3 Recovery studies

The RPC1 was operated with wet gas at various flow rates and the deterioration in the detector's efficiency was observed as a function of time. It was observed that the higher the flow rate, faster the RPC's deterioration as shown in figure 10a. The detector was operated with wet gas at 0% efficiency for a day and then switched to standard gas. Then, the efficiency of detector recovered to greater than 95% in less than an hour as shown in figure 10b.
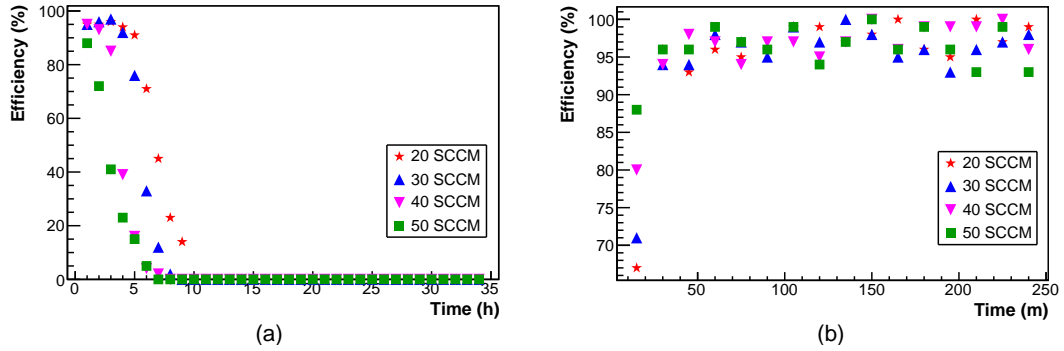


**Figure 10:** (a) Deterioration in efficiency of RPC1 with wet gas operation at various flow rates and (b) its recovery with standard gas operation.

## 0.6 Response of the ICAL geometry to muons

For the ICAL detector, the INO collaboration has proposed two geometries 1) default, where the dead space, due to the support structures in the detector volume, is localized to the neutrino event

and 2) staggered, where the support structure is redistributed throughout the volume. The ICAL detector performance studies were carried out for the optimization parameters for different zenith angles of muons using both the geometries with Geant4-based simulation data. The CERN-ROOT framework was used to analyze the simulated data. The results are summarized as following.

## 0.6.1 Momentum reconstruction efficiency

The momentum reconstruction efficiencies for $\mu^-$ events of $1 - 25$ GeV momentum regime were computed using both the geometries. The histograms of reconstructed momentum were plotted for the events with the quality of fit such that $\chi^2/\text{ndf} < 5$. This quality was obtained by fitting histograms for $5\sigma$ data. The analysis was performed for the zenith angles $\cos\theta = 0.65$, $0.85$ and $0.95$. The comparison studies of momentum reconstruction efficiencies for $\mu^-$s using the default and staggered geometries are shown in figure 11.
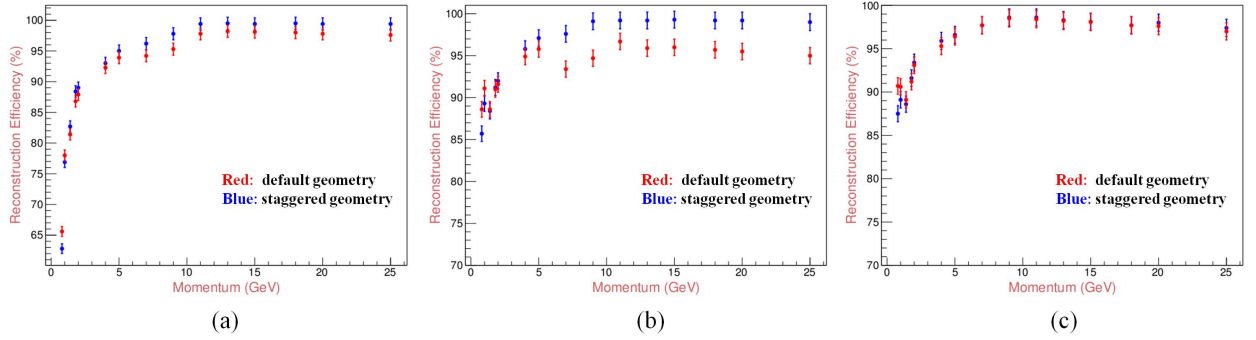


**Figure 11:** Comparison of the momentum reconstruction efficiencies for $\mu^-$s using default and staggered geometries of the ICAL detector. The results are for the zenith angles (a) $\cos\theta = 0.65$, (b) $\cos\theta = 0.85$ and (c) $\cos\theta = 0.95$.

## 0.6.2 Relative charge identification efficiency

The Kalman filter enabled in Geant4-based INO-ICAL code may mis-identify the muon charge ($\mu^-$ as $\mu^+$ or $\mu^+$ as $\mu^-$) and therefore results in the wrong charge identification. The comparison of charge identification efficiencies of the ICAL detector for the two proposed geometries was studied. The results are shown in figure 12.
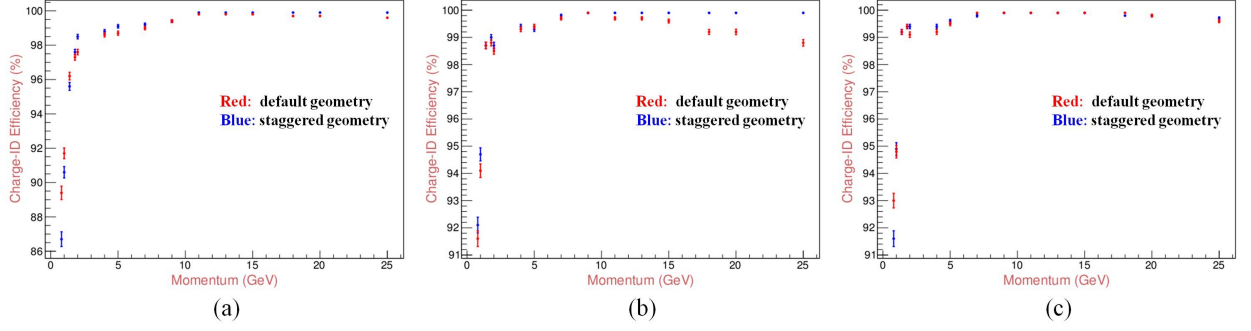
**Figure 12:** Comparison studies of the relative charge identification efficiencies for $\mu^-$s using the default and staggered geometries of the ICAL detector. The results are for the zenith angles (a) $\cos\theta = 0.65$, (b) $\cos\theta = 0.85$ and (c) $\cos\theta = 0.95$.

### 0.6.3 Muon momentum resolution

The comparison studies of the muon momentum resolutions for $\mu^-$s using the default and staggered geometries are shown in figure 13. The analysis was performed for the zenith angles $\cos\theta$ = 0.65, 0.85 and 0.95. The detector showed best momentum resolutions for 7 GeV $\mu^-$s. The staggered geometry showed better momentum resolutions compared to default geometry.
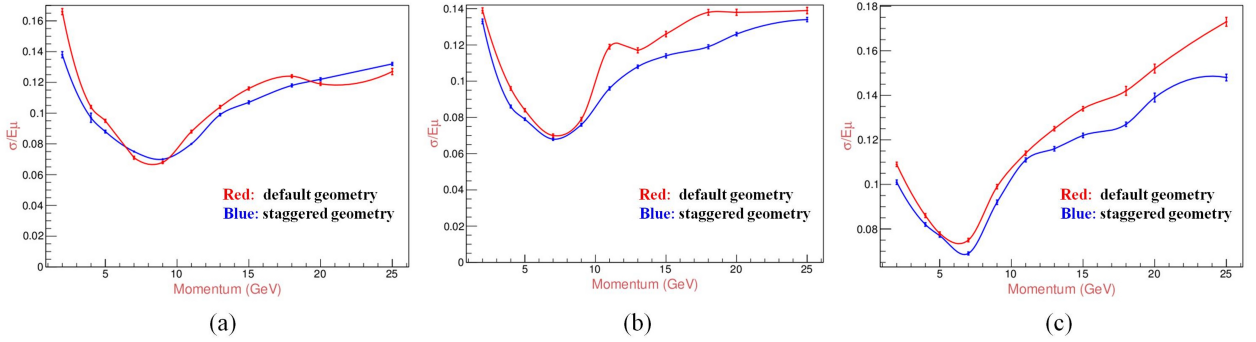


**Figure 13:** Comparison studies of the muon momentum resolutions for $\mu^-$s using the default and staggered geometries of the ICAL detector. The results are for the zenith angles (a) $\cos\theta = 0.65$, (b) $\cos\theta = 0.85$ and (c) $\cos\theta = 0.95$.

### 0.6.4 Zenith angle resolution

The analysis was performed for the zenith angles $\cos\theta = 0.65, 0.85$ and $0.95$. The comparison studies of the zenith angle resolutions for $\mu^-$s using the default and staggered geometries are shown in

figure 14. It was observed that both the geometries showed identical zenith angle resolutions for $\mu^-$s.
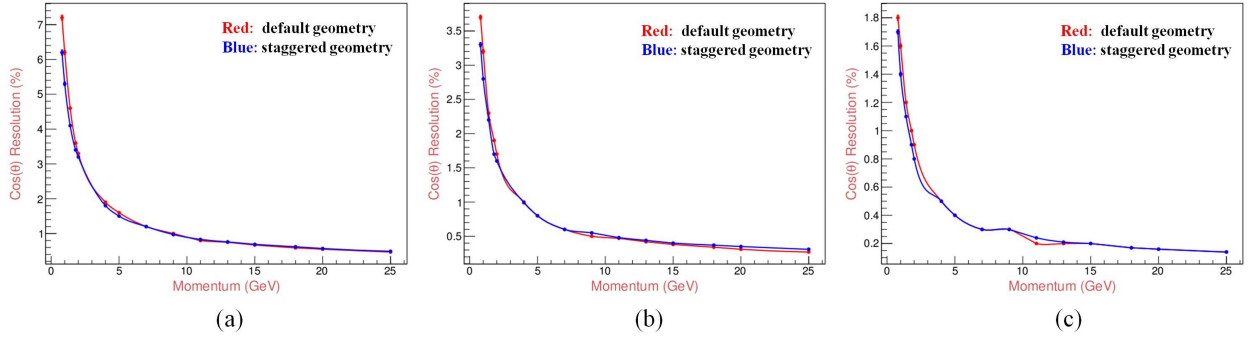


**Figure 14:** Comparison studies of the zenith angle resolutions for $\mu^-$s using the default and staggered geometries of the ICAL detector. The results are for the zenith angles (a) $\cos\theta = 0.65$, (b) $\cos\theta = 0.85$ and (c) $\cos\theta = 0.95$.

## 0.7   Summary

The various material property characterization studies were performed on the glasses from Asahi and Saint-Gobain manufacturers as RPC electrodes for the INO-ICAL experiment. Asahi glass showed $\sim$2% larger sodium component than Saint-Gobain glass. This could be the reason for larger relative permittivity of Asahi glass. The RPCs built using these glasses and their performances were compared with the material properties. The Asahi RPCs were found to draw lower bias currents compared to Saint-Gobain RPCs. The knees of efficiency plateau of Asahi and Saint-Gobain RPCs were started at 10.8 kV and 12 kV, respectively. At a given high voltage, the Asahi RPCs showed better time resolutions compared to Saint-Gobain RPCs. Therefore, a qualitative agreement in the comparisons of RPCs performances to material properties of glasses was observed.

The effect of water vapor on the performance of glass RPCs in the avalanche mode operation was studied. The RPC's efficiency decreased to 0% after a few days with wet gas operation. Its signal charge decreased and timing distribution deteriorated. The RPC was operated at 0%

efficiency with the wet gas for a day and then switched to standard gas, recovering an efficiency greater than 95%. Therefore, it indicates that no damages occurred to the inner surfaces of RPC electrodes.

The response of ICAL geometry to muons was studied for the default and staggered geometries. The staggered geometry showed 2% better momentum resolution and 4% larger reconstruction efficiency at larger muon energies compared to default geometry.

# Bibliography

[1] R. Santonico and R. Cardarelli, Development of Resistive Plate Counters, *Nucl. Instrum. and Meth.* 187 (1981) 377.

[2] K. Raveendrababu, P.K. Behera, B. Satyanarayana and J. Sadiq, Study of glass properties as electrode for RPC, *JINST* 11 (2016) C07007.

[3] K. Raveendrababu, P.K. Behera and B. Satyanarayana, Effect of electrical properties of glass electrodes on the performance of RPC detectors for the INO-ICAL experiment, *JINST* 11 (2016) P08024.

[4] Changguo Lu, RPC electrode material study, *Nucl. Instr. and Meth. A* 602 (2009) 761.

[5] C. H. Hsieh et al., Correlation between dielectric constant and chemical structure of sodium silicate glasses, *J. Appl. Phys.* 80 (1996) 1704.

[6] M. Bhuyan et al., Development of 2 m $\times$ 2 m size glass RPCs for INO, *Nucl. Instrum. and Meth. A* 661 (2012) S64.

[7] B. Satyanarayana, Design and Characterisation Studies of Resistive Plate Chambers, Ph.D Thesis (2009).

[8] M. Morales et al., Conductivity and charge depletion aging of resistive electrodes for high rate RPCs, *JINST* 8 (2013) P01022.

[9] W. Riegler and C. Lippmann, Detailed models for timing and efficiency in resistive plate chambers, *Nucl. Instrum. and Meth. A* 508 (2003) 14.

[10] Tapasi Ghosh and Subhasis Chattopadhyay, A Monte Carlo simulation to study the effect of surface roughness on the performance of RPC, *Nucl. Instrum. and Meth. A* 661 (2012) S177.

[11] H. Sakai et al., Study of the effect of water vapor on a resistive plate chamber with glass electrodes, *Nucl. Instrum. and Meth. A* 484 (2002) 153.

[12] T. Kubo et al., Study of the effect of water vapor on a glass RPC with and without freon, *Nucl. Instrum. and Meth. A* 508 (2003) 50.

[13] K. Raveendrababu, P.K. Behera, B. Satyanarayana, S. Mukhopadhayay and N. Majumdar, Effect of water vapor on the performance of glass RPCs in avalanche mode operation, *JINST* 11 (2016) C08001.

# List of Figures

# List of Tables

# Full form of the abbreviations used in the thesis

fm              Fermi

CERN            The European Organization for Nuclear Research

SLAC            Stanford Linear Accelerator Center

SPEAR           Stanford Positron Electron Asymmetric Rings

LBNL            Lawrence Berkeley National Laboratory

NOνA            NuMI Off-Axis $\nu_e$ Appearance Experiment

LBNO            Long Baseline Neutrino Observatory

PINGU           The Precision IceCube Next Generation Upgrade Experiment

ORCA            Oscillation Research with Cosmics in the Abyss

JUNO            The Jiangmen Underground Neutrino Observatory

RENO-50         Reactor Experiment for Neutrino Oscillation-50

HK              The Hyper-Kamiokande Experiment

T2HK            The Tokai to Hyper-Kamiokande Project

ALICE           A Large Ion Collider Experiment

ATLAS           A Toroidal LHC ApparatuS

CMS             The Compact Muon Solenoid

STAR            Solenoidal Tracker at RHIC

RHIC            Relativistic Heavy Ion Collider

BESIII          Beijing Spectrometer III

BEPC II         Beijing Electron-Positron Collider II

NIM             Nuclear Instrumentation Module

CAMAC           Computer Automated Measurement And Control

# Chapter 1

# Introduction

## 1.1 The Standard Model: A brief summary

The Standard Model describes the theory of elementary constituents of matter and forces that act between them (excluding gravitation) [1, 2]. The known elementary building blocks of the standard model are quarks, leptons, antiparticles of quarks and leptons, and force carriers of the fundamental interactions between these particles. The force carriers are called as the gauge bosons. The Standard Model is a gauge theory based on the local symmetry group $SU(3)_C \times SU(2)_L \times U(1)_Y$, where the subscripts $C$, $L$ and $Y$ indicate color, left-handed chirality and weak hypercharge, respectively. The gauge group uniquely determines the interactions and the number of vector gauge bosons that correspond to the generators of the group. They are eight massless gluons, corresponding to the eight generators of $SU(3)_C$, that mediate strong interactions; four gauge bosons, of which three are massive ($W^\pm$ and Z) and one is massless ($\gamma$, the photon), corresponding to the three generators of $SU(2)_L$ and one generator of $U(1)_Y$, responsible for electroweak interactions [3]. The building blocks of the standard model and some of their quantum numbers are summarized in table 1.1. The quarks and leptons are grouped into three generations of four particles each. Between generations, particles differ by their flavor quantum number and mass, but their interactions are identical.

**Table 1.1:** Building blocks of the standard model and some of their quantum numbers. The spin is given in units of $\hbar$ and the charge is given in units of elementary charge $e$. The antiparticles of quarks and leptons have the quantum numbers B, L and Q with opposite sign [4, 5].

| Category | Particle | Mass (MeV/c$^2$) | Spin | Baryon number (B) | Lepton number (L) | Charge (Q) |
|---|---|---|---|---|---|---|
| Quarks | $u$ | $1.5 - 4$ | $\frac{1}{2}$ | $\frac{1}{3}$ | 0 | $+\frac{2}{3}$ |
| | $d$ | $4 - 8$ | $\frac{1}{2}$ | $\frac{1}{3}$ | 0 | $-\frac{1}{3}$ |
| | $c$ | $(1.15 - 1.35) \times 10^3$ | $\frac{1}{2}$ | $\frac{1}{3}$ | 0 | $+\frac{2}{3}$ |
| | $s$ | $80 - 130$ | $\frac{1}{2}$ | $\frac{1}{3}$ | 0 | $-\frac{1}{3}$ |
| | $t$ | $174.3 \pm 5.1 \times 10^3$ | $\frac{1}{2}$ | $\frac{1}{3}$ | 0 | $+\frac{2}{3}$ |
| | $b$ | $(4.1 - 4.4) \times 10^3$ | $\frac{1}{2}$ | $\frac{1}{3}$ | 0 | $-\frac{1}{3}$ |
| Leptons | $e$ | $0.511$ | $\frac{1}{2}$ | 0 | 1 | -1 |
| | $\mu$ | $105.7$ | $\frac{1}{2}$ | 0 | 1 | -1 |
| | $\tau$ | $1.777 \times 10^3$ | $\frac{1}{2}$ | 0 | 1 | -1 |
| | $\nu_e$ | $< 2.2 \times 10^{-6}$ | $\frac{1}{2}$ | 0 | 1 | 0 |
| | $\nu_\mu$ | $< 0.17$ | $\frac{1}{2}$ | 0 | 1 | 0 |
| | $\nu_\tau$ | $<15.5$ | $\frac{1}{2}$ | 0 | 1 | 0 |
| Gauge bosons (force carriers) | $g_i$ ($i = 1, 2, ...,8$ gluons) | 0 | 1 | 0 | 0 | 0 |
| | $\gamma$ (photon) | 0 | 1 | 0 | 0 | 0 |
| | W$^\pm$, Z (weak bosons) | $80.4 \times 10^3$, $91.2 \times 10^3$ | 1 | 0 | 0 | $\pm1, 0$ |

The typical interactions, force carriers and interaction properties of the elementary particles are given in table 1.2. Quarks participate in all the interactions, whereas leptons participate in all the interactions except strong interactions. Quarks are elementary components of hadrons but do not exist as free particles.

**Table 1.2:** Typical interaction properties of the elementary particles.

| Interaction | Participating particles | Force carrier | Charge | Range | Strength | Typical lifetime (sec) |
|---|---|---|---|---|---|---|
| Strong | Quarks | Gluon | Color | 1 fm | 10 | $10^{-23}$ |
| Electromagnetic | All charged particles | $\gamma$ (photon) | Electric charge (e) | $\infty$ | $10^{-2}$ | $10^{-20} \sim 10^{-16}$ |
| Weak | Quarks, Leptons | $W^{\pm}$, Z | Weak charge | $10^{-3}$ fm | $10^{-13}$ | $10^{-12}$ or longer |

The detailed list of elementary constituents of the standard model, some of their quantum numbers and their interaction proerties are summarized in figure 1.1 as well.

## 1.2 Gravity

The gravitational force is the most evident in everyday life. This is by far the weakest force known. As a result, it has no measurable effects on a subatomic scale and no manifestations that can guide to a quantum field theory. Therefore, the standard model could not adequately explain the gravity and is called as beyond standard model problem. Finally, On September 14, 2015 the gravitational-wave signals were observed at Advanced Laser Interferometer Gravitational-Wave Observatory (LIGO), USA [6].
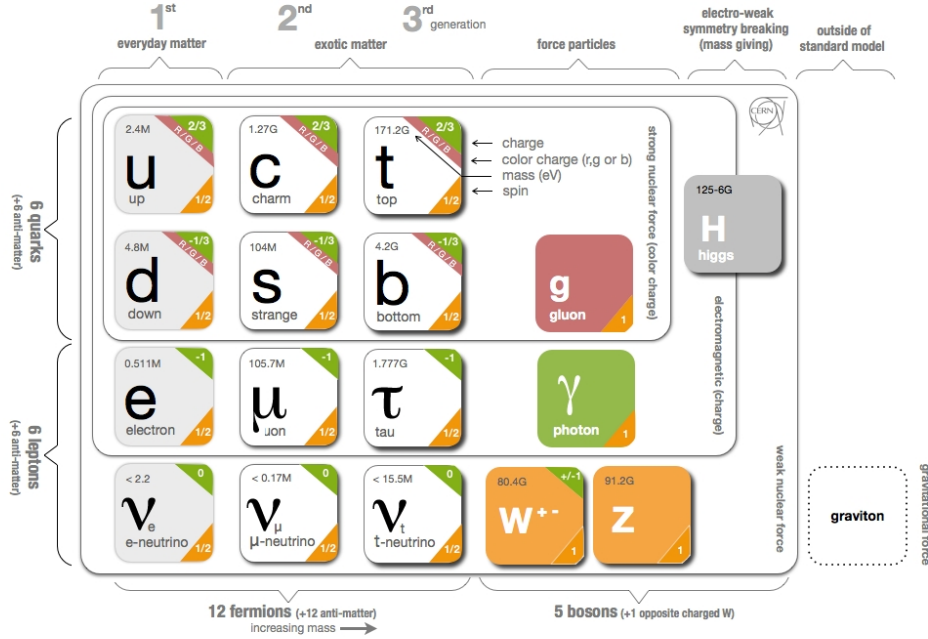
**Figure 1.1:** Standard model of the particle physics showing the electric charge, color charge, mass and spin of each particle [7].

## 1.3 Neutrino physics

### 1.3.1 A historical introduction

The history of neutrino started when in 1914 James Chadwick demonstrated that the $\beta$-spectrum was continuous, in contrast to $\alpha$ and $\gamma$ spectra that are discrete. The same result was subsequently confirmed in 1927 by Sir Charles Drummond Ellis and William Wooster. This led to the idea that the missing energy could be explained either by the existence of a new particle or, as proposed by Niels Bohr, abandoning of fundamental classical laws: conservation of energy and momentum.

In order to explain the continuous energy spectrum and spin statistics in $\beta$-decay, Wolfgang Pauli proposed a new particle, in a famous letter to a physics conference at Tubingen on 4 December 1930, addressed to *"Dear Radioactive Ladies and Gentlemen"*, that an additional neutral fermion, emitted along with the $\beta$-particle, might exist in the nucleus. He called the neutral fermion as neutron. In 1932, James Chadwick discovered the neutron as we know it today and later Enrico

Fermi renamed the Pauli particle the *neutrino* [3, 8].

By following the suggestion from Bruno Pontecorvo, Frederick Reines and Clyde Cowan conducted an experiment in 1953 at Savannah River reactor, USA and discovered the neutrino. The basic detection reaction was:

$$\overline{\nu}_e + p \longrightarrow e^+ + n, \tag{1.1}$$

where, $\overline{\nu}_e$ is electron antineutrino, $p$ is proton, $e^+$ is positron and $n$ is neutron. The detection principle was a coincident measurement of the 511 keV photons associated with positron annihilation and a neutron capture reaction a few $\mu$s later [3, 9, 10]. Again as suggested by Pontecorvo, in 1955 Raymond Davis, Jr. conducted an experiment in an attempt to induce the radiochemical reaction:

$$\overline{\nu}_e + {}^{37}Cl \longrightarrow e^- + {}^{37}Ar. \tag{1.2}$$

For this experiment, Davis used antineutrino source from Brookhaven reactor, USA. He could not observe this reaction and concluded that neutrinos and antineutrinos are not identical particles [3, 10, 11, 12]. Later in 1968, Davis and his collaborators used the same detection principle in a large scale version in the successful detection of solar neutrinos [3, 10, 12, 13]. The experiment was conducted at Homestake gold mine at South Dakota, USA. The detection reaction was:

$$\nu_e + {}^{37}Cl \longrightarrow e^- + {}^{37}Ar. \tag{1.3}$$

In 1959, Pontecorvo investigated whether the neutrino emitted in $\beta$-decay is the same as the one emitted in pion decay. If $\nu_\mu$ and $\nu_e$ are identical particles, then the reactions:

$$\nu_\mu + n \longrightarrow \mu^- + p, \tag{1.4}$$

$$\overline{\nu}_\mu + p \longrightarrow \mu^+ + n, \tag{1.5}$$

and

$$\nu_\mu + n \longrightarrow e^- + p, \tag{1.6}$$

$$\overline{\nu}_\mu + p \longrightarrow e^+ + n \tag{1.7}$$

should happen in the same rate, because the later could be done by $\nu_e$ and $\overline{\nu}_e$; otherwise the last two reactions should not be observed at all [10]. In 1960, M. Schwartz discussed about the use of high-energy accelerators as neutrino sources [14]. Then in 1962, G. Danby and his collaborators conducted an experiment at Brookhaven Alternating Gradient Synchrotron (AGS), USA using proton beam hitting a beryllium (Be) target. Due to this interaction secondary pions and kaons are generated, and their decay in flight produced an almost pure $\nu_\mu$ beam. This beam strikes through a thick iron wall and the interactions were observed in an aluminum spark chamber located behind the iron wall. In total, 29 muon-like (single tracks) and six electron-like (showers) events were observed in the chamber. The electron events were expected from $\nu_e$ beam contaminations due to kaon decays (for example, $K^+ \longrightarrow e^+ + \nu_e + \pi^0$). Therefore, it concludes that $\nu_\mu$ and $\nu_e$ are different particles (i.e., $\nu_\mu \neq \nu_e$) [10, 15]. In 1964, the experiment was repeated at CERN with higher statistics and confirmed the result [10, 16].

In 1975, Martin Lewis Perl and his collaborators detected the $\tau$ lepton using Stanford Linear Accelerator Center's (SLAC's) then new $e^+ - e^-$ colliding ring, called Stanford Positron Electron Asymmetric Rings (SPEAR), and the Lawrence Berkeley National Laboratory (LBNL) magnetic detector. The detection reaction was:

$$e^+ + e^- \longrightarrow e^\pm + \mu^\mp + \geq 2 \text{ undetected particles.} \tag{1.8}$$

In July 2000, Direct Observation of the NU Tau (DONUT) experiment at Fermilab, USA announced the first observation of $\nu_\tau$ events [17]. In the experiment, protons accelerated by the Tevatron were used to produce tau neutrinos via decay of charmed mesons ($D_S$). The detection principle was as following:

$$\nu_\tau + N \rightarrow \tau^- + X \tag{1.9}$$

and then

$$\tau^- \to \mu^-(e^-) + \nu_\tau(\nu_e) + \nu_\tau \quad \text{or} \quad \tau^- \to h^- + \nu_\tau. \tag{1.10}$$

## 1.3.2  Neutrino sources

Neutrinos are produced both naturally and in the laboratory. To understand the intrinsic properties of neutrinos, each of these sources provides information, sometimes overlapping.

**Solar neutrinos**

We begin with solar neutrino problem because of its historical importance. The Sun generates heat and light through thermonuclear fusion reactions. There are cycles of such reactions which take place in the Sun, for example the *pp* chain, the CNO cycle, etc., where neutrinos are produced at different stages. The effective process is the *pp* chain reaction and is summarized as following:

$$p + p + p + p \to {}^4\text{He} + 2e^+ + 2\nu_e + 26.73 \text{ MeV}. \tag{1.11}$$

The energy released in the process accounts for the luminosity of the Sun. From this, the solar neutrino flux at the Earth is calculated to be 70 billion/cm$^2$/sec. The Sun produces only electron neutrinos and they carry only MeVs of energy. The solar neutrinos were first discovered by Davis and his collaborators at Homestake gold mine, USA, as discussed in section 1.3.1.

**Atmospheric neutrinos**

The primary cosmic-rays interact with the Earth's atmospheric nuclei and produce showers of particles. Many of these particles are unstable and produce neutrinos when they decay as following:

$$\pi^+ \longrightarrow \mu^+ + \nu_\mu \tag{1.12}$$

$$\pi^- \longrightarrow \mu^- + \overline{\nu}_\mu \tag{1.13}$$

and

$$\mu^+ \longrightarrow e^+ + \nu_e + \overline{\nu}_\mu \tag{1.14}$$

$$\mu^- \longrightarrow e^- + \overline{\nu}_e + \nu_\mu \tag{1.15}$$

The atmospheric neutrino flux is $10^3/m^2/s$ and they carry energies in GeV scale. The atmospheric neutrinos were first discovered at the Kolar Gold Field (KGF) mines in South India [18] and East Rand Proprietary Gold mines in South Africa [19].

## Neutrinos from supernovae

Neutrinos are copiously emitted during stellar collapse. The first such observation of neutrinos from a supernova took place in 1987. During the early stage of stellar collapse neutrinos are produced through neutronization as following:

$$e^- + p \rightarrow n + \nu_e, \tag{1.16}$$

where only $\nu_e$s are produced. The main neutrino emission is during the cooling phase where the thermal $\nu/\overline{\nu}$s are produced through the pair production as one of the processes as following:

$$e^+ + e^- \rightarrow \nu + \overline{\nu}. \tag{1.17}$$

Neutrinos from supernovae are visible just beyond the energy range of solar neutrinos. Hence, they can be observed in detectors dedicated to solar neutrino experiments. The approximate neutrino flux observed from SN1987a Supernova was $10^{12}/m^2/s$.

## Geoneutrinos

The radioactive isotopes $^{238}$U and $^{232}$Th present in the Earth produce $\nu_e$s as a result when they naturally decay [20]. They can provide the information on the Earth's interior. The flux of geologically produced neutrinos is about $5 \times 10^{10}/m^2/s$.

## Reactor neutrinos

The very first experimental detection of neutrinos was in fact made with the reactor neutrinos at Savannah River reactor, USA, as discussed in section 1.3.1. The fission reactors are the major source of the human-generated neutrinos and they produce huge number of anti-electron neutrinos ($\overline{\nu}_e$s). The reactor neutrinos carry MeVs of energy. A standard nuclear power reactor produces about $2\times10^{20}$ $\overline{\nu}_e$s/GWth.

## Accelerator neutrinos

The particle accelerators are used to produce neutrino beams as following. An accelerated proton beam strikes a thick nuclear target, producing secondaries, such as pions and kaons. These unstable secondaries leave the target and are boosted in the forward direction. They decay in flight and produce neutrinos. This facility is called as neutrino factory.

The spectra of neutrinos from different sources as a function of their energies are shown in figure 1.2.
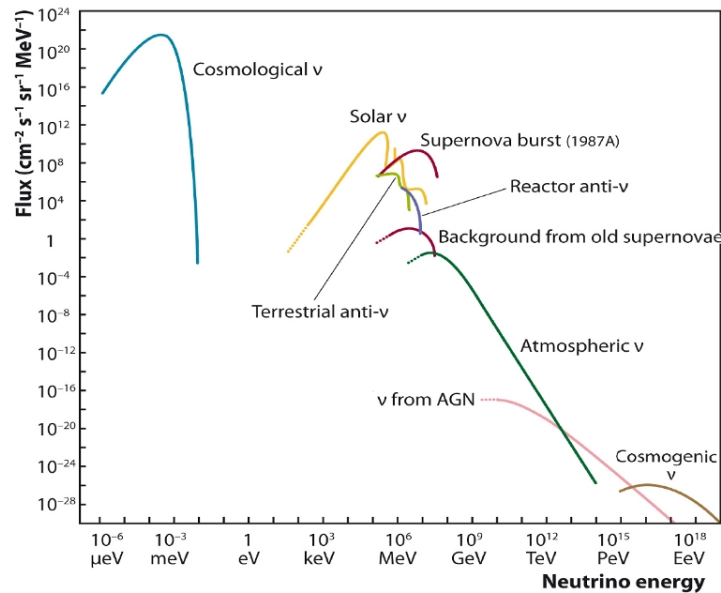


**Figure 1.2:** Neutrino spectra from different sources as a function of energy [21].

### 1.3.3   Neutrino oscillations

In the standard model, neutrinos of all flavors are assumed to be massless. This would mean that neutrinos produced with certain flavor would remain in the same flavor at all times. However, if neutrinos are not massless then there is a possibility that neutrinos can change flavor as they propagate in space. This phenomenon is called as neutrino oscillation and originates from the mixing of flavor eigenstates. Neutrinos produced via weak interaction carry definite flavor. However, when it propagates in space, its mass eigenstate remains the same as that at production but its flavor content can change. The probability of flavor change depends on the mixing angle between flavors, the masses of the eigenstates, the energy of neutrino and the distance travelled between the points of production and detection. Observation of change in neutrino flavor is of great importance in particle physics since this will be the signature of breakdown of some of the vital assumptions made in the Standard Model. The first experimental signature of the neutrino oscillation phenomenon was observed in Davis's solar neutrino experiment at the Homestake gold mine, USA. It was observerd 70% deficit in the solar neutrino flux than the theoretically predicted.

Neutrino flavor conversion is fundamentally a quantum mechanical effect. The discovery of neutrino oscillations implies that the neutrino flavor states are not mass eigenstates but superpositions of such states. Consider $\nu_\alpha$ refers to the known flavor eigenstates, $\alpha = e$, $\mu$ and $\tau$. These are related to the mass eigenstates, $\nu_i$, $i = 1,2,3$, through a $3 \times 3$ unitary matrix as following:

$$\nu_\alpha = \sum_i U_{\alpha i} \nu_i. \tag{1.18}$$

The mixing matrix is parametrized in terms of the mixing angles $\theta_{12}$, $\theta_{23}$, $\theta_{13}$ and the CP violating phase $\delta$ [22], as

$$U = \begin{pmatrix} c_{13}c_{12} & c_{13}s_{12} & s_{13}e^{-i\delta} \\ -c_{23}s_{12} - s_{23}c_{12}s_{13}e^{i\delta} & c_{23}c_{12} - s_{23}s_{12}s_{13}e^{i\delta} & c_{13}s_{23} \\ s_{23}s_{12} - c_{23}c_{12}s_{13}e^{i\delta} & -s_{23}c_{12} - c_{23}s_{12}s_{13}e^{i\delta} & c_{13}c_{23} \end{pmatrix}, \tag{1.19}$$

where, $c_{12}$ and $s_{12}$ refer to $cos\theta_{12}$ and $sin\theta_{12}$, etc. Also, it can be observed that the CP violating

phase always occurs with $s_{13}$, as highlighted in the matrix [23].

The general expression for the probability that an initial flavor state $\nu_\alpha$ ($\overline{\nu}_\alpha$) of energy $E_\nu$ gets converted to a flavor state $\nu_\beta$ ($\overline{\nu}_\beta$) after travelling a distance L in vacuum is:

$$
\begin{aligned}
P_{\nu_\alpha(\overline{\nu}_\alpha)\to\nu_\beta(\overline{\nu}_\beta)} = \delta_{\alpha\beta} &- 4\sum_{i>j}\text{Re}[U^*_{\alpha i}U_{\beta i}U_{\alpha j}U^*_{\beta j}]\sin^2\left(\frac{\Delta m^2_{ij}\,\text{L}}{4\text{E}_\nu}\right) \\
&+(-)\,2\sum_{i>j}\text{Im}[U^*_{\alpha i}U_{\beta i}U_{\alpha j}U^*_{\beta j}]\sin\left(\frac{\Delta m^2_{ij}\,\text{L}}{2\text{E}_\nu}\right),
\end{aligned}
\tag{1.20}
$$

where, $\delta_{\alpha\beta} = \sum_i U_{\alpha i}U^*_{\beta i}$ and $\Delta m^2_{ij} = m^2_i - m^2_j$ is the mass squared difference [3].

The propagation of neutrinos of energy $E_\nu$ in matter is determined by:

$$
i\frac{d\nu_\alpha}{dt} = \sum_\beta\left(\sum_j U_{\alpha j}U^*_{\beta j}\frac{m^2_j}{2\text{E}_\nu} + \frac{A}{2\text{E}_\nu}\delta_{\alpha e}\delta_{\beta e}\right)\nu_\beta,
\tag{1.21}
$$

where, $A/(2\text{E}_\nu)$ refers to the amplitude for coherent forward CC scattering in electronic matter, i.e., $\nu_e$ scattering. The matter dependent term is given by:

$$
A = 2\sqrt{2}G_F Y_e\rho\text{E}_\nu \sim 1.52\times10^{-4}Y_e\rho(\text{E}_\nu/\text{GeV})\,\text{eV}^2,
\tag{1.22}
$$

where, $\rho$ is the density of Earth matter in gm/cc and $Y_e$ is the electron fraction in the matter, while $G_F$ is the universal Fermi coupling constant [23].

### 1.3.4 Neutrino mixing parameters and mass hierarchy

As discussed in the previous section, the current accelerator, reactor, solar and atmospheric neutrino data can be described within the framework of a $3\times3$ mixing matrix between the flavor eigenstates $\nu_e$, $\nu_\mu$, and $\nu_\tau$ and mass eigenstates $\nu_1$, $\nu_2$, and $\nu_3$. The neutrino experiments have not only established the neutrino oscillations, but also have made the precision measurements of the oscillation parameters. All the three mixing angles $\theta_{12}$, $\theta_{13}$ and $\theta_{23}$ as well as the two mass squared differences $\Delta m^2_{21}$ and $\Delta m^2_{32}$ have been measured. The current best fit values and errors on these parameters for the analysis of global neutrino data are summarized in table 1.3.

**11**

**Table 1.3:** Current best fit values of the neutrino oscillation parameters for the analysis of global neutrino data [22]. NH and IH are normal and inverted hierarchies, respectively.

| Parameter | Best fit value |
|---|---|
| $\sin^2 \theta_{12}$ | $0.304 \pm 0.014$ |
| $\sin^2 \theta_{23}$ | $0.514^{+0.055}_{-0.056}$ (NH) |
| | $0.511 \pm 0.055$ (IH) |
| $\sin^2 \theta_{13}$ | $0.0219 \pm 0.0012$ |
| $\Delta m^2_{21}$ | $(7.53 \pm 0.18) \times 10^{-5}$ eV$^2$ |
| $|\Delta m^2_{32}|$ | $(2.42 \pm 0.06) \times 10^{-3}$ eV$^2$ (NH) |
| | $(2.49 \pm 0.06) \times 10^{-3}$ eV$^2$ (IH) |

The sign of $\Delta m^2_{21}$ is determined to be positive from the solar neutrino data [22]. This allows for two different arrangements of the three neutrino mass states as shown in figure 1.3. If $\Delta m^2_{32} > 0$, then the mass hierarchy (MH) is defined to be normal. If $\Delta m^2_{32} < 0$, the mass hierarchy is defined to be inverted.

The current and future neutrino oscillation experiments, NO$\nu$A [24], LBNE [25], LBNO [26], PINGU [27], ORCA [28], JUNO [29], RENO-50 [30], HK [31], T2HK [32] and INO [33] would try to address the mass hierarchy in neutrino sector and the CP violating phase $\delta$.

The current constraints on the absolute neutrino masses have been obtained from cosmological data [34, 35, 36], neutrinoless double beta decay [37, 38] and from tritium beta decay [39, 40] experiments. The neutrinoless double beta decay experiments will also seek to answer the question of whether the neutrinos are Dirac or Majorana particles.
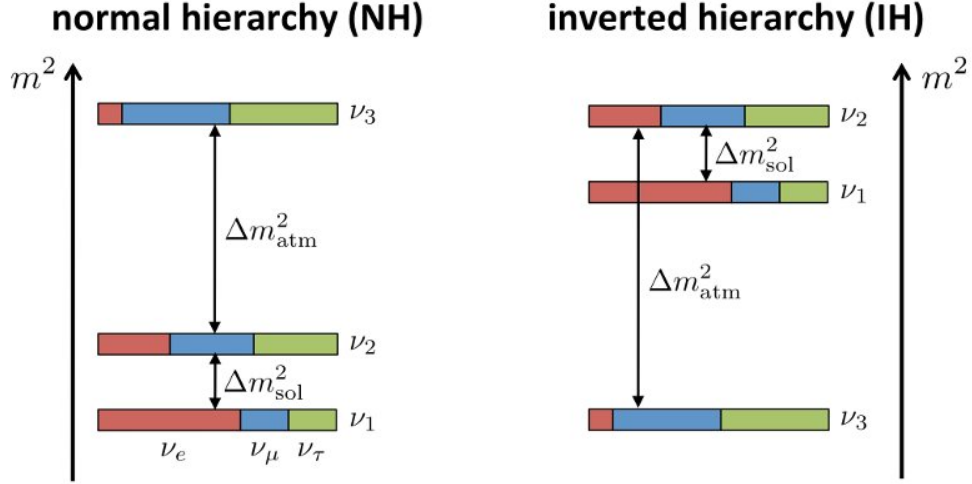
**Figure 1.3:** Pattern of neutrino masses for the normal and inverted hierarchies as mass squared [41].

## 1.4 The INO-ICAL experiment

The India-based Neutrino Observatory (INO) is an upcoming underground project in South India. The Iron Calorimeter (ICAL) experiment is going to be one of the INO experimental facilities for studying the neutrino oscillations. Additionally, it will host the experiments for neutrinoless double beta decay (NDBD), direct dark matter search, etc. The cavern for the INO will be constructed under the mountain, which will provide a rock cover of minimum 1 km in all directions to shield the experiments from the atmospheric muons. The layout of the INO cavern is shown in figure 1.4. The hall for the ICAL will have sufficient space for a 100 kiloton detector. A 3 km long access tunnel will be constructed under the mountain to reach the ICAL experiment hall [33].

The ICAL is a 50 kiloton magnetized detector to detect the atmospheric neutrinos and antineutrinos separately. The ICAL detector will comprise of three modules of $16 \times 16 \times 14.5$ m$^3$. Each module will consist of a stack of 151 horizontal layers of 5.6 cm thick iron plates interleaved with 4 cm gaps to house the active detector layers. The modular structure of the detector allows flexibility in the construction and operation. Data taking can start as soon as one of the modules is complete. The iron plates act as the target mass for the neutrino interactions. The collaboration has chosen glass Resistive Plate Chambers (RPCs) of $2 \times 2$ m$^2$ in size as the active detector elements
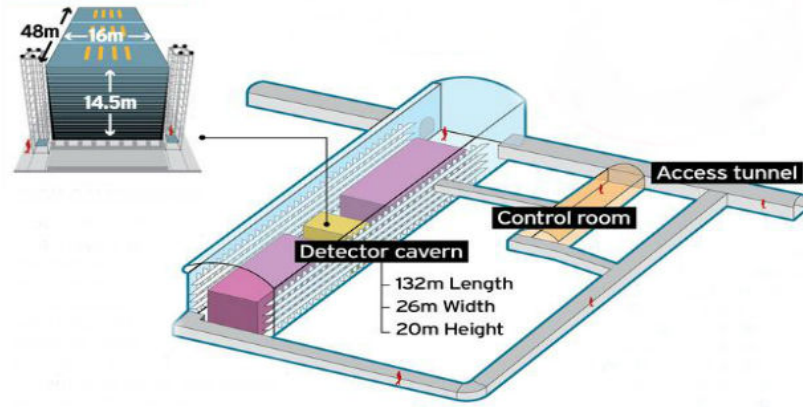
**Figure 1.4:** Layout of the proposed INO cavern.

and they will be operated in the avalanche mode. The ICAL detector is going to use 28,800 such RPCs. The iron plates are magnetized with an average magnetic field of 1.5 T. The magnetic field causes a charged particle to travel along a curved path. The layout of proposed modular form of the ICAL detector and its construction sequence are shown in figures 1.5a and 1.5b, respectively. The current specifications of the ICAL detector and RPCs are given in table 1.4 [33].
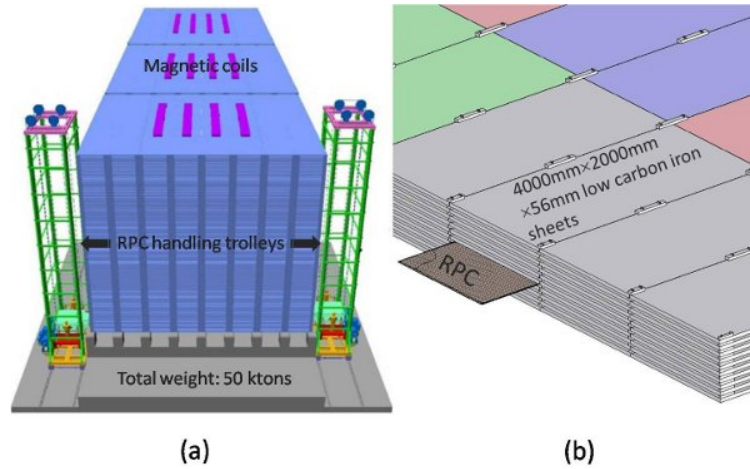


**Figure 1.5:** (a) Layout of the proposed INO-ICAL detector and (b) construction sequence of the ICAL detector.

The major components of the ICAL experiment are under research and development at the various INO collaborating institutes, universities and at industrial facilities. An engineering prototype

of the ICAL with the RPCs, iron plates and the magnet is planned at the Madurai center.

**Table 1.4:** Current specifications of the ICAL detector and RPCs.

| ICAL | | RPC | |
|------|------|------|------|
| Number of modules | 3 | RPC unit dimension | $2 \times 2$ m$^2$ |
| Module dimension | $16 \times 16 \times 14.5$ m$^3$ | Readout strip width | 2.8 cm |
| Detector dimension | $48 \times 16 \times 14.5$ m$^3$ | Number of RPC units/layer/module | 64 |
| Number of layers | 151 | Total no. of RPC units | 28,800 |
| Iron plate thickness | 5.6 cm | No. of electronic readout channels | $3.9 \times 10^6$ |
| Gap for RPC trays | 4 cm | | |
| Magnetic field | 1.5 Tesla | | |

## 1.4.1 Physics potentials of the ICAL detector

The ICAL detector is contemplated as both a detector for atmospheric neutrinos as well as a future end-detector for a neutrino factory beam. In both the cases, the primary detection mechanism is via detection of muons produced in charged current neutrino interactions such as:

$$\nu_\mu + n \rightarrow \mu^- + p. \tag{1.23}$$

The major physics goals of the ICAL detector are summarised as following:

The atmospheric neutrino physics program possible with ICAL is substantial. It is possible to observe a clear signal of oscillation by observing one full oscillation period so that the precision of the parameters $\Delta m_{32}^2$ and $\theta_{23}$ can be improved. An unambiguous evidence for matter effects can be obtained, and the sign of mass-squared difference $\Delta m_{32}^2$ can be determined. The atmospheric neutrinos can be used to probe CPT invariance which is one of the fundamental paradigms of quantum field theories.

Apart from their charge discrimination capability, iron calorimeters have a large range in sensi-

tivity to L/E variations compared to water Cerenkov detectors and can substantiate the evidence of neutrino mass and oscillation already observed by the Super-K experiment, via the observation of dips and peaks in the event rate versus L/E. Therefore, ICAL can be used as an end-detector for a neutrino factory that matches the magic baseline to determine the CP violating phase $\delta$ in neutrino sector.

The multi-TeV cosmic-ray muons can be studied through pair-meter technique. The technique is used to measure the energy and frequency of electron-positron pair cascades produced by the passage of a high energy muon in dense matter. Such studies in the high energy (TeV–PeV) region can throw light on possible extensions of the Standard Model.

## 1.5   Organization of the thesis

A brief introduction of the standard model of particle physics, gravity, neutrino physics, the INO-ICAL experiment and its physics potentials are summarized in chapter 1. The RPC and its principle of operation, designs and types of RPCs are discussed in chapter 2.

The INO collaboration has chosen glass RPCs as the active elements and is going to deploy in an unprecedented scale for the ICAL detector. Therefore, it is imperative that we study the electrode material aspects of RPCs in detail. A systematic material characterization studies on the glasses were undertaken and the detailed results are reported in chapter 3.

Several numbers of cosmic-ray paddles were developed and characterized as discussed in chapter 4. A cosmic-ray muon telescope was set up using these paddles. The RPCs of $30 \times 30$ cm$^2$ built using the glass electrodes and characterized using the cosmic-ray muon telescope. The performances of these RPCs were compared with the glass electrode material properties. The results are reported in chapter 5.

The ICAL experiment is expected to run for more than 10 years in order to record statistically significant number of neutrino interaction data. Therefore, long-term stability and performance of the RPCs over the duration of the experiment are of prime concern. The contaminants are known

cause for serious degradation in the performance or permanent damage of the RPCs. Therefore, the effect of water vapor on the performance of glass RPCs in avalanche mode operation was studied and reported in chapter 6.

For the ICAL detector, the INO collaboration has proposed two geometries: 1) default and 2) staggered. The response of these two geometries to muons ($\mu^-$s) was studied and the results are compared in chapter 7.

Finally, the conclusions and future outlooks of the thesis are drawn in chapter 8 based on various studies reported in the previous chapters.

## 1.6   Chapter summary

As a beginning, the elementary constituents of matter in the standard model and their interaction forces are summarized in this chapter. The proposal of neutrino and its discovery are discussed. The various sources of neutrinos, neutrino oscillations, neutrino mixing parameters and about the mass hierarchy issue in the neutrino sector are summarized. The INO-ICAL experiment and its physics goals are described in detail.

# Chapter 2

# Resistive plate chambers

Experimental studies in various areas of nuclear and particle physics inevitably involve detection of radiations and quite often also measurements of their characteristics. Radiations that cover a variety of energetic charged and neutral particles usually encountered in studies of atomic and sub-atomic phenomena are summerized in table 2.1.

**Table 2.1:** Types of nuclear and particle radiations.

| Types of radioactive particles | |
|---|---|
| Charged particles | Electrons, pions, protons, alpha particles and heavy ions |
| Neutral particles | Neutrons, X-rays, $\gamma$-rays and neutrinos |

Radioactive particles are detected only through their interactions with matter. The energetic charged particles interact with matter primarily by Coulomb interaction with the electrons of the medium resulting in excitation and/or ionization of the atoms and molecules of the medium. The detection of neutral particles is made possible by a two step process: the liberation of an energetic charged particle in the first step through some interaction of the neutral radiation with matter and the subsequent detection of the charged particle in the second step [42].

The radiation detectors are basically divided into three types based on their working mechanisms as following:

**Gaseous detectors**

The radiation that pass through a gas medium ionize the gas molecules. The produced charge pairs will be multiplied in an externally applied electric field and propagate in opposite directions, resulting in a measurable electrical pulse [43, 44, 45, 46]. Ionization chambers, proportional counters, Geiger-Mullar counters, resistive plate chambers etc., are widely used gaseous detectors.

**Scintillator detectors**

When radiation interacts with scintillation material, the energy is transferred to the bound states of the atoms of the material resulting transfer to short-lived excited states. The excited atoms return to their ground states and emit photons. The photons are collected by photo-detector from which the electrical pulse is generated [44, 45, 46]. Anthracene, liquid argon, polyvinyltoluene, etc., are the organic scintillators and NaI (Tl), $Bi_4Ge_3O_{12}$ (commonly known as BGO), etc., are the inorganic scntillators.

**Semiconductor detectors**

The passage of ionizing radiation through a semiconductor material creates electron-hole pairs. These electron-hole pairs are collected by an externally applied electric field. Silicon (Si) and germanium (Ge) are the commonly used semiconductors to manufacture the radiation detectors [44, 45, 46].

Based on the requirement, for example good energy resolution, spatial resolution, time resolution etc., a particular type of detector is selected for a particular nuclear or high energy physics experiment.

## 2.1   Resistive plate chamber

Resistive Plate Counters/Chambers (RPCs) are parallel plate gaseous detectors, which work on the ionization principle. They are simple to construct, offer two-dimensional readout, provide good efficiency (>95%) and excellent time ($\sim$ ps) as well as position ($\sim$ $\mu$m) resolutions. Therefore, they are used as the trigger and/or timing detectors in many high-energy physics experiments.

RPC was first developed by R. Santonico and R. Cardarelli in 1981 [47]. The RPC electrodes are made out of a high resistive material (typically, bakelite or float glass), with a bulk resistivity of $10^{10}$–$10^{12}$ $\Omega$.cm. The outer surfaces of RPC electrodes are coated with a semi-resistive paint, which facilitates applying high voltage across the electrodes [48]. The surface resistance of electrodes after the graphite coating is $\sim$1 M$\Omega$/□. The electrodes are separated a few millimeters using poly-carbonate spacers, having a bulk resistivity of $\sim10^{13}$ $\Omega$.cm, to maintain a uniform gap between the two electrodes. They are applied with high voltages $\sim$ 10 kV in order to create a uniform electric field in the gap. Conductive readout-strips are orthogonally mounted on the external surfaces of the gap. The electrodes and the readout-strips are separated using a layer of mylar insulator. The schematic of a single gap RPC is shown in figure 2.1.
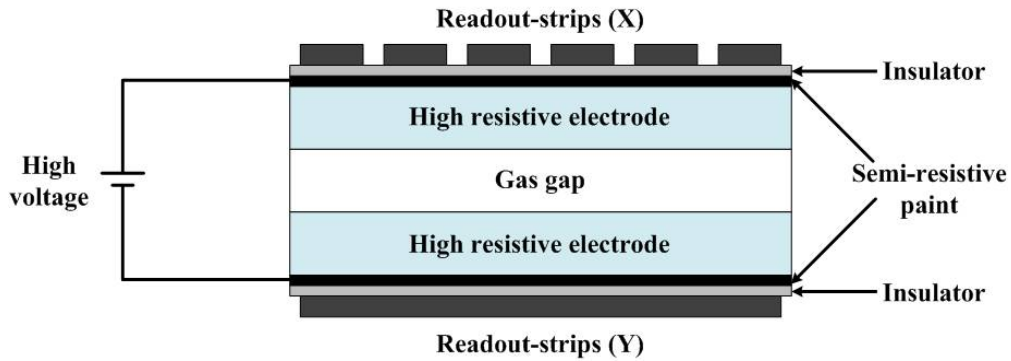


**Figure 2.1:** Schematic of a single gap Resistive Plate Counter.

The relaxation time ($\tau$) of electrode is defined as [49]:

$$\tau = RC = \frac{\rho \cdot t}{A} \frac{\varepsilon \cdot A}{t} = \rho \varepsilon = \rho \varepsilon_0 \varepsilon_r, \tag{2.1}$$

where, $R$ is resistance, $C$ is capacitance, $\rho$ is bulk resistivity, $t$ is thickness, $A$ is area, $\varepsilon$ is permittivity and $\varepsilon_r$ is relative permittivity of the electrode. $\varepsilon_0$ is permittivity of the vacuum $= 8.85 \times 10^{-12}$ F/m.

The bulk resistivity and relative permittivity of bakelite are $\sim 10^{10}$ $\Omega$.cm and 5.4 [50], respectively. Therefore, bakelite electrode relaxation time is: $\tau = 10^{10}$ $\Omega$.cm $\times 8.85 \times 10^{-12}$ F/m $\times 5.4 \approx$ 5 ms. The bulk resistivity and relative permittivity of float glass are $\sim 5 \times 10^{12}$ $\Omega$.cm and 10, respectively [51]. Therefore, glass electrode relaxation time is: $\tau = 5 \times 10^{12}$ $\Omega$.cm $\times 8.85 \times 10^{-12}$ F/m $\times 10 \approx 0.9$ s. Hence, for high counting rate experiments the bakelite RPCs are suggestable.

## 2.2 Principle of operation

An optimized gas mixture, depending on the mode of operation (discussed in the following sections), is flown through the RPC. When a charged particle passes through the gas gap, it produces the free charge carriers. These free charge carriers multiply into an avalanche under the influence of strong electric field in the gap, propagate toward the opposite electrodes and induce charge on the external readout-strips. Since the readout-strips are orthogonally placed on either side of the gas gap, we get the (x, y) coordinates of the particle using the same active detector volume. Based on the gas proportion and the experiment, RPCs can be operated in the following modes:

### 2.2.1 Avalanche mode

In the avalanche mode operation, an optimized gas mixture of Tetrafluoroethane ($CH_2FCF_3$), Iso-butane (iso-$C_4H_{10}$) and Sulfur hexafluoride ($SF_6$) in the proportion of 95/4.5/0.5 is used to operate the RPCs [52, 53]. The tetrafluoroethane or R-134a acts as both target for radiative particles to ionize and reduce the streamer size, the iso-butane limits the amount of secondary streamers by absorbing UV photons emitted from the de-excitation of molecules, and the small content of
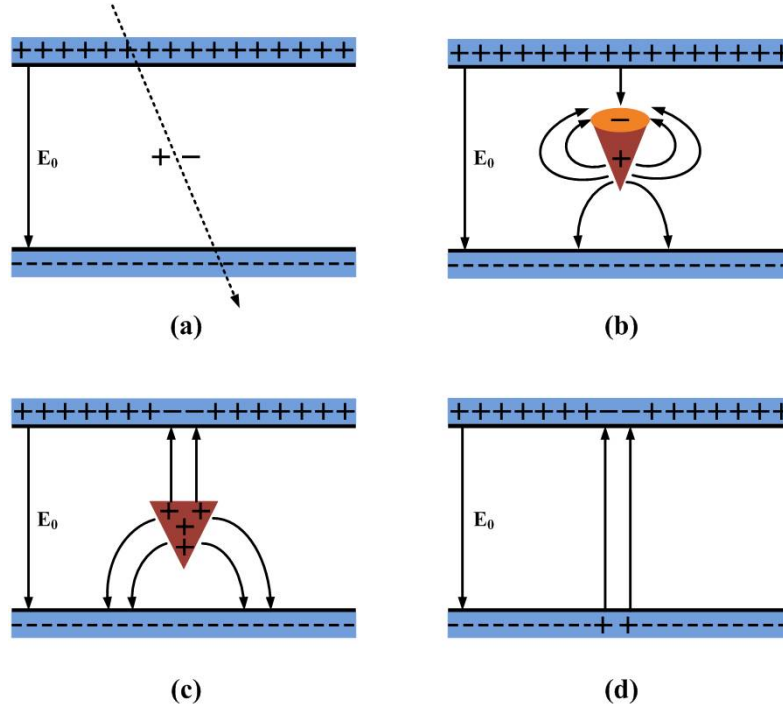
**Figure 2.2:** Schematic of an avalanche development in an RPC due to the passage of a charged particle. $E_0$ is the applied electric field. The electric field deformations caused by the avalanche charges at large gain are also shown. (a) Gas molecules are ionized due to the charged particle passage and an avalanche is started, (b) the avalanche size is sufficient enough to change the electric field in the gas gap, (c) the electrons reach the anode and the ions drift much slower, and (d) the ions reach the cathode. Because of the high resistive electrodes, the avalanche is localized to small area [54].

Sulfur hexafluoride quenches secondary electrons to reduce the streamer size. The formation of electric pulse in the RPC is essentially based on the process of electron multiplication. Say, $n_0$ is a certain number of electrons created due to the primary ionization created by the passage of ionizing particle, $\alpha$ is the first Townsend coefficient, $\beta$ is the attachment coefficient, and $x$ is the distance between the anode and the point where the cluster is produced. Then, the number of electrons that reach the anode is given by

$$n = n_0 e^{(\alpha - \beta)x}. \tag{2.2}$$

Therefore, the gain factor ($G_f$) is defined as

$$G_f = \frac{n}{n_0}.$$ 
(2.3)

In the case of avalanche mode operation of RPCs, both $CH_2FCF_3$ and $SF_6$ quench the streamer size, which leads to $G_f$ to be the order of $10^6$. The formation of additional secondary avalanches are prevented and the simple charge multiplication phenomenon occurs. This leads to the average pulse charges are about a few pC and hence pre-amplification of the pulses is required for the analysis. Therefore, the avalanche mode allows the detector to operate at a comparatively larger particle rate up to a few kHz/cm$^2$ [54]. A schematic of an avalanche development in an RPC due to the passage of a charged particle and the electric field deformations caused by the avalanche charges at large gain is shown in figure 2.2.

## 2.2.2   Streamer mode

In the streamer mode operation, an optimized gas mixture of Argon (Ar), Iso-butane (iso-$C_4H_{10}$) and Tetrafluoroethane ($CH_2FCF_3$) in the proportion of 30/8/62 is used to operate the RPCs [55]. The argon acts as target for radiative particles to ionize, iso-butane quenches UV photons emitted from the de-excitation of molecules, and the tetrafluoroethane has high electron affinity and is used to reduce the streamer size by absrobing the outer electrons [56]. In the streamer mode operation, $G_f$ (from equation 2.3) is greater than $10^8$, hence the primary ionizations are suffice to produce streamers with high probability [52].

The streamer pulses are very large that vary between 50 pC and a few nC, therefore no pre-amplification is required and the pulses can be discriminated directly against the detection threshold. Thus, the readout of streamer mode RPCs is quite simple. Because of the huge charge production, the rate capability of streamer mode RPCs is limited to a few hundred Hz/cm$^2$ [54]. A schematic of a streamer development in an RPC due to the passage of a charged particle is shown in figure 2.3.
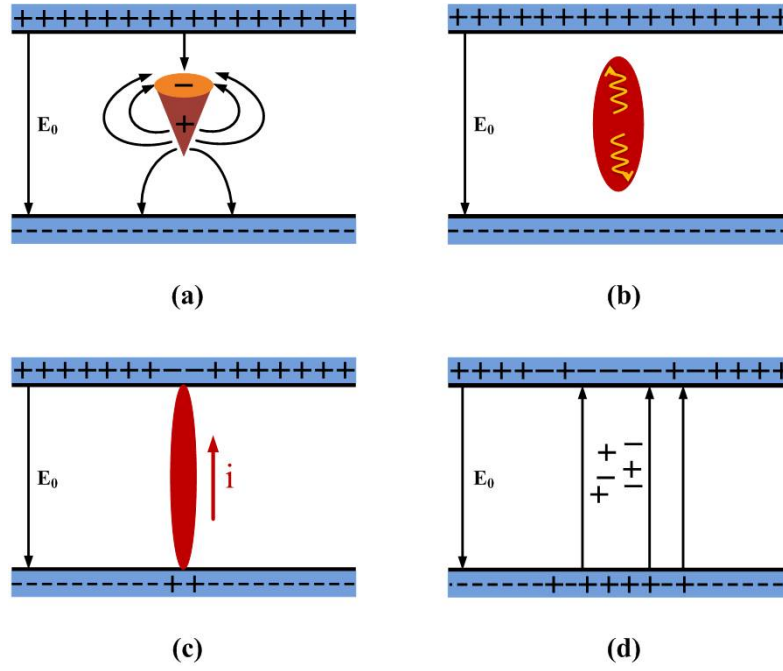
**Figure 2.3:** Schematic of a streamer development in an RPC due to the passage of a charged particle. (a) Development of an avalanche, (b) the avalanche charges lead to a high field deterioration in the gas gap, and the photons start to contribute to the avalanche development and cause a rapid spread of the avalanche: a streamer evolves, (c) a weak spark may be created, which leads to the local electrode area is discharged, and (d) the electric field is strongly decreased around the spot of the avalanche and the detector has a blind spot [54].

## 2.3 Designs of RPCs

The combination of resistive and metallic electrodes with signal-transparent semiconductive layers, highly isolating layers, and different kinds of pickup electrodes endows the RPCs with a rich variety of configurations, tunable to a variety of requirements.

### 2.3.1 Single gap RPC

The development of RPCs was started with a single gas gap using bakelite resistive electrodes [47]. In the case of single gap RPCs, generally the electrodes are separated by 2 mm using polycarbonate

spacers. The schematic of a single gap RPC is shown in figure 2.1. These RPCs are operated both in avalanche and streamer mode. They provide detection efficiencies of greater than 95% and time resolutions of 1 ns for the charged particles. Due to excellent mechanical stiffness and surface quality, the glass RPCs are also widely used in high energy physics experiments [55, 33].

## 2.3.2 Double gap RPC

The double-gap designs allow for more varied structures than the single-gap ones, because they comprise of large number of building elements [57]. One of such designs is shown in figure 2.4. The avalanches produced in either or both of the gas gaps induce signals in the common pick-up strips. Double-gap RPCs were introduced to improve the detection efficiency and counting rate capabilities [49, 58].
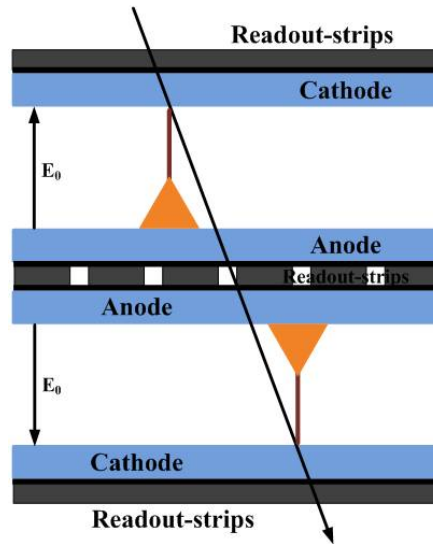


**Figure 2.4:** Schematic of a double gap RPC [57].

## 2.3.3 Multi-gap RPC

The Multi-gap Resistive Plate Chamber (MRPC) was introduced in 1996 [59]. The total gas volume in MRPC is divided into equal individual gas gaps using resistive plates of equal thickness.

A schematic of MRPC is shown in figure 2.5. Based on the experimental purposes, the individual gas gaps would vary from 0.2 mm to 1 mm [60]. The high voltages are applied only to the external surfaces of the stack of plates and the intermediate plates are electrically floating. Readout-strips are mounted on the external surfaces of the stack and are insulated from applied high voltages. The resistive plates are transparent to the fast signals generated by the avalanches (or streamers) inside each gas gap. The sum of the individual avalanche (or streamer) pulses is the induced pulse on the readout-strips. Therefore, larger size pulses are expected from MRPC. Since the intermediate resistive plates are electrically floating, the time jitter are reduced by the small size of the subgaps [61]. The MRPCs provide time resolutions up to 20 ps and efficiencies of 99% [62, 63]. Therefore, this technique is used for the Time-of-Flight (TOF) measurements [64] in high energy physics experiments as discussed in section 2.4.2.
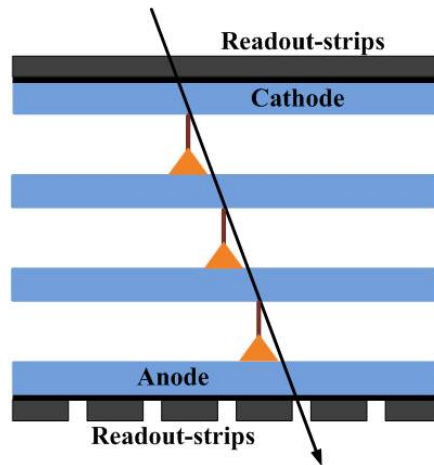


**Figure 2.5:** Schematic of a multi-gap RPC [57, 59].

## 2.4   Types of RPCs

RPCs are usually classified as trigger or timing depending on their application in an experiment. While, the distinction is largely subjective, the timing RPCs are expected to provide much better timing resolution compared to trigger RPCs and hence the former are typically used as Time-Of-

Flight (TOF) detectors in many experiments. Trigger RPCs on the other hand typically are used to detect the passage of Minimum Ionizing Particles (MIPs) such as muons and signaling the other co-detectors and their data acquisition systems to record the data.

### 2.4.1 Trigger RPCs

Single or double gap RPCs operated in avalanche or streamer mode are used as the trigger RPCs for detection and measurements on the minimum ionizing particles (MIPs) such as muons. They provide up to 98% efficiencies and ~1 ns time resolutions. This type of RPCs are used as muon trigger systems in ALICE, ATLAS and CMS experiments at CERN [58, 65], Babar and BELLE detectors [66], etc. The 2 mm gap glass RPCs, in the avalanche mode operation, are going to be used in the INO-ICAL experiment for the muon detection measurements [33].

### 2.4.2 Timing RPCs

RPCs with gas gaps of 0.2 to 0.3 mm in multigap configurations are used for the Time-of-Flight (TOF) measurements [64]. This type of RPCs are operated in avalanche mode. Their time resolutions and efficiencies are up to 20 ps and 99%, respectively [62, 67, 68]. This technique is used for the charged particle identification in high energy physics experiments like ALICE at CERN [69], STAR at RHIC [70], BESIII at BEPC II [71], etc.

## 2.5 Chapter summary

The principle of operation, designs and types of RPCs are discussed in this chapter. The RPCs are easy to construct for low cost and in large areas. They are operated either in the streamer or avalanche mode. They provide particle detection efficiencies up to 99%. The signal charges in the avalanche mode is ~1 pC and that in the streamer mode vary from 50 pC to a few nC. Therefore, the avalanche pulses are needed to be amplified before being recorded, whereas not required for

the streamer pulses. Based on the design, the RPCs can provide excellent time resolutions up to 20 ps. Therefore, they are used in many high energy physics experiments as the trigger and/or timing detectors.

# Chapter 3

# Glass electrode material study for RPCs

The INO collaboration has proposed to use glasses from Asahi and/or Saint-Gobain for producing the RPCs for the ICAL detector. The operation and performance of RPCs mostly depend on the quality and characteristics of the electrode materials. Therefore, it is imperative to study the electrode material aspects in detail. The systematic material property studies on the glasses from these two manufacturers were undertaken and the results are summarized in this chapter. The RPC detectors built using these glasses and their performances were compared with the material properties in chapter 5 [51, 72].

## 3.1   Cleaning the glasses

In an attempt to remove the surface contaminants, the glasses from Asahi and Saint-gobain manufacturers were first treated as following:

1. Thoroughly cleaned with the solution of labolene soap and deionized water

2. Rinsed in deionized water

3. Rinsed in iso-propyl alcohol and

4. Finally, dried in a filtered airstream.

During and after the treatment the glasses were handled on edges with latex free and powder free surgical gloves. After cleaning, the following measurements were performed on the samples in a clean environment.

## 3.2 X-ray diffraction studies

The studies were initiated with X-ray diffraction (XRD) tests on the glasses from both manufacturers. The glasses of $1 \times 1$ cm$^2$ size were scanned using "PANalytical X'PERT Pro X-ray diffractometer" in the $2\theta$ range of 10 to 90°. The experiments were conducted at room temperature. The measured XRD spectra for both the Asahi and Saint-Gobain glasses are shown in figure 3.1. These are broad spectra and represent the typical amorphous bands around 25° derived from the silica [73]. The identical XRD pattern was observed from both the glasses.

## 3.3 Scanning electron microscope studies

A scanning electron microscope (SEM) is a type of electron microscope, which produces images of the samples under test. For the scanning, the machine uses a focused beam of electrons. The SEM machine equipped with the energy dispersive X-ray spectroscopy (EDS) detector is used for the elemental analysis of samples. Using FEI Quanta 200 SEM machine equipped with the EDS detector, the following measurements were performed on the glasses.

### 3.3.1 Surface quality of the glasses

The surface that is in contact with molten tin, on which the glass floats during its manufacturing, is relatively smoother than the opposite surface that is exposed to air. The suggestion is that the

(a)                                                (b)
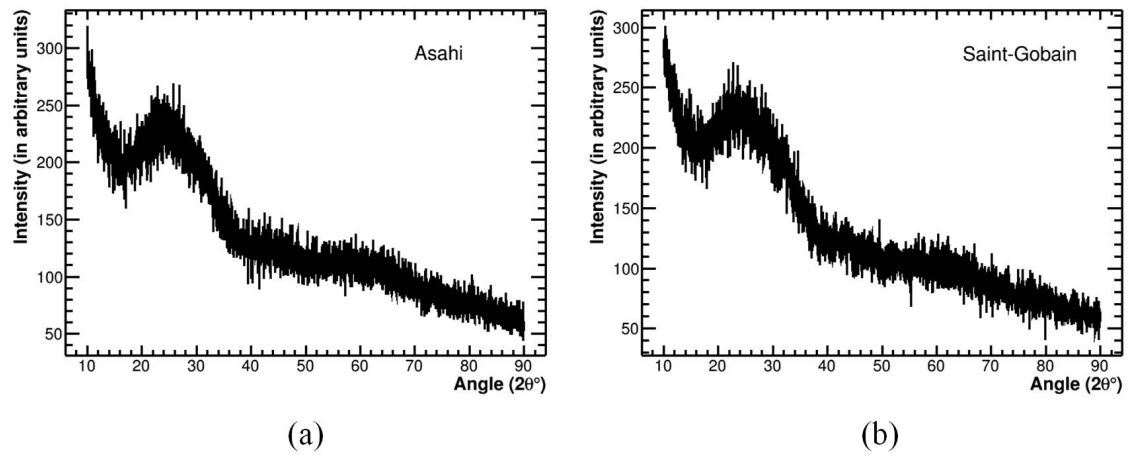
**Figure 3.1:** XRD patterns of (a) Asahi and (b) Saint-Gobain glasses.

smoother surface of the glass should face the gas volume for minimizing the field emission of electrons from cathode [74].



(a) Asahi side-1          (b) Asahi side-2

(c) Saint-Gobain side-1    (d) Saint-Gobain side-2
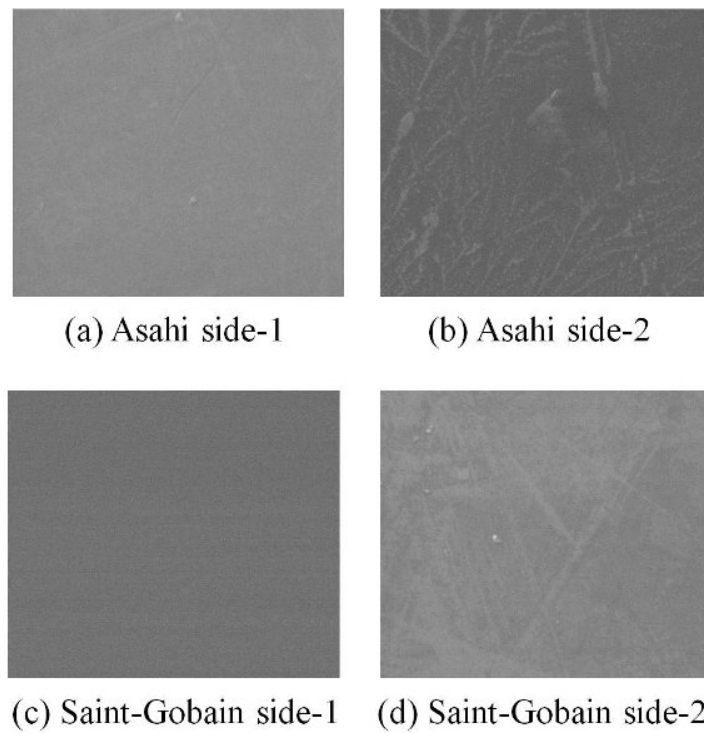
**Figure 3.2:** Images from the scanning electron microscope (SEM), which show the surface quality of both sides of the glasses. Size of each scan is 25 $\mu$m $\times$ 25 $\mu$m.

Both the sides of glasses were scanned using SEM machine and obtained their surface quality

information. The scanned images are shown in figure 3.2. The scans were taken on 25 $\mu$m $\times$ 25 $\mu$m size glasses. The side-1 of glasses are smoother than the side-2. The scratches are clearly visible on the side-2 of glasses.

## 3.3.2   Elemental composition of the glasses

The elemental compositions on the smoother surfaces of glasses (identified from figure 3.2) were measured using EDS detector. The measurements were taken on five samples from each manufacturer and the results were averaged out. The results in fractional atomic percentages are summarized in table 3.1. The calculated standard deviation ($\sigma_A$ for Asahi and $\sigma_S$ for Saint-Gobain) for each element is also given in the table. Asahi glass has showed larger Na component ($\sim 2\%$) compared to Saint-Gobain glass.

**Table 3.1:** Summary of the various elemental compositions of the glass samples in fractional atomic percentages (%). $\sigma_A$ is the calculated standard deviation for each element of Asahi glass and $\sigma_S$ is that of Saint-Gobain glass.

| Element | Asahi (%) | $\sigma_A$ (%) | Saint-Gobain (%) | $\sigma_S$ (%) |
|---|---|---|---|---|
| Oxygen (O) | 69.96 | 00.75 | 71.40 | 00.60 |
| Silicon (Si) | 15.89 | 00.44 | 16.62 | 00.45 |
| Sodium (Na) | 10.59 | 00.16 | 08.48 | 00.16 |
| Magnesium (Mg) | 02.34 | 00.12 | 02.18 | 00.10 |
| Calcium (Ca) | 00.69 | 00.12 | 00.75 | 00.09 |
| Aluminium (Al) | 00.49 | 00.09 | 00.59 | 00.13 |
| Iron (Fe) | 00.04 | 00.01 | 00.04 | 00.02 |

## 3.4 Surface roughness measurements

As mentioned in section 3.3.1, the inner surface of the electrode that is facing the gas volume should be as smooth as possible, so that the field emission of electrons from cathode can be minimized [74]. These emitted electrons increase dark current and singles rate of the RPC and thereby deteriorating its performance. Therefore, the surface roughness of the glasses from Asahi and Saint-Gobain was measured using BRUKER ContourGT Optical Microscope. The size of each scan is 582 $\mu$m $\times$ 436 $\mu$m. The microscope resolution is <0.01 nm. The measurements are shown in figure 3.3. The RMS surface roughness (Rq) values of glasses are quoted below the image of each scan. Both the glasses showed identical surface roughness on their smoother sides.



(a) Asahi side-1; Rq = 0.79 nm　　　(b) Asahi side-2; Rq = 1.28 nm

(c) Saint-Gobain side-1; Rq = 0.93 nm　　(d) Saint-Gobain side-2; Rq = 1.97 nm
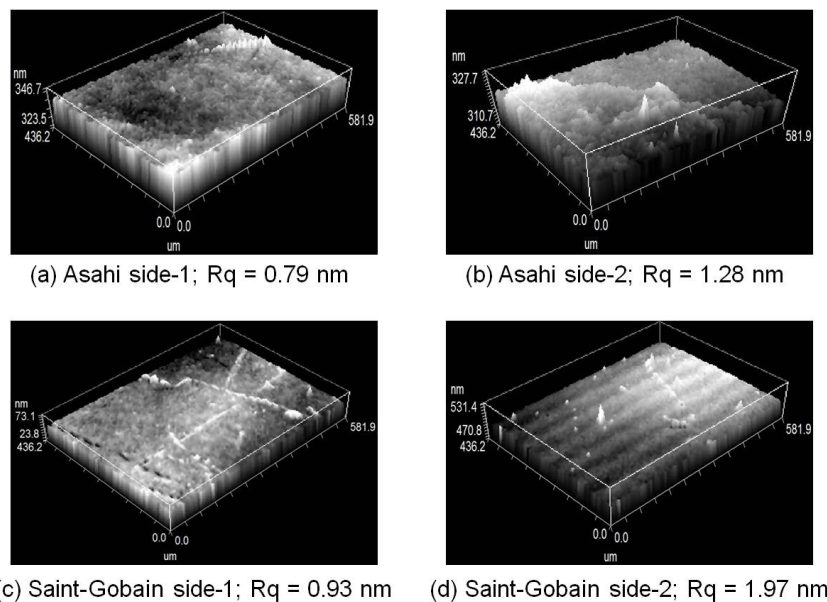
**Figure 3.3:** Surface roughness measurements of the glasses using BRUKER ContourGT Optical Microscope. Size of each scan is 582 $\mu$m $\times$ 436 $\mu$m.

## 3.5 Density measurements

The density of glass plays a role in the weight of RPC detector. The mammoth ICAL detector uses RPCs in an unprecedented scale as the active elements. Therefore, it is understood that the density

of electrodes is also an important parameter to be accounted in manufacturing the RPCs for such a big scale INO-ICAL experiment.

The density of glasses were measured using METTLER-AE163 laboratory weighing balance, which works on the Archimedes buoyancy principle. The size of each glass sample used for the measurements was $1 \times 1$ cm$^2$. The pure water was used as a reference fluid. The density of immersed object relative to the density of fluid was calculated using the formula:

$$\rho = \frac{W_1}{W_2}\rho_0.$$  (3.1)

Where, $W_1$ = Weight of object in air, $W_2$ = (Weight of object in air - Apparent weight of object in water) and $\rho_0$ = density of water at $27.4^\circ$C($\approx$ room temperature) = 0.996676 g/cc.

The measurements were taken on three samples from each manufacturer and the results were averaged out as given in table 3.2. Both the Asahi and Saint-Gobain glasses showed identical densities. Therefore, it can be expected that the RPCs made out of any of these glass electrodes would show identical weights.

**Table 3.2:** Summary of the density measurements on glasses. $\sigma_d$ is the standard deviation on average density of the glasses.

| Manufacturer | Sample Number | W1 | W2 | Density(g/cc) | Average Density (g/cc) | $\sigma_d$ ($\times 10^{-2}$ g/cc) |
|---|---|---|---|---|---|---|
| Asahi | 1 | 0.8958 | 0.357 | 2.5 | 2.4996 | 0.85 |
| | 2 | 0.9464 | 0.3757 | 2.51 | | |
| | 3 | 0.8232 | 0.3296 | 2.489 | | |
| Saint-Gobain | 1 | 0.705 | 0.2814 | 2.4968 | 2.4963 | 0.72 |
| | 2 | 1.0387 | 0.4162 | 2.4872 | | |
| | 3 | 0.8144 | 0.324 | 2.505 | | |

## 3.6   Electrical properties

The float glass is a dielectric material, therefore electrical properties of glass electrodes play a major role in the performance of RPCs. The bulk resistivity determines the leakage current of RPC [51], and the relaxation time of electrodes [49] and thereby the detector rate capability [75]. The relative permittivity determines relaxation time of electrodes [49], operating voltage, signal charge and time resolution of the RPC [51]. The INO-ICAL is a much lower counting rate experiment and therefore detector rate capability is not an issue here. The bulk resistivity and relative permittivity studies were performed on the glasses to make an informed choice on selection of the electrodes for ICAL experiment and the results are summarized as following.

### 3.6.1   Bulk resistivity

The bulk resistivity of glasses was measured using Agilent Technologies B1500A Semiconductor Device Analyzer equipped with B1511B Medium power source/monitor unit (MPSMU). The instrument provides accurate and precise measurent ranges of 10 fA - 0.1 A and 0.5 $\mu$V - 100 V. Using the equipment, the voltage-current (V-I) characteristics of the glasses were measured on 2 $\times$ 2 cm$^2$ samples of 3 mm thick. The volume resistance of glasses was obtained from the slope of that V-I plots. Then, the volume or bulk resistivity $\rho$ was obtained using the following relation:

$$R = \frac{\rho \cdot t}{A} \implies \rho = \frac{R \cdot A}{t}, \tag{3.2}$$

where, $R$, $A$ and $t$ are the volume resistance, area and thickness of the glass sample, respectively [76].

The measurements were taken on three samples of each manufacturer and the results were averaged out, which are summarized in table 3.3. Asahi glass showed larger bulk resistivity compared to Saint-Gobain glass.

**Table 3.3:** Bulk resistivities of Asahi and Saint-Gobain glasses in $\Omega$.cm. $\sigma_{BA}$ and $\sigma_{BS}$ are the calculated standard deviations on the average bulk resistivities of Asahi and Saint-Gobain glasses, respectively.

| Sample number | Bulk resistivity of Asahi glass ($\times 10^{12}$ $\Omega$.cm) | $\sigma_{BA}$ ($\times 10^{12}$ $\Omega$.cm) | Bulk resistivity of Saint-Gobain glass ($\times 10^{12}$ $\Omega$.cm) | $\sigma_{BS}$ ($\times 10^{12}$ $\Omega$.cm) |
|---|---|---|---|---|
| 1 | 4.67 | | 3.87 | |
| 2 | 4.72 | | 3.60 | |
| 3 | 4.80 | | 3.47 | |
| Average | 4.73 | 0.05 | 3.65 | 0.17 |

### 3.6.2 Relative permittivity

The permittivity ($\varepsilon$) characterizes the tendency of charge distortion or the electric polarization of a dielectric material (insulator) in the presence of an electric field. The larger permittivity implies the higher tendency of electric polarization. The permittivity of a dielectric material is expressed as [77]:

$$\varepsilon = \varepsilon_r \varepsilon_0, \tag{3.3}$$

where, $\varepsilon_0$ is the permittivity of vacuum and $\varepsilon_r$ is the relative permittivity of dielectric.

The relative permittivities of glasses were measured using 'Novocontrol Broadband Dielectric/Impedance Spectrometer' at 20 $^\circ$C. The results are shown in figure 3.4. Asahi glass showed larger relative permittivity compared to Saint-Gobain glass. Therefore, investigations were made to understand the reason for the difference in relative permittivity between the two glasses.

Normally, the float glass is made out of the chemical composition $SiO_2$, $Na_2O$, MgO, $Al_2O_3$ and CaO. The $Si^{4+}$ ions are called as network-formers and the corresponding bonding oxygen ions as *bridging oxygens*. The formation of $SiO_2$ (Si – O – Si) network in glass is illustrated in figure 3.5a. The $Na^+$, $Mg^{2+}$, $Al^{3+}$ and $Ca^{2+}$ ions are called as network-modifiers and the corresponding bonding oxygen ions as *nonbridging oxygens*. The modification of $SiO_2$ network
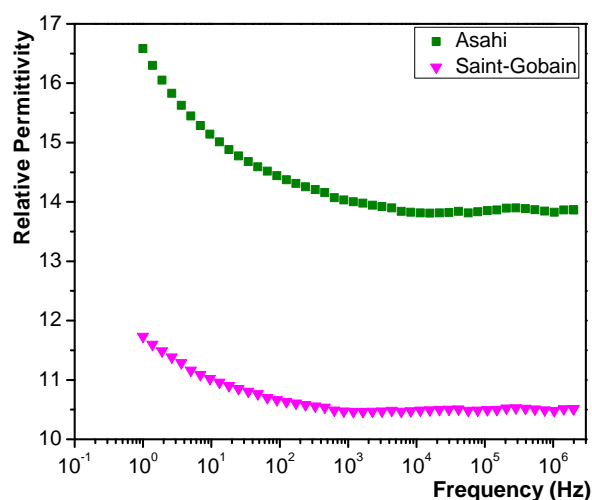
**Figure 3.4:** Relative permittivities of Asahi and Saint-Gobain glasses using Novocontrol Broadband Dielectric/Impedance Spectrometer.
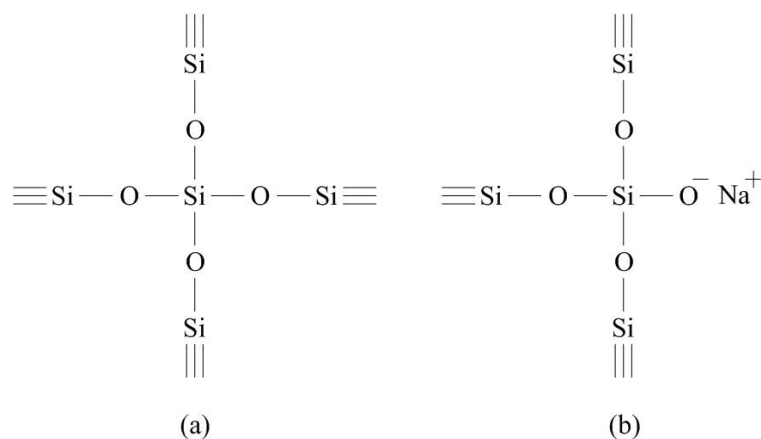


**Figure 3.5:** Schematic diagrams of (a) the Si – O – Si network formation, and (b) the Si – O – Si network modification through Na$^+$ ions in float glass.

through Na$^+$ (alkali ion) network modifiers is illustrated in figure 3.5b. In an electric field, the more content of network modifiers leads to more easily polarizable *nonbridging oxygens* and therefore the increase of relative permittivity of the material. In the case of float glass, the presence of sodium ion in the Si – O – Na structure (figure 3.5b) increases the electronic polarizability of oxygen ions and ionic polarizability of sodium ions [78]. Therefore, in an applied electric field

larger number of sodium ions leads to larger number of easily polarizable Si – O – Na structures. This implies to larger electric permittivity of the glass [79]. Asahi glass showed larger amount of sodium component ($\sim 2\%$) compared to Saint-Gobain glass as seen in table 3.1. This could be the reason for Asahi glass is showing larger relative permittivity compared to Saint-Gobain glass.

## 3.7 UV-VIS-NIR studies

During the avalanche process, the UV photons would be produced due to the excitation and de-excitation of gas molecules between the electrodes of RPC. The produced UV photons near the inner surface of electrodes would lead to the electron emissions [80]. The emitted electrons increase dark current and singles rate of the detector and thereby deteriorating its performance. Therefore, the glass with least sensitivity to the UV photons will make a better choice for the RPC electrodes.

To have a knowledge on the UV photon sensitivity to the electrodes, the band gap energy of the glasses was measured by means of their transmittance and absorbance behavior to the UV light using JASCO V-570 UV/VIS/NIR Spectrophotometer as following. For these measurements, $1 \times 1$ cm$^2$ size glasses were used.

**Transmittance**

From the Beer-Lambert law, the light transmittance through the sample is defined as:

$$T = I/I_0 = e^{-ax}, \tag{3.4}$$

where, $I_0$ = initial light intensity, $I$ = light intensity after passing through the sample, $a$ = attenuation coefficient, and $x$ = sample thickness.

The measured results on light transmittance through the glasses are shown in figure 3.6. It was observed that about 90% of the incident light was transmitted through the glasses in the VIS-NIR

(16000 – 4000 $A^\circ$) region. However, in the UV region ($\sim$4000 – 2800 $A^\circ$) the light gets severely attenuated.
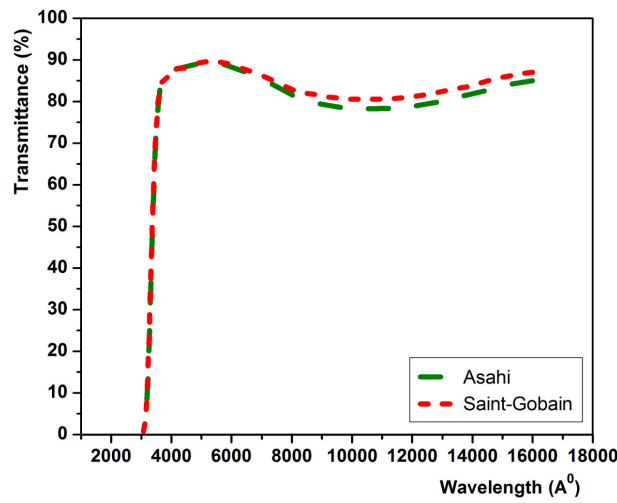


**Figure 3.6:** Transmittance of the glasses as a function of wavelength of the incident light in the UV-VIS-NIR region.

**Absorbance**

The light absorbance of glasses as a function of wavelength was calculated using the following equation 3.5. The measurement results are shown in figure 3.7(a).

$$A = -\frac{1}{2.303} ln(T),$$
(3.5)

$$\Rightarrow T = e^{-2.303A}.$$
(3.6)

From equations 3.4 and 3.6

$$ax = 2.303A,$$

$$\Rightarrow a = \frac{2.303A}{x}.$$
(3.7)

Neglecting the scattering, the attenuation coefficient $a$ can be represented as the absorption coefficient $\alpha$ [81].

From the band gap theory, the light absorption coefficient ($\alpha$) [82] is:

$$\alpha = P\sqrt{h\nu - E_g},\tag{3.8}$$

where, $h$ = Planck's constant, $\nu$ = light frequency, $E_g$ = band gap energy and $P$ = constant.

$$\Rightarrow \alpha^2 = Q(h\nu - E_g),\tag{3.9}$$

where, $Q$ is a constant.
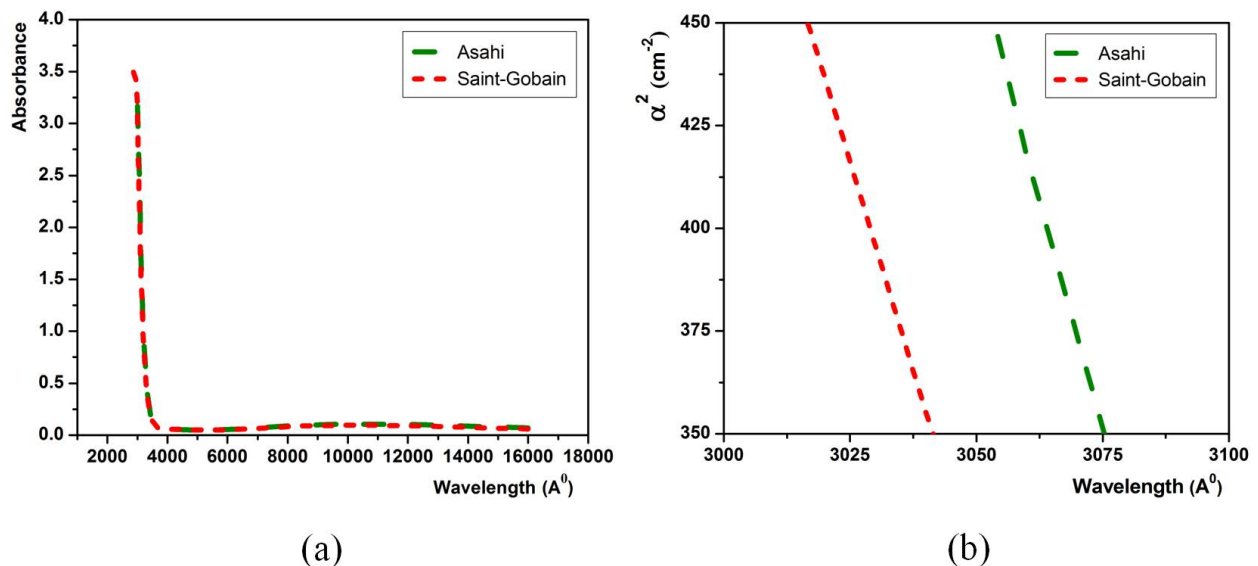


**Figure 3.7:** Absorption studies on the glass samples: (a) absorbance vs. wavelength for UV-VIS-NIR region, and (b) $\alpha^2$ vs. wavelength for UV region of the incident light.

The $\alpha^2$ values were calculated for different wavelengths of the incident light in the UV region and the plotted results are shown in figure 3.7(b). The observed wavelengths from the intercepts on X-axis of figure 3.7(b) were noted for both the glasses. Using these wavelengths, the band gap energy to emit an electron from the surface of electrode was calculated using the equation:

$$E_g = \frac{hc}{\lambda} = \frac{1240 \; eV.nm}{\lambda}, \tag{3.10}$$

where, $c$ = speed of light and $\lambda$ = wavelength of light.

The measured band gap energy results for Asahi and Saint-Gobain glasses are given in table 3.4. Both the glasses showed identical band gap energies.

**Table 3.4:** Band gap energies of the glasses.

| Manufacturer | $E_g$(eV) |
|:---:|:---:|
| Asahi | 4.03 |
| Saint-Gobain | 4.08 |

## 3.8   Chapter summary

Various material property studies were performed on the glasses from Asahi and Saint-Gobain manufacturers as electrode for the RPCs. Both the glasses showed identical behavior for X-ray diffraction, surface roughness, density and UV-VIS-NIR studies. Asahi glass contain ∼2% larger sodium component compared to Saint-Gobain glass. This could be the reason for Asahi glass showing a larger relative permittivity compared to Saint-Gobain glass. Asahi glass has larger bulk resistivity compared to Saint-Gobain glass.

# Chapter 4

# Development and characterization of

# cosmic-ray paddles

Cosmic-ray particles are ionized nuclei comprising of $\sim$90% protons, 9% alpha particles and the rest heavier nuclei. They are distinguished by their high energies, most of them are relativistic. Cosmic-rays hit the Earth's atmosphere at the rate of about 1000 per square meter per second [83]. As these particles arrive at Earth's atmosphere, they interact with the atoms and molecules present and produce secondary particles that continue to propagate towards the Earth's surface. These interactions can occur multiple times before a particle reaches sea level, while some particles can be stopped during its passage through the atmosphere. This collective flux of primary, secondary, tertiary, etc., particles are typically referred to as air showers or cosmic-ray showers as shown in figure 4.1.

In the Earth's atmosphere, high-energy primary cosmic-rays interact with atmospheric nuclei that produce pions and kaons. These particles decay into muons through the following mechanisms:

$$\pi^+ \longrightarrow \mu^+ + \nu_\mu \tag{4.1}$$

$$\pi^- \longrightarrow \mu^- + \overline{\nu}_\mu \tag{4.2}$$

and

$$K^+ \longrightarrow \mu^+ + \nu_\mu \tag{4.3}$$

$$K^- \longrightarrow \mu^- + \overline{\nu}_\mu \tag{4.4}$$

The muon is a second-generation elementary particle in the lepton sector. It is a fermion with half spin. It's mass is 105.7 MeV, making it 200 times heavier than the electron. The muon is unstable, and has a mean life-time of 2.2 $\mu$s. The most common decay modes of a muon are:

$$\mu^+ \longrightarrow e^+ + \nu_e + \overline{\nu}_\mu \tag{4.5}$$

and

$$\mu^- \longrightarrow e^- + \overline{\nu}_e + \nu_\mu \tag{4.6}$$
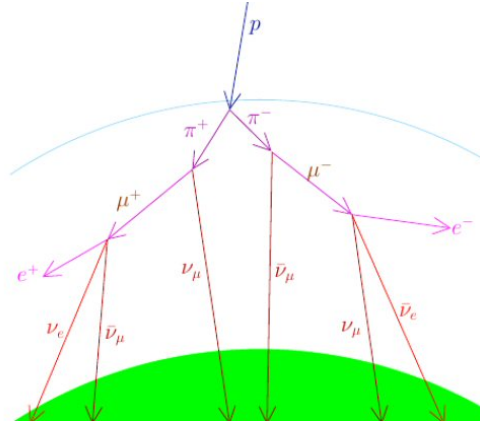


**Figure 4.1:** Typical cosmic-ray shower in the Earth's atmosphere [3].

Despite being unstable, due to its heavy mass, muons have the high penetrating power. Although muons have a short life-time, once that produced at the top of atmosphere can travel through the atmosphere and reach sea level due to their relativistic speeds. At sea level, atmospheric muons are the most abundant charged particles [84].

## 4.1 Muon interactions with matter

When a charged particle passes through the matter, it (1) release energy due to inelastic collisions with the atomic electrons of the material and/or (2) deflects from its incident direction due to elastic

scattering from nuclei, which are called as Coulombic interactions. For heavy charged particles, like muons, these effects are primarily due to inelastic collisions with the material. The amount of energy transferred during every collision is small, but in dense media the interaction cross section can be large and many collisions can occur per path length, so the cumulative effect can lead to significant energy loss.

A quantum-mechanical approach for this energy loss was first calculated by Bethe, Bloch and other authors [45]. The obtained formula is:

$$-\frac{dE}{dx} = 2\pi N_a r_e^2 m_e c^2 \rho \frac{Z}{A} \frac{z^2}{\beta^2} \left[ ln\left( \frac{2m_e\gamma^2 v^2 W_{max}}{I^2} \right) - 2\beta^2 - \delta - 2\frac{C}{Z} \right], \qquad (4.7)$$

with $2\pi N_a r_e^2 m_e c^2 = 0.1535$ MeV cm$^2$/g.

Where,

$N_a$     :     Avogadro's number = $6.022 \times 10^{23}$ mole$^{-1}$

$r_e$     :     classical electron radius = $2.817 \times 10^{-13}$ cm

$m_e$     :     electron mass = 0.511 MeV

$c$     :     speed of light = $3 \times 10^8$ m/s

$\rho$     :     density of absorbing material

$Z$     :     atomic number of absorbing material

$A$     :     atomic weight of absorbing material

$z$     :     charge of the incident particle in the units of $e$

$v$     :     velocity of the incident particle

$\beta$     :     v/$c$ of the incident particle

$\gamma$     :     $1/\sqrt{1-\beta^2}$

$W_{max}$:     maximum energy transfer in a single collision (head-on)

$I$     :     mean excitation potential

$\delta$     :     density correction

$C$     :     shell correction.
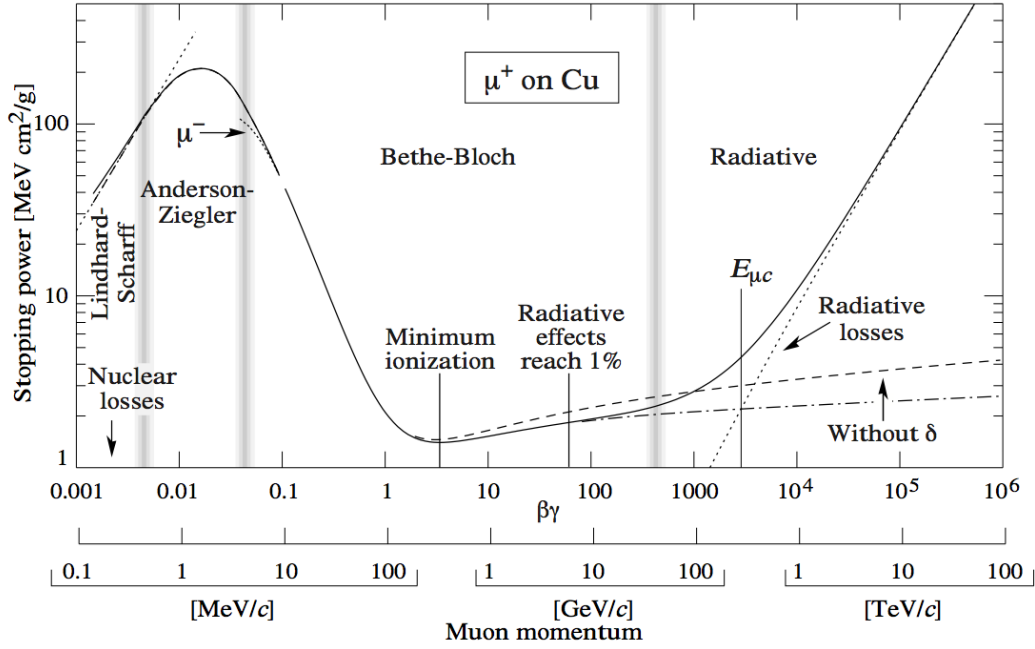
**Figure 4.2:** Energy loss of positive muons in copper as a function of momentum [22].

Equation 4.7 is commonly known as the Bethe-Bloch formula [45, 46]. The energy loss of positive muons in copper as a function of momentum is shown in figure 4.2. At low energies, the curve is decreasing until a certain point where the curve becomes relatively constant. Particles at these momenta, where the value of $-dE/dx$ is minimal, are called minimum ionizing particles. Their energy deposition per unit distance traveled over a piece of material is relatively constant. Cosmic-ray muons travel at relativistic speeds at ground level, and are typically minimum ionizing particles. For plastic scintillator, the minimum ionizing value of $-dE/dx$ is 1.9 MeV/(g.cm$^2$) [45].

## 4.2   Scintillator detector

When energetic particles or radiations pass through matter, they excite or ionize the atoms and molecules in the target material which cause the light emission called scintillation (figure 4.3). These scintillations can be coupled to an amplifying device such as a photomultiplier and converted to electrical pulses. The pulses can then be analyzed to give information concerning the incident

radiation [45].
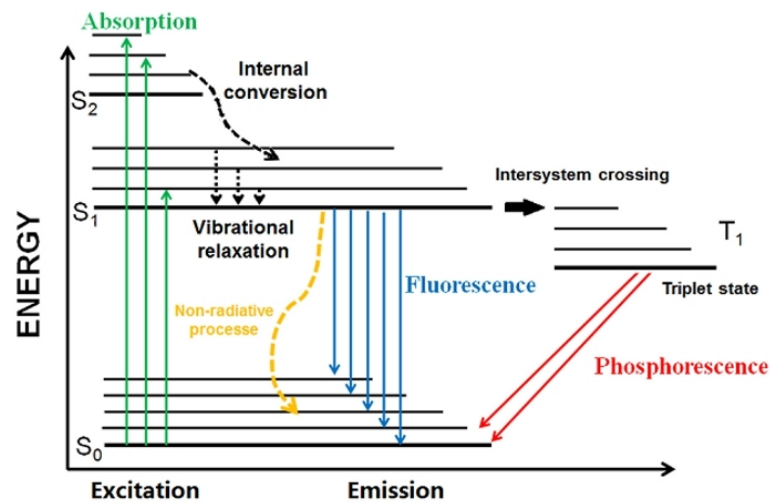


**Figure 4.3:** Schematic of the absorption and emission of light energy in a scintillation material [85].

The two main advantages of using scintillator detectors for detecting cosmic-ray muons are:

1. They are sensitive to energy. In cosmic ray showers, there are particles that come in different energy ranges. Muons with their characteristically high energies at ground level can be easily distinguished from other particles by most energy-sensitive detectors.

2. They provide fast response. This gives a better resolution to particles incident on the material since the overlapping time between light produced by different particles is minimized. More particles can then be differentiated, which leads to a higher probability in obtaining a pure signal produced solely by muons.

In general, scintillator detectors are categorized as inorganic and organic scintillators. In nuclear and particle physics, plastic scintillators are the most widely used as the organic detectors. In these detectors, only fluorescent light is produced during the excitation of molecules, and phosphorescence does not occur, which leads to fast response. Common response timings range from a couple to tens of ns.

## 4.3 Photomultiplier tube

The photomultiplier tube (PMT) converts light into a measurable electric current. The scintillator is optically coupled to a PMT either directly or via light guide. This coupled system is called scintillator detector. The schematic of PMT is shown in figure 4.4. It consists of a cathode made of photosensitive material followed by a focusing electrode, an electron multiplier section (cascaded dynode system) and finally an anode from which the final pulse can be collected. The total system is usually housed in an evacuated glass tube. The amplified electric pulse from the PMT can be analyzed to get the information of the incident radiation [45, 46].
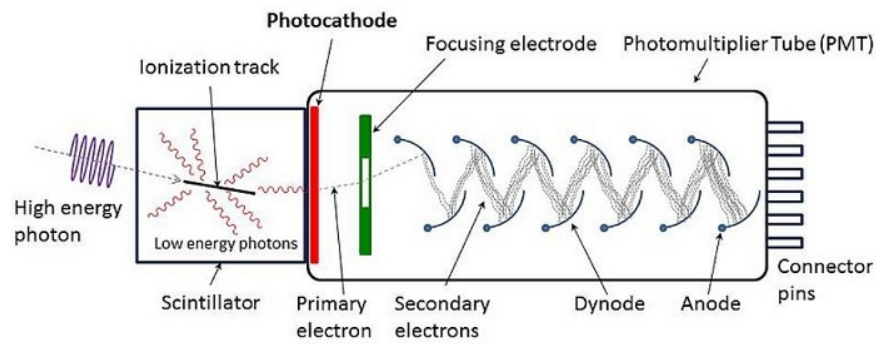


**Figure 4.4:** Schematic of the photomultiplier tube and it's working principle [86].

## 4.4 Construction of cosmic-ray paddles

The Bicron made plastic scintillators of the model no. BC-404 were used to construct the scintillator detectors (cosmic-ray paddles). The base material of the scintillators is polyvinyltoluene and its refractive index is 1.58.

### 4.4.1 Machining and gluing of scintillators and light guides

Scintillator sheets of 1 cm thick, acrylic (perspex) light guides and cookies were shaped into optimized dimensions using a Computer Numeric Control (CNC) machine. The dimensions of scintil-

lators in length $\times$ width are $30 \times 2$ cm$^2$, $30 \times 3$ cm$^2$ and $30 \times 5$ cm$^2$. The light guide channelizes produced light from scintillator to PMT. Cookies of 50 mm diameter help to couple scintillator cum light guide to PMT. The refractive index of acrylic is 1.49 matching with the refractive index of the plastic scintillator.

The schematic of scintillator and light guide drawn using OrCAD is shown in figure 4.5. The scintillators, light guides and cookies were assembled using Loctite adhesive glue. The plastic scintillator glued with light guide and cookie is shown in figure 4.6.
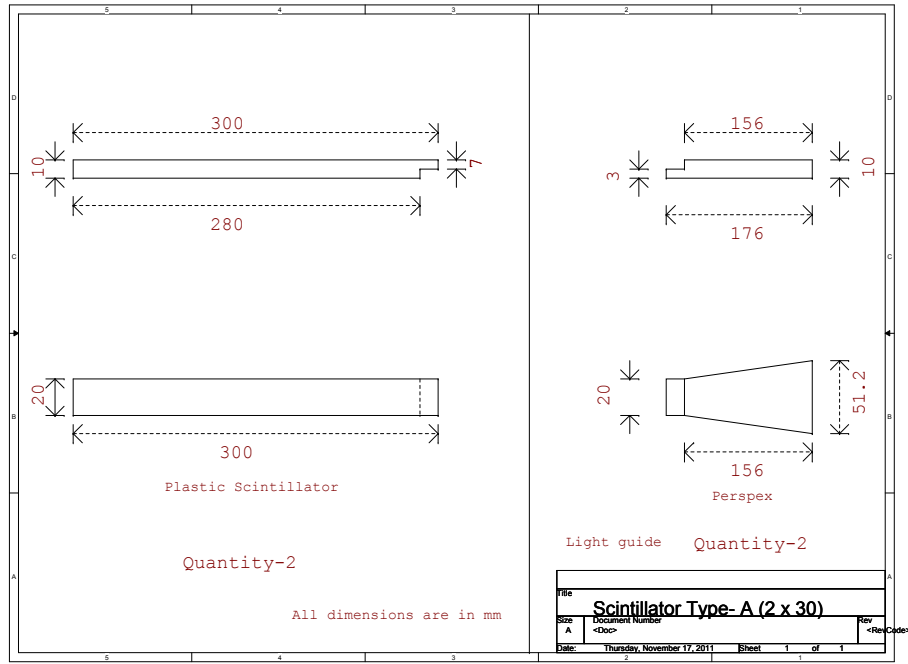


**Figure 4.5:** Schematic of $30 \times 2 \times 1$ cm$^3$ scintillator and its light guide drawn using OrCAD. All the dimensions in the figure are in mm.

### 4.4.2 Light collection and scintillator mounting

The charged particle that passes through the scintillator produces excitations and ionizations track throughout its path. This leads to the emission of photons isotropically in the scintillator. Ideally, the largest possible fraction of the produced light has to be collected and analyzed. In practical cases, however two effects arise that lead to less than perfect light collection: optical self-

**Figure 4.6:** Parts of the scintillation detectors at different stages of their construction.

absorption within the scintillator and losses at the scintillator surfaces. In the case of small size scintillators, self-absorption is usually not a significant loss mechanism. Therefore, uniformity of the light collection depends primarily on the conditions that exist at the interface between the scintillator and container in which it is mounted [46].

The scintillation emits isotropically in all directions and only a limited fraction of it can reach to the photomultiplier tube. If the remainder has to be collected, must be reflected one or more times at the scintillator surfaces. The two situations that can happen when the light photon reaches the scintillator surface are: (1) If the angle of incidence $\theta$ is greater than the critical angle $\theta_c$, total internal reflection will occur and (2) if $\theta$ is less than $\theta_c$, partial reflection and partial transmission through the surface will occur. The fraction of reflected light drops to only a few percent when the angle of incidence is near zero. Consider the refractive index of scintillation medium is $n_0$ and that of surrounding medium is $n_1$, then the critical angle is defined as [46]:

$$\theta_c = \sin^{-1}\frac{n_1}{n_0}. \tag{4.8}$$

The reflection of light photon that depends on the incident angle $\theta$ on the scintillator surface is shown in figure 4.7.
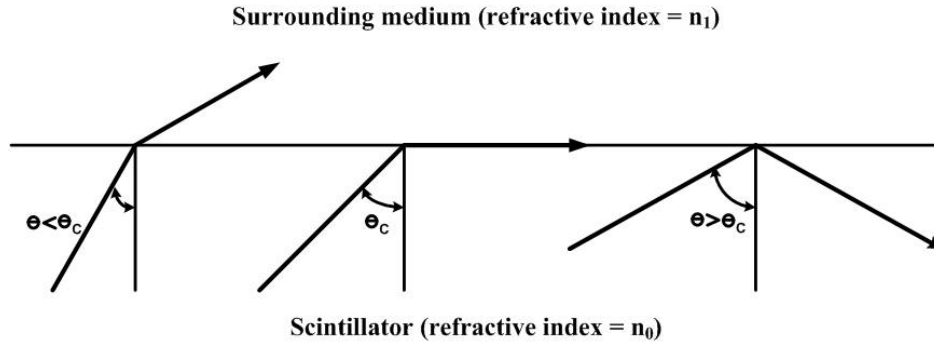
**Figure 4.7:** Transmission and reflection of the light photon from the scintillator surface at the incident angles $\theta < \theta_c$, $\theta = \theta_c$ and $\theta > \theta_c$, respectively.

To capture the light that does escape from the surfaces, scintillator is normally surrounded by a reflector at all the surfaces except that at which the phtomultiplier tube is mounted. Therefore, scintillators along with light guides and cookies were wrapped with specular-reflector aluminium tape and tyvek paper. Care was taken to avoid the inclusion of microscopic air bubbles that represent large local changes in refractive index while wrapping the reflectors. The scintillator must be shielded from ambient room light. Therefore, on top of tyvek paper the scintillators were wrapped with tedler paper followed by a layer of black tape. While wrapping the above material, special attention was paid to corners and sharp bends of the scintillator where light leaks will most likely occur. The scintillators after mounting with the required material are shown in figure 4.6.

## 4.4.3    Base circuit for the PMT

The mounted scintilltors along with light guides and cookies were optically coupled to PMTs. Twelve dynode PMTs of 51 mm diameter procured from ET Enterprises (Part number is 9807B02) were used for developing the cosmic-ray paddles. An external voltage must be applied to the PMTs in such a way that the photocathode and each succeeding multiplier stage (dynode) are correctly biased with respect to one another. The produced electrons must be attracted and hence the first dynode held at a positive voltage with respect to the photocathode. Then, each succeeding dynode must be held at a positive voltage with respect to the preceding dynode. For efficient photoelec-

tron collection, the voltage between photocathode and first dynode is several times as great as dynode-to-dynode voltage differences [46]. The required voltage differences were provided using a resistive voltage divider and a single source of positive polarity high voltage. The schematic of wiring for the base of a twelve dynode PMT is shown in figure 4.8.

The photocathode of PMT is grounded, and the divider string supplies successively increasing positive voltages to each dynode down the multiplying string. When the light photons from scintillator strike on the photocathode, phtoelectrons will be emitted by the photoelectric effect. The focusing electrode guides the photoelectrons towards the first dynode of the multiplying string, which produces the secondary electrons. These secondary electrons will be accelerated towards the second dynode and the process continues until the last dynode. The anode is at a DC potential equal to the supply voltage from which the amplified scintillator pulses could be collected.
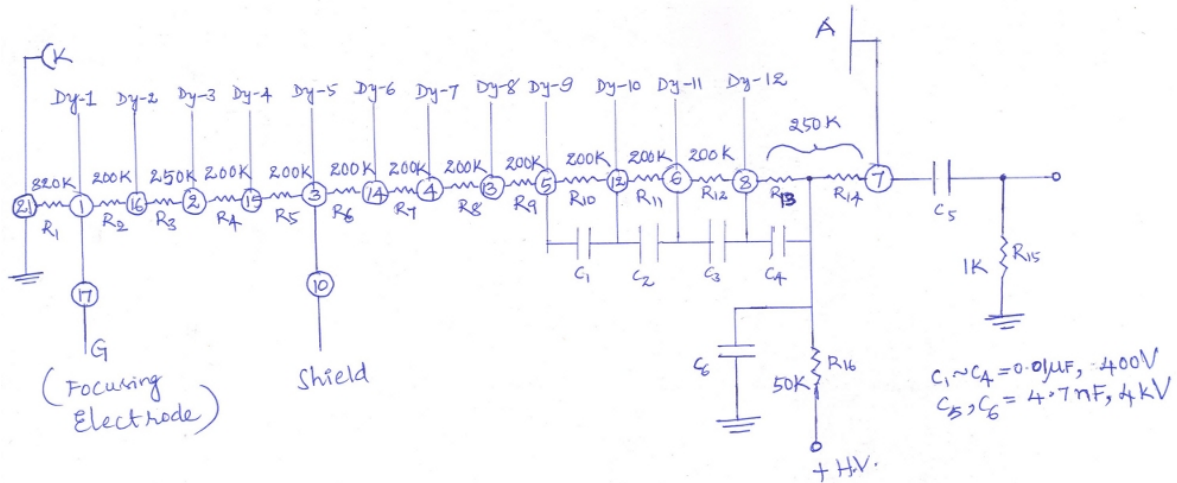


**Figure 4.8:** Schematic of wiring for the base of a twelve dynode photomultiplier tube.

The linearity in increase of voltage across the resistors of base circuits was tested with an applied voltage of 500 V. The tested results for one of the base circuits are shown in figure 4.9. The mechanical support is provided to the base circuits using suitable aluminium cylinders. One of the developed base circuits for PMT and its aluminium cylinder are shown in figure 4.6.
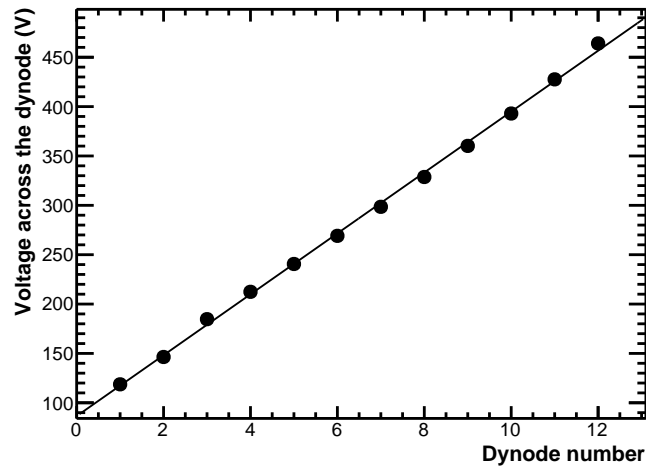
**Figure 4.9:** Linearity in the increment of voltage across the resistors of base circuit with an applied voltage of 500 V.

### 4.4.4 Assembly procedure

The base circuits were coupled to the PMT by means of the provided pins. The assembly of scintillators, light guides and cookies were then coupled to PMTs using the acrylic holders. These assemblies were wrapped with black tape for providing mechanical strength and safety handling purpose. The assembly of cosmic-ray paddle is shown in figure 4.10. One of the developed $30 \times 3 \times 1$ cm$^3$ cosmic-ray paddle is shown in figure 4.11.



**Figure 4.10:** Assembly of cosmic-ray paddle.

**Figure 4.11:** A $30 \times 3 \times 1$ cm$^3$ cosmic-ray paddle.

## 4.5   Characterization of cosmic-ray paddles

Several numbers of cosmic-ray paddles of the dimensions $30 \times 2 \times 1$ cm$^3$, $30 \times 3 \times 1$ cm$^3$ and $30 \times 5 \times 1$ cm$^3$, as mentioned in section 4.4.1, were built. Their performances were studied using cosmic-ray muons. Here, the results are summarized for one of the paddles of each dimension.

### 4.5.1   Experimental setup

A cosmic-ray muon telescope was set up with already characterized cosmic-ray paddles of the dimensions $30 \times 2 \times 1$ cm$^3$ (top), $30 \times 3 \times 1$ cm$^3$ (middle) and $30 \times 5 \times 1$ cm$^3$ (bottom). The newly developed paddles that have to be characterized (or tested) of the dimensions $30 \times 2 \times 1$ cm$^3$, $30 \times 3 \times 1$ cm$^3$ and $30 \times 5 \times 1$ cm$^3$ were named as test paddle-1, test paddle-2 and test paddle-3, respectively. The schematic of experimental arrangement of the telescope paddles, test paddle and electronic circuit developed with NIM-based DAQ system is shown in figure 4.12. The telescope window that is defined by a 2 cm wide finger paddle was centered on the test paddle.

### 4.5.2   Test results

**Singles rate as a function of applied voltage**

The singles rate of the paddles was measured using C.A.E.N Mod. N145 Quad Scaler and Preset Counter/Timer. The time elapse for each measurement was 30 min on each paddle and the results were averaged out over the time period. The singles rate of the paddles as a function of applied
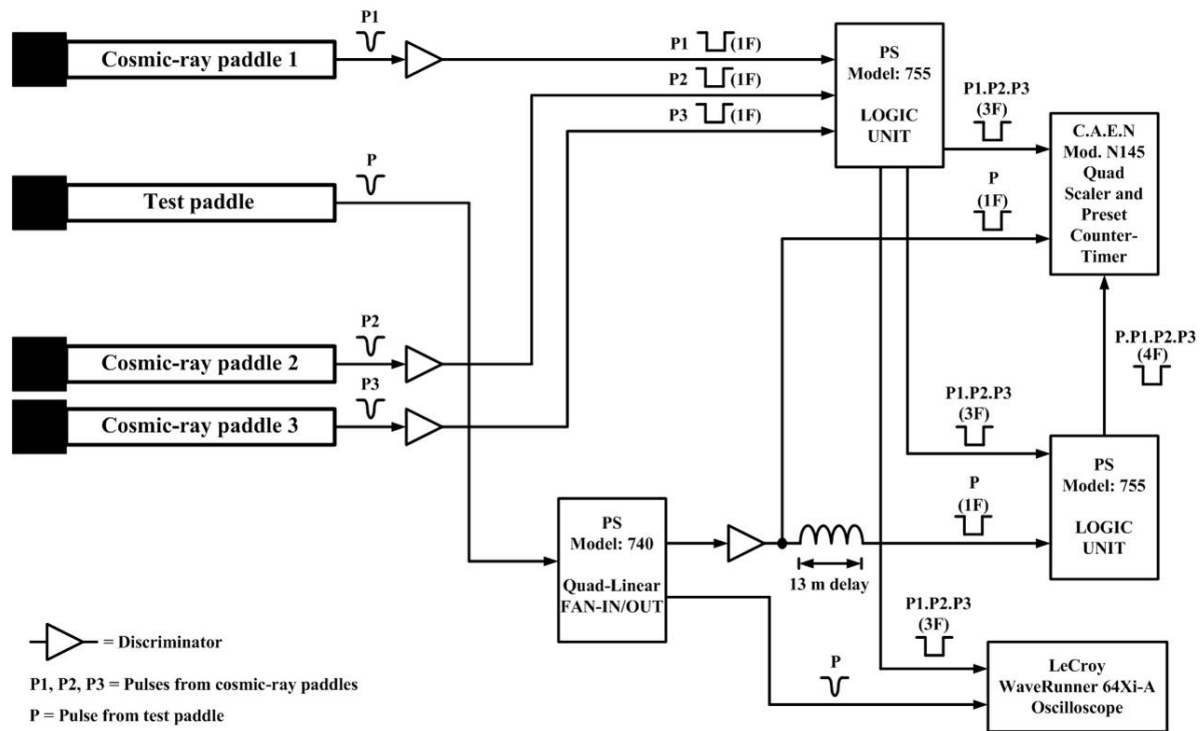
**Figure 4.12:** Schematic of the experimental arrangement for measuring the singles rate and efficiency of the cosmic-ray paddles.
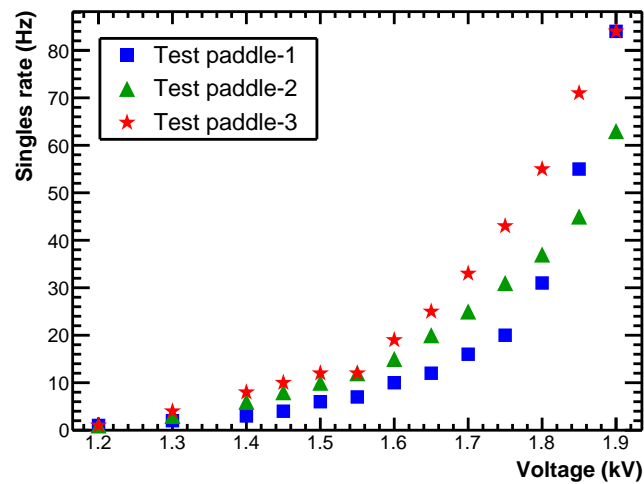


**Figure 4.13:** Singles rate of the cosmic-ray paddles as a function of applied voltage.

voltage is shown in figure 4.13. The 5 cm width paddle (test paddle-3) showed largest singles rate because of its largest acceptance cone under the telescope among the three test paddles.

**Singles rate as a function of discriminator threshold**

From figure 4.13, it was observed that a sudden increase of the singles rate of test paddles from 1.7 kV onwards. Therefore, the paddles were operated at 1.7 kV and measured their singles rate as a function of discriminator threshold. PS Model 706 sixteen channel leading edge discriminator was used for applying the various thresholds. The measurements were recorded for 30 min on each paddle and the results were averaged out over the time period. These results are shown in figure 4.14. It was observed a sudden increase of the singles rate of paddles from the applied discriminator threshold of –30 mV.
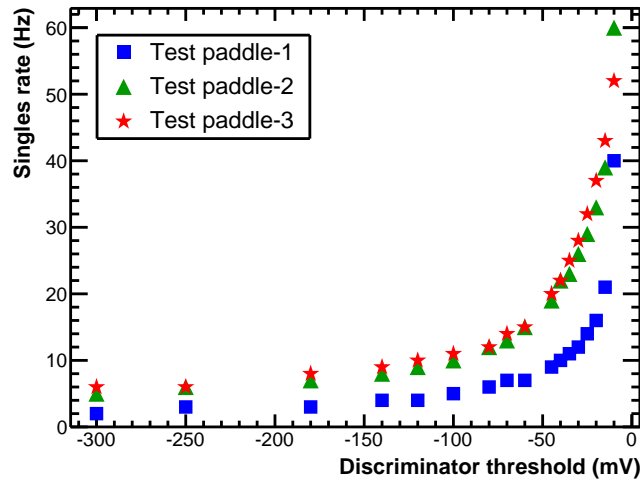


**Figure 4.14:** Singles rate of the cosmic-ray paddles as a function of discriminator threshold.

**Efficiency**

The experimental arrangement and the electronic circuit for measuring the efficiency of the newly constructed paddles is shown in figure 4.12. A –30 mV threshold was applied to the amplified pulses and the efficiency measurements were performed using C.A.E.N Mod. N145 Quad Scaler and Preset Counter/Timer. The telescope trigger pulse was recorded as 3-fold pulse (P1.P2.P3). The efficiency is defined as the ratio of the number of coincident pulses of test paddle with that telescope trigger (P.P1.P2.P3), which are 4-fold pulses, to the number of trigger pulses (3-fold

pulses). This definition is written as:

$$\text{Efficiency} = \frac{\text{4-fold (4F) rate}}{\text{3-fold (3F) rate}} \times 100\%, \tag{4.9}$$

where, 3F is the telescope trigger pulse, which is generated by the time coincidence of three scintillator counters, 4F is the coincidence pulse of the paddle under test and the telescope trigger pulse.

The measured efficiency of the paddles as a function of applied high voltage is shown in figure 4.15. The three paddles showed ∼95% efficiency on the plateau. It was observed that the knee of efficiency plateau of paddles starts at 1.4 kV. Therefore, the paddles could be operated at ≥1.4 kV.
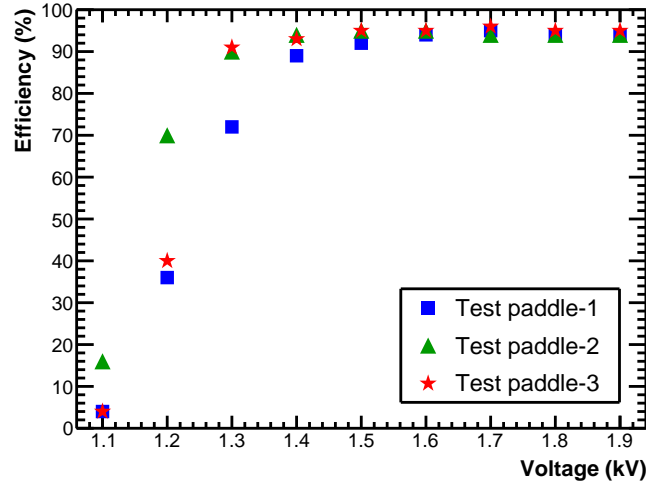


**Figure 4.15:** Efficiency of the cosmic-ray paddles as a function of applied voltage.

**Signal charge**

The experimental arrangement developed for the signal charge measurements of the paddles is shown in figure 4.16. The schematic of experimental arrangement of cosmic-ray telescope, test paddle, and NIM and CAMAC-based DAQ system is shown in figure 4.17. The measurements were performed using PS Model 7166 Common GATE Charge to Digital Converter (ADC). The resolution of this ADC is 0.25 pC. The trigger pulse (P1.P2.P3) was used as the Common GATE
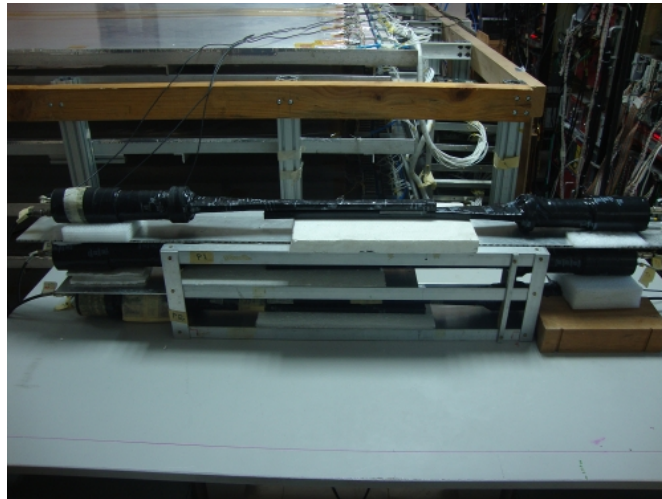
**Figure 4.16:** Experimental arrangement for characterizing the newly constructed cosmic-ray paddles.
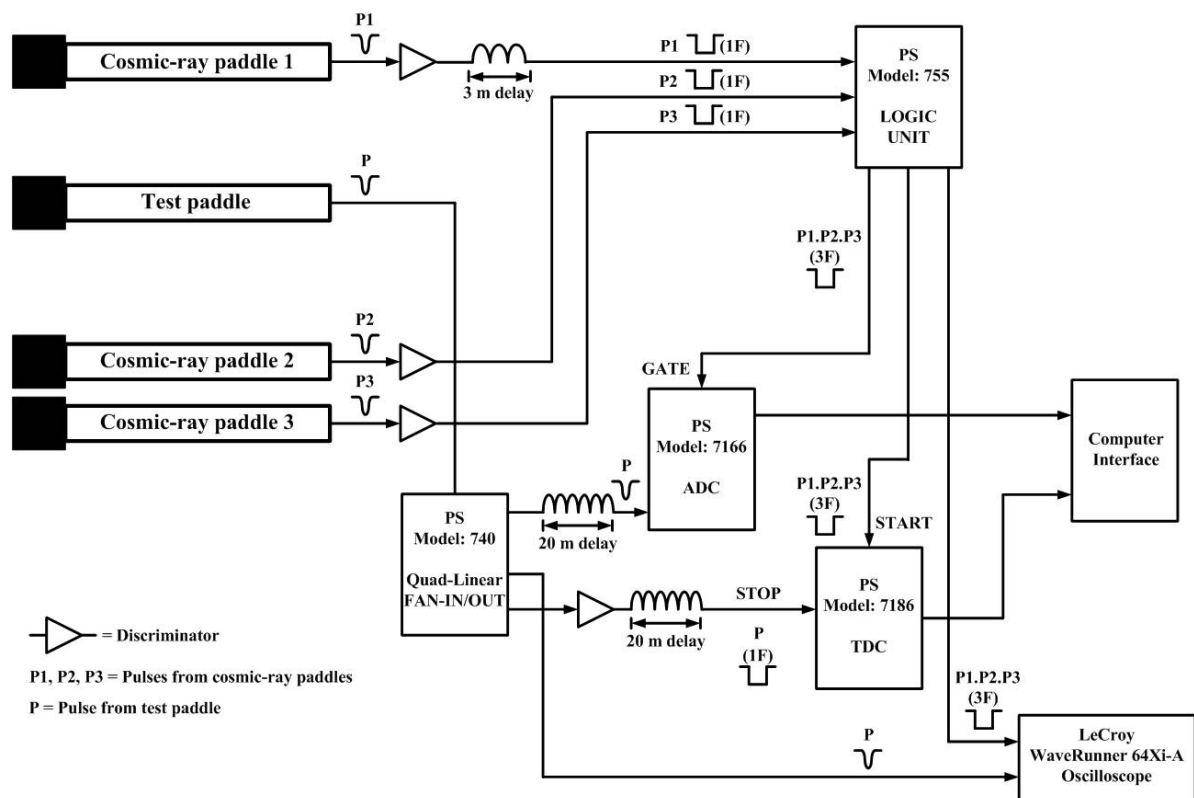


**Figure 4.17:** Schematic of the experimental arrangement for measuring the signal charge and time resolution of cosmic-ray paddles.

for ADC. The charge collection of the paddles followed the landau distribution and the results are

shown in figures 4.18, 4.19 and 4.20.

**Time resolution**

The experimental arrangement for the time resolution measurements of paddles is shown in figure 4.16. The schematic of experimental arrangement is shown in figure 4.17. The measurements were performed using PS Model 7186 Common START Time to Digital Converter (TDC). The resolution of this TDC is 0.1 ns. The trigger pulse (P1.P2.P3) was used as the Common START for TDC. The timing distribution of paddles is shown in figures 4.21, 4.22 and 4.23. The three tested paddles showed identical results.

Signal charge of test paddle-1 =
236.6 × 0.25 pC = 59.2 pC.
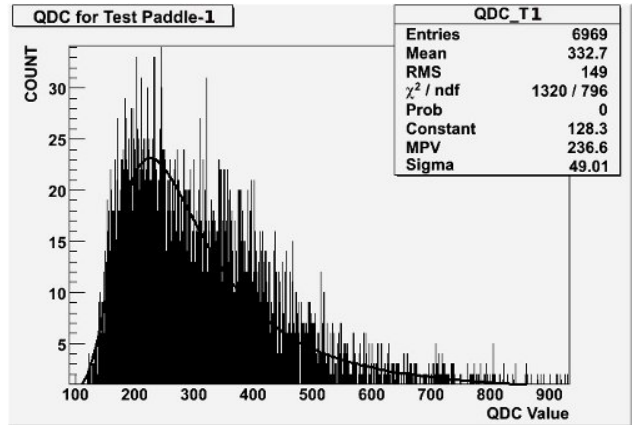


**Figure 4.18:** Charge distribution of the test paddle-1.

Signal charge of test paddle-2 =
334.9 × 0.25 pC = 83.7 pC.
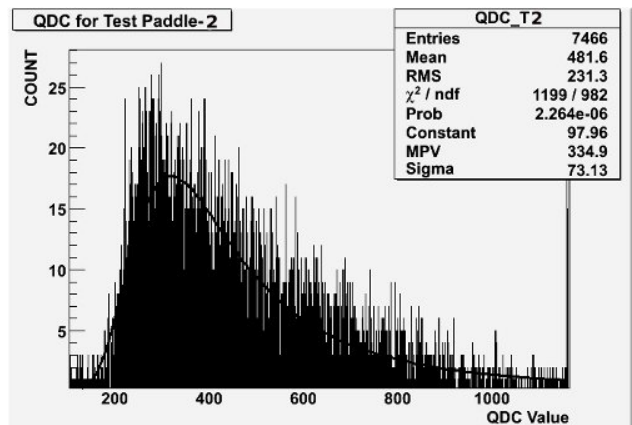


**Figure 4.19:** Charge distribution of the test paddle-2.

Signal charge of test paddle-3 = 432.7 × 0.25 pC = 108.2 pC.
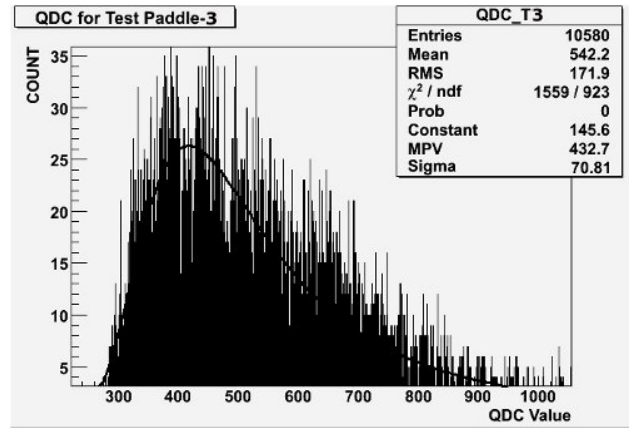
**Figure 4.20:** Charge distribution of the test paddle-3.



Time resolution of test paddle-1 = 7.375 × 0.1 ns ≈ 0.74 ns.
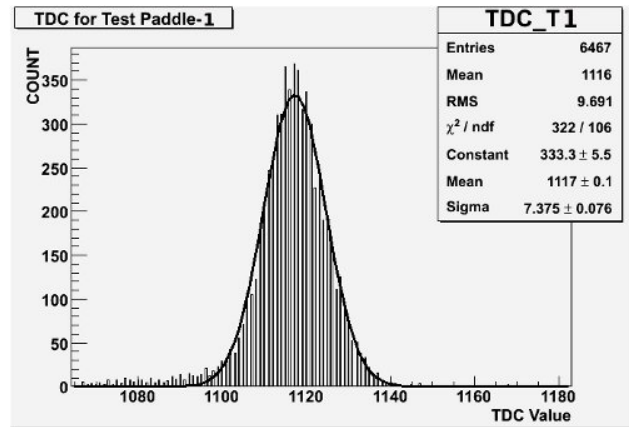
**Figure 4.21:** Timing distribution of the test paddle-1.



Time resolution of test paddle-2 = 7.213 × 0.1 ns ≈ 0.72 ns.
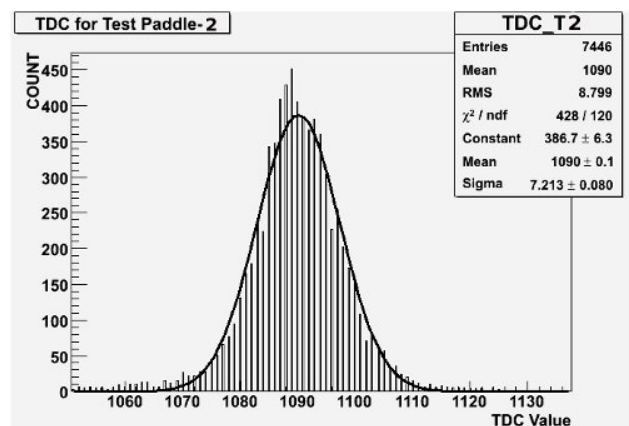
**Figure 4.22:** Timing distribution of the test paddle-2.

Time resolution of test paddle-3 =

$7.497 \times 0.1$ ns $\approx 0.75$ ns.
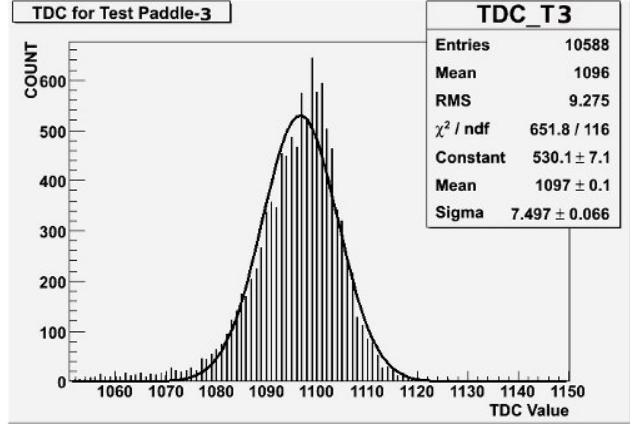


**Figure 4.23:** Timing distribution of the test paddle-3.

## 4.6 Chapter summary

Several numbers of cosmic-ray paddles of the dimensions $30 \times 2 \times 1$ cm$^3$, $30 \times 3 \times 1$ cm$^3$ and $30 \times 5 \times 1$ cm$^3$ were developed. The plastic organic scintillators of above dimensions, light guides and cookies in an optimized dimensions were cut using a CNC machine. Then, they were assembled using Loctite adhesive glue. To capture the light that escapes from the surfaces, scintillators along with light guides and cookies were wrapped with specular-reflector aluminium tape and tyvek paper. They were shielded from ambient room light using tedler paper followed by a layer of black tape. To apply voltage to the PMT dynodes, base circuits were developed using a resistive voltage divider. The linearity in increase of voltage across the resistors of base circuits was tested. These base circuits were coupled to 9807B02 type PMTs by providing aluminium cylinders support. The coupled scintillators, light guides and cookies were assembled to PMTs using acrylic holders. Then, these assemblies were wrapped with black tape for providing mechanical strength and safety handling purpose.

A cosmic-ray muon telescope was set up with already characterized cosmic-ray paddles using NIM and CAMAC-based DAQ systems. The newly developed paddles were characterized using this telescope. In this chapter, the results are summarized for one of the paddles from each dimension. They showed ~95% efficiency on the plateau. The signal charges of the paddles of width 2,

3 and 5 cm are 59.2, 83.7 and 108.2 pC and time resolutions are 0.74, 0.72 and 0.75 ns, respectively. These newly characterized paddles were used to develop the cosmic-ray muon telescope for characterizing the resistive plate chambers, as reported in chapters 5 and 6.

# Chapter 5

# Development and characterization of RPCs

As reported in chapter 3, the INO collaboration has proposed to use glasses from Asahi and/or Saint-Gobain for producing the RPC gas gaps for the ICAL detector. The float glass is a dielectric material, hence operation and performance of the glass RPCs are influenced by the electrical properties of electrodes. In this chapter, the development and characterization studies of $30 \times 30 \text{ cm}^2$ size RPCs made of Asahi and Saint-Gobain glass electrodes are reported. These RPCs performances are compared with the electrical properties of the glasses discussed in chapter 3. A qualitative agreement in the RPCs performances and the electrical properties of glasses was observed.

## 5.1 Development of RPCs

The development of RPCs involves deploying a large number of materials as well as many assembly procedures. The production of high performance and reliable chambers involves choosing the right type and quality of materials as well as optimizing of various assembly and quality control procedures involved in the construction. Here, several numbers of $30 \times 30 \text{ cm}^2$ size glass RPCs are constructed using the Asahi and Saint-Gobain glass plates. The following is the step by step

procedure used for constructing the RPCs.

## 5.1.1  Cleaning the glass plates

The float glass plates of 3 mm thick were procured from Asahi and Saint-Gobain manufacturers. They were cut into $30 \times 30$ cm$^2$ size using TUOFENG Precision Glass Cutter. The four corner edges were chamfered using a jig of right dimension to make a correct $45°$ angle. In an attempt to remove the surface contaminants, the glass plates were treated as following:

1. Thoroughly cleaned with the solution of labolene soap and deionized water

2. Cleaned with deionized water while rubbing with sponge

3. Dried in a filtered airstream and

4. Finally, cleaned with iso-propyl alcohol

 During and after this treatment the glass plates were handled on edges with latex free and powder free surgical gloves.

## 5.1.2  Semi-resistive coating on the glass surfaces

It is suggested that the smoother surface of RPC electrodes should face the gas volume. Hence the tin side, which is the smoother surface, of glass plates was identified using TS2300 Digital Tin Side Detector. The air side of the glass plates was coated with specially developed semi-resistive graphite paint for the ICAL RPCs [87]. The coated surfaces were dried in sunlight for a few minutes. The surface resistance of coated films was measured using an indigenously developed copper jig as shown in figure 5.1 and is maintained to be uniform at $\sim$1 M$\Omega$/$\square$. The measured surface resistance of the two electrodes while jig oriented in the horizontal and vertical positions is shown in figure 5.2.
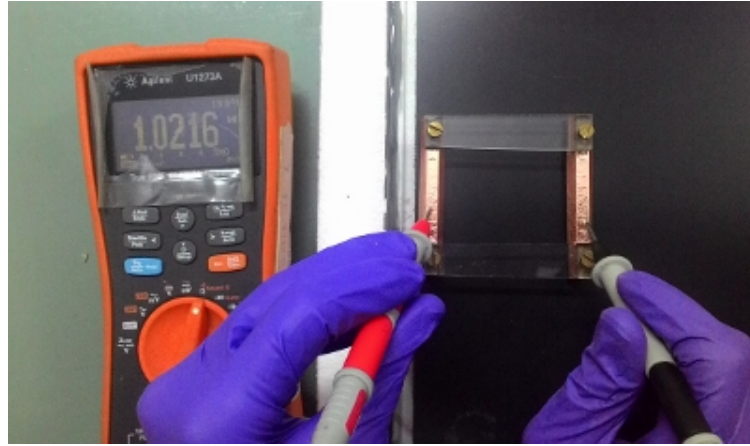
**Figure 5.1:** Surface resistance measurement of the electrode using a copper jig.
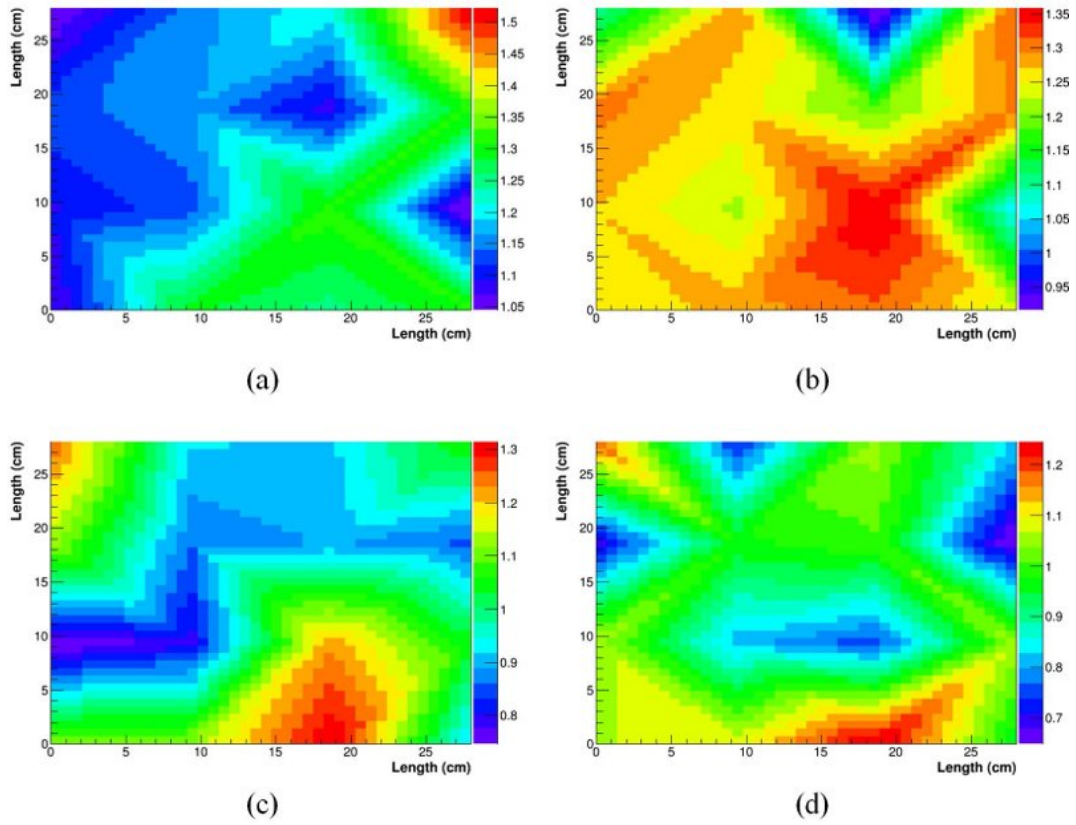


**Figure 5.2:** Surface resistance of (a) electrode 1, (c) electrode 2 while jig oriented in the horizontal position and (b) electrode 1, (d) electrode 2 while jig oriented in the vertical position. The measurements are in the units of MΩ/□.

### 5.1.3   Construction of RPC

The bottom glass electrode was mounted on a perfectly even horizontal table. A precise amount of 3M Scotch-Weld DP190 Gray Epoxy Adhesive was dispensed at four points on the electrode using a designated grid. Each point is at 10 cm away from the center of the diagonal of electrode. The polycarbonate button spacers of 0.2 cm thick and 1 cm diameter were then placed on these points. The adhesive was again applied on the top side of buttons. The square frame made of 0.2 cm thick side spacers and gas nozzles was placed on the bottom electrode. Then, the top electrode was mounted on the buttons and side spacers. The schematic designs of the button, side spacers and gas nozzle are shown in figure 5.3. The bulk resistivity of these spacers is $\sim 10^{13}$ $\Omega$.cm [52]. In order to make sure the button spacers was glued well on both sides to the electrodes, heavy steel blocks were placed on the assembly. One side of the outer spacers were glued to the electrodes using the adhesive and allowed for a day to gain handling strength. The opposite side was glued on the next day and allowed for a week to full cure. In this way, the gap is maintained to be isolated from the ambient environmental conditions. Then, this gap was assembled with gas inlets and outlets of tygon tubing having 3/16" inner diameter. The step by step procedure of constructing RPC is shown in figure 5.4.



(a)                              (b)                              (c)
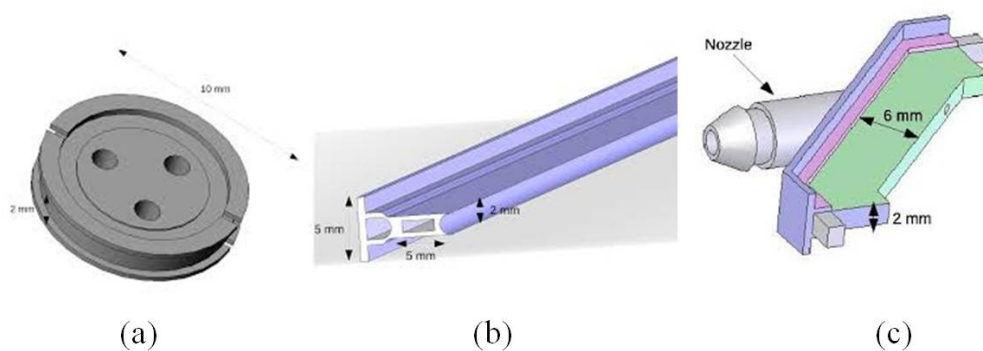
**Figure 5.3:** Schematic designs of (a) button spacer, (b) side spacer and (c) gas nozzle.
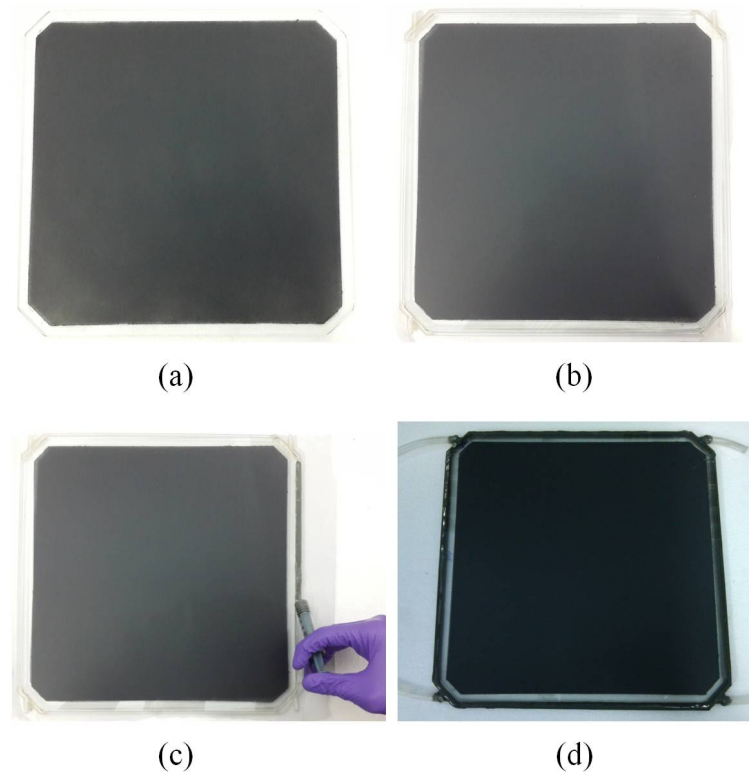
**Figure 5.4:** Step by step procedure of constructing the RPC. (a) A $30 \times 30$ cm$^2$ glass plate chamfered at the four corner edges and coated with semi-resistive paint, (b) the parallel electrodes were separated by 0.2 cm using polycarbonate spacers and gas nozzles, (c) the outer spacers were glued to the electrodes using 3M Scotch-Weld DP190 Epoxy Adhesive and (d) the RPC was assembled with gas inlets and outlets using tygon tubing of 3/16" inner diameter.

## 5.2   Gas mixing system

The INO collaboration has chosen to operate the RPCs in the avalanche mode. The gas mixing system designed and developed by local vendors for the INO collaborators was used to flush the gas through the RPC gap, which acts as an active medium for the charged particles that pass through the RPC. This unit can mix up to four individual gases and has 8 output channels. The mass flow controllers (MFCs) are used to measure and control the flow rate of gases. The gas mixing system used for operating the RPCs is shown in figure 5.5.

        (a)                                 (b)
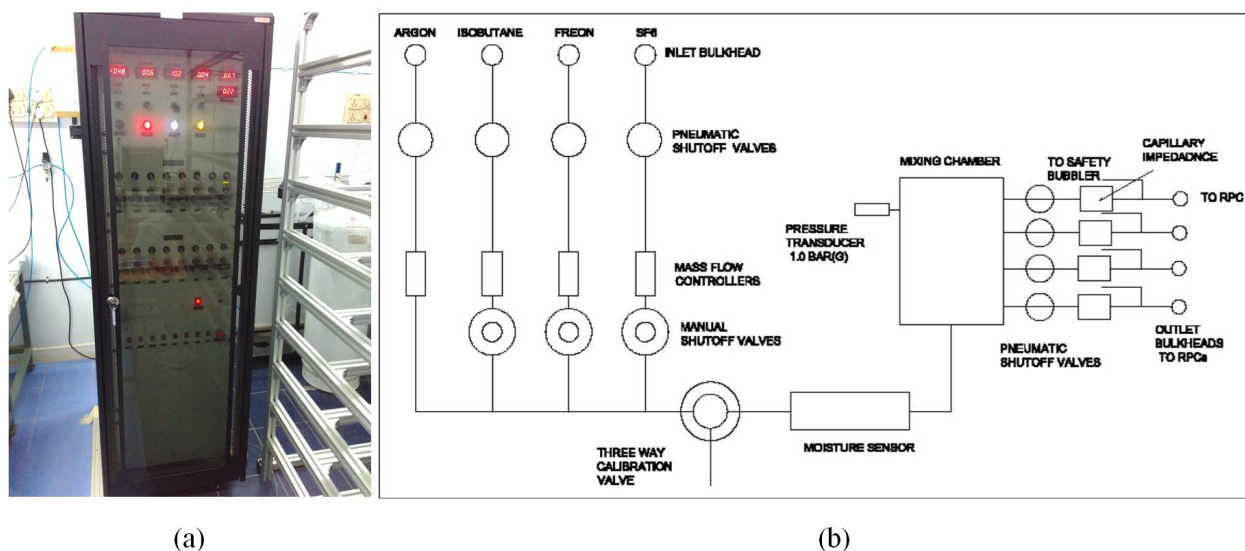
**Figure 5.5:** (a) Gas mixing unit and (b) layout of the gas mixing and distribution system for operating the RPCs.

## 5.2.1   Calibration of MFCs

An optimized gas mixture of freon ($C_2H_2F_4$), iso-butane (iso-$C_4H_{10}$) and sulfur hexafluoride ($SF_6$) was used to operate the RPCs in the avalanche mode. The MFCs for theses gases were calibrated by the water downward displacement method. In this method, a burrette filled with water was inverted into a container filled with water by means of a chemistry stand. The gas tube from the MFC output was carefully inserted into the burette as shown in figure 5.6. The time taken for fixed amount of volume drop ($\Delta V$) of water (equal to the amount of gas collected) in the burette was recorded for the different set flow rates of MFC. The volume drop divided by time taken is the actual flow rate of MFC for the corresponding set flow rate.

The vendor advised to calibrate the MFCs in the interval of six months. The MFC calibration plots for the three gases are shown in figure 5.7. In the figure, X-axis is the MFC set flow rate and Y-axis is the actual flow rate in the units of standard cubic centimeters per minute (SCCM).
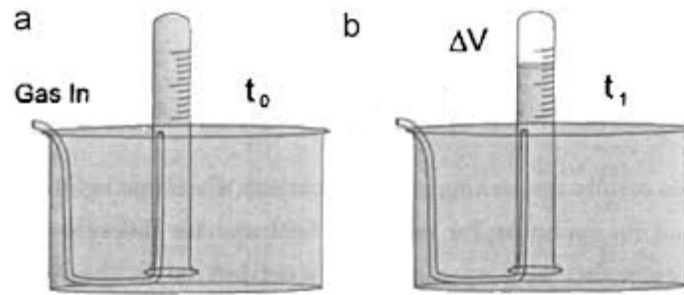
**Figure 5.6:** MFC calibration by water downward displacement method.
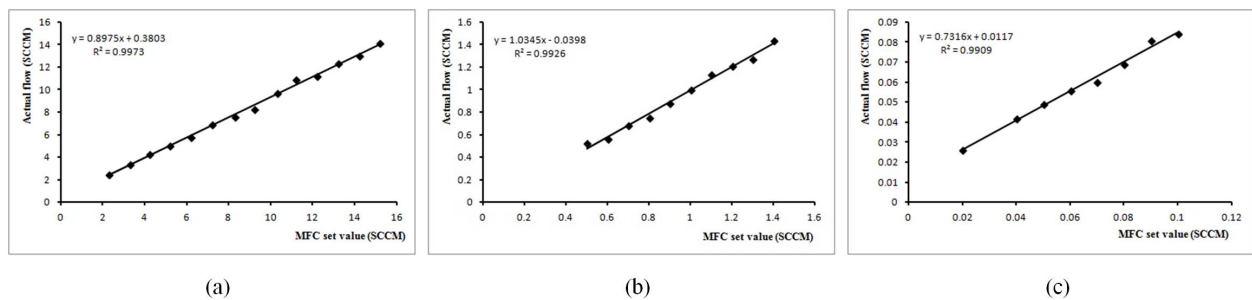


**Figure 5.7:** MFC calibration plots for (a) freon, (b) iso-butane and (c) sulfur hexafluoride gases.

## 5.3   Leak test for RPC

The constructed RPC (section 5.1.3) has to be leak tight from the ambient environmental conditions. The leaks may lead to the ageing of RPC performance [88]. Therefore in order to make sure the constructed RPC is leak tight, the following test was performed. Two opposite corner nozzles of the RPC (figure 5.4d) were blocked with the blockers. One of the other two opposite corner nozzles was used as the gas inlet and the other as gas outlet. The outlet was kept at the atmospheric pressure using FESTO PUN-6×1 tubing. The inlet of RPC was connected to the freon gas cylinder and the air inside RPC was flushed out. Then, the RPC gap was filled with freon gas and the inlet was blocked with screw clip. The outlet of RPC was connected to the inlet of manometer filled with water and the outlet of manometer connected to the atmospheric pressure. It was maintained 40 mm water column difference between the pressure in RPC gap and atmospheric pressure. The system was left for about two hours to see if any change in the water column difference. If there is a decrease in the water column difference, that could be due to the RPC leaks. The leaking

locations were identified using RIKEN GH-202F gas leak checker, which is sensitive to freon gas at the atmospheric pressure. These leaking locations were again glued with the adhesive mentioned in section 5.1.3. Then, RPC was allowed for a day to gain handling strength. The above leak test procedure was repeated for the RPC. Finally, the RPC gap proven leak tight only when the manometer water column difference followed the atmospheric pressure changes of a day. The setup used for the RPC leak test is shown in figure 5.8.
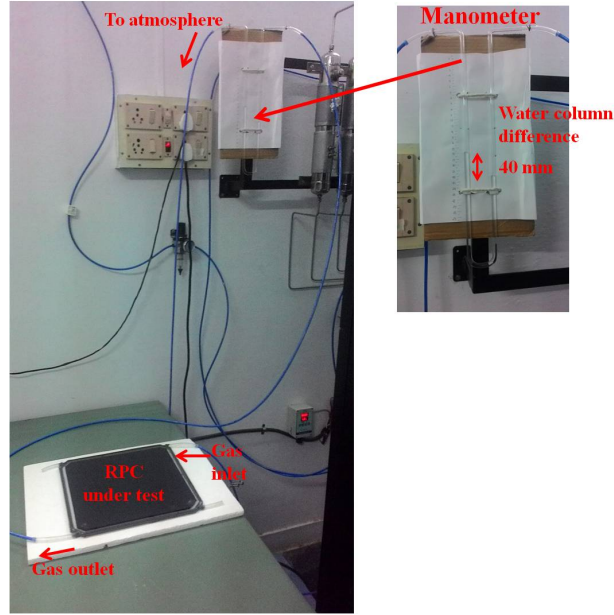


**Figure 5.8:** A setup developed for performing leak test on the RPCs.

## 5.4 Readout system for RPC

A copper tape was pasted at the corners of both the electrodes of leak tight RPC and the high voltage cables were soldered on these tapes. Positive polarity high voltage can be applied to one electrode and the negative polarity to the other, therefore both the electrodes see a common ground. Due to the bipolar connection, each electrode sees only a half of the total applied voltage, thus reducing the chances of high voltage leaks. The soldering of high voltage cable to the RPC electrode is shown in figure 5.9a.

A layer of mylar sheet was placed on the external surface of RPC electrodes. The mylar sheet is a dielectric material and isolate the high voltage from the surroundings. Copper readout-strips of 2.8 cm wide, with 0.2 cm gap between the consecutive strips, were orthogonally mounted on the RPC electrodes.
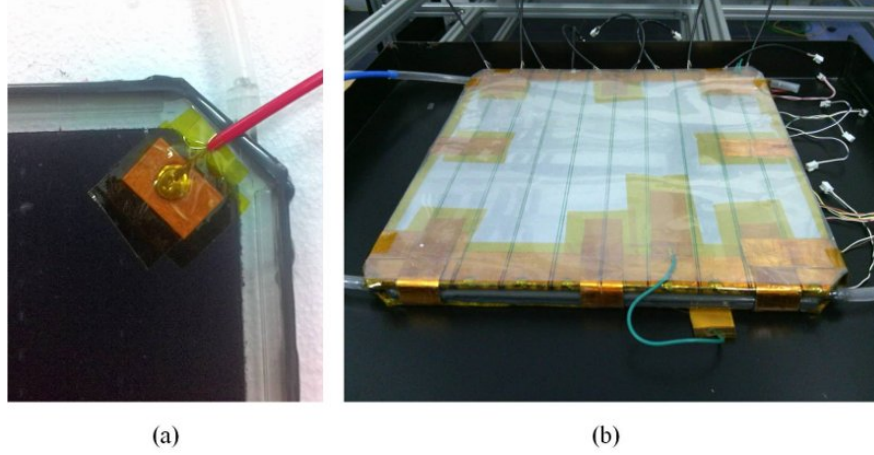


**Figure 5.9:** (a) High voltage cable soldered at the corner of electrode and (b) RPC sandwiched between the copper readout panels.

## 5.5    Characterization of RPCs

Several numbers of $30 \times 30$ cm$^2$ size RPCs were constructed using the glass plates from Asahi and Saint-Gobain manufacturers. The Asahi RPCs and Saint-Gobain RPCs were named as A-RPCs and S-RPCs, respectively. These RPCs were characterized using cosmic-ray muon source and a telescope developed using the scintillator paddles (chapter 4).

### 5.5.1    A cosmic-ray muon telescope setup

A cosmic ray muon telescope was set up using three plastic scintillator paddles to get a 3-fold coincidence. The dimensions of scintillator paddles in length $\times$ width $\times$ thickness are $30 \times 2 \times 1$ cm$^3$ (top), $30 \times 3 \times 1$ cm$^3$ (middle), and $30 \times 5 \times 1$ cm$^3$ (bottom). The RPCs were stacked

between top and middle scintillator paddles. The telescope window that is defined by a 2 cm wide finger paddle was centered on the 2.8 cm wide central strip of the RPC. The developed cosmic-ray muon telescope is shown in figure 5.10. The geometrical muon trigger acceptance cone for two RPCs is shown in figure 5.11.
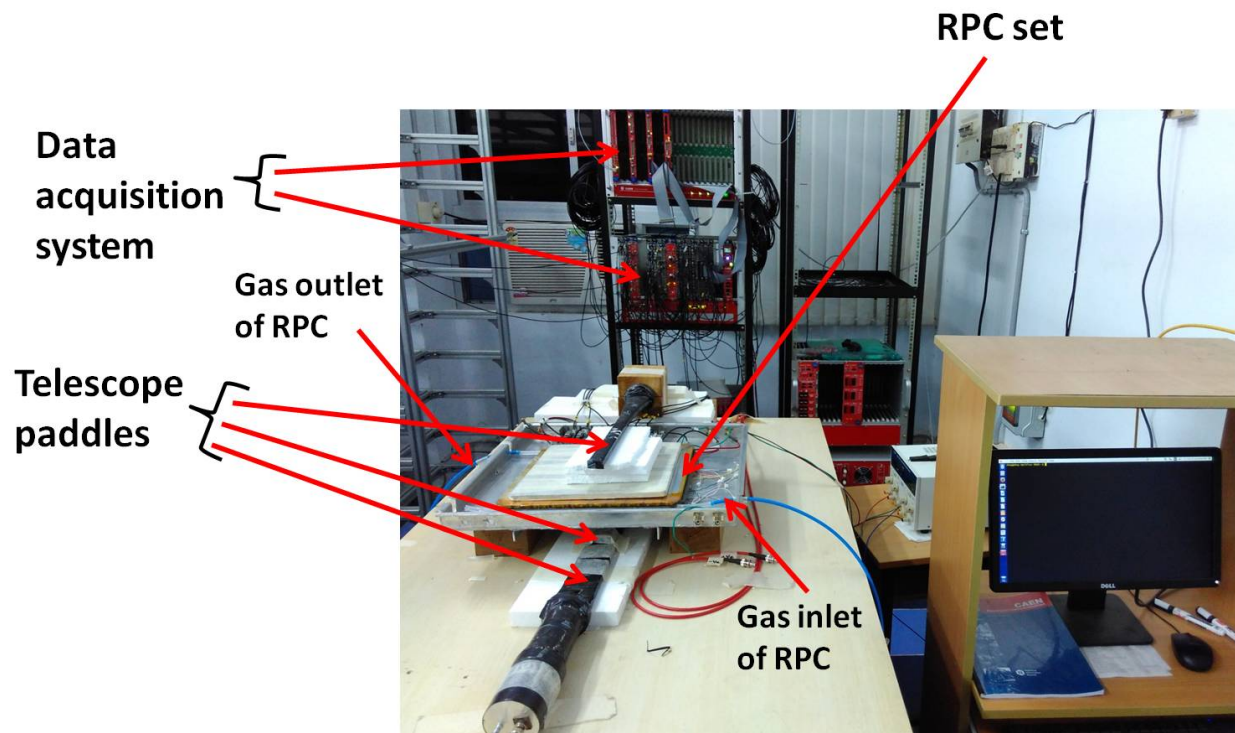


**Figure 5.10:** A cosmic-ray muon telescope arrangement for characterizing the RPCs. The RPC is stacked between top and middle scintillator paddles. The telescope window defining 2 cm wide finger paddle is centered on the 2.8 cm wide central strip of the RPC.

## 5.5.2   Data acquisition system

The scintillator paddles were operated at 1.7 kV (figure 4.15) using Aplab H5KO2N high voltage DC power supply. A –30 mV threshold was applied to the analog pulses of these paddles using PS Model 706 sixteen channel leading edge discriminator. The RPC analog pulses were amplified
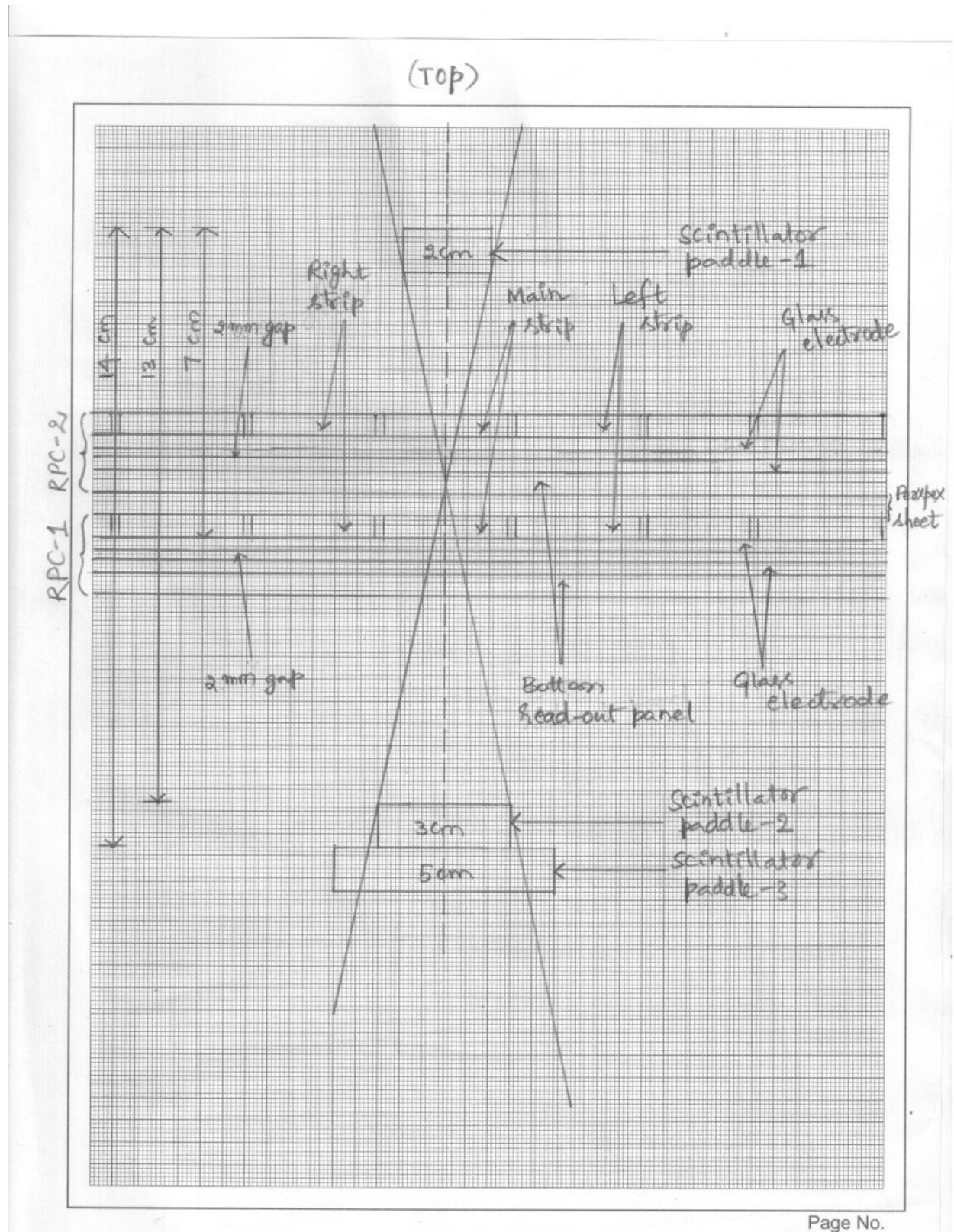
**Figure 5.11:** Geometrical muon trigger acceptance cone for the RPCs.

**Figure 5.12:** A 8-in-1 two-stage Hybrid Micro Circuit (HMC) based high speed preamplifier board.

using indigenously developed 8-in-1 two-stage Hybrid Micro Circuits (HMC) based high speed preamplifier shown in figure 5.12. The measured gain of the pre-amplifier is ∼70 and jitter was a few tens of ps. A –20 mV threshold was applied to the amplified RPC pulses using PS Model 705 octal leading edge discriminator. The logic pulses from both the scintillator paddles and RPCs were analyzed using NIM and VME-based data acquisition (DAQ) system (figure 5.13). The schematic of detailed experimental arrangement of telescope paddles, two RPCs, electronic circuit and DAQ system is shown in figure 5.14.



**Figure 5.13:** (a) NIM and (b) VME-based data acquisition system.
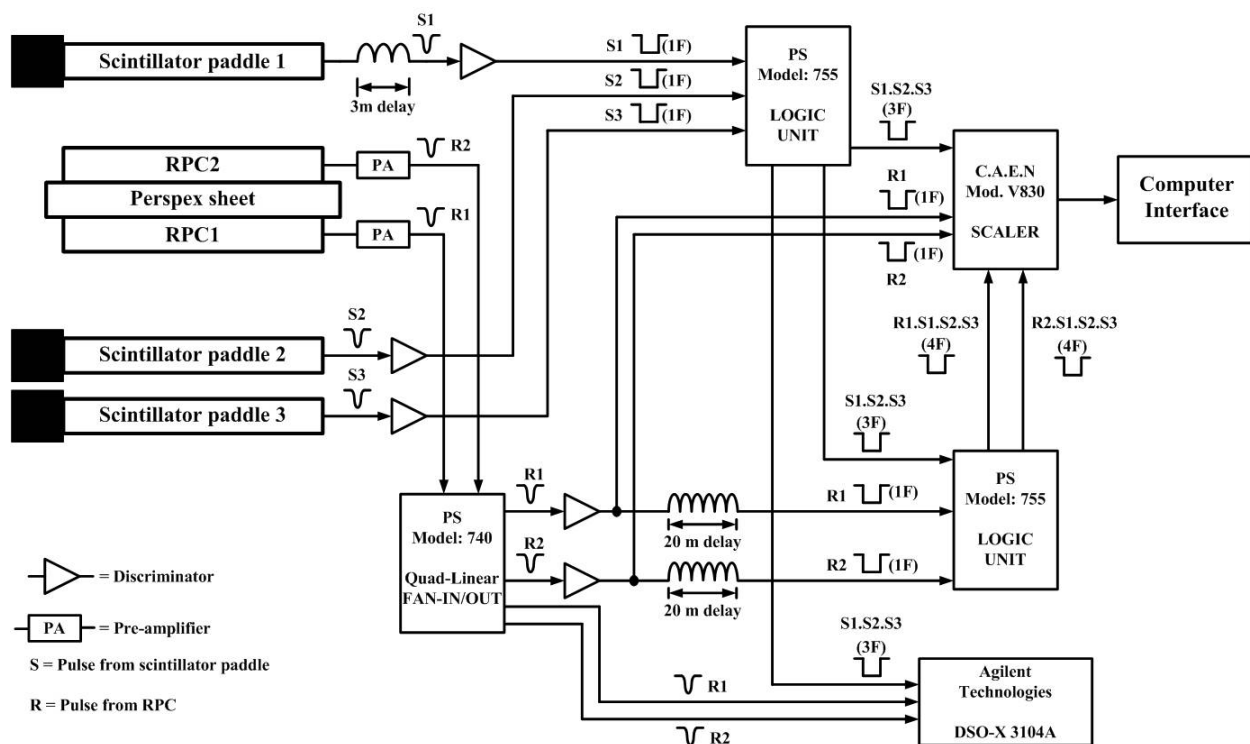
**Figure 5.14:** Schematic of the experimental arrangement for characterizing the RPCs.

### 5.5.3 Test results

An optimized gas mixture of $C_2H_2F_4$/iso-$C_4H_{10}$/$SF_6$ = 95/4.5/0.5 was flown through the RPCs with a total flow rate of 10 SCCM and operated in the avalanche mode. The schematic of the gas flow system for two RPCs is shown in figure 5.15. The following characterization studies were conducted on the RPCs at ~45% relative humidity (RH) and 20 °C temperature. These are the optimized ambient RH and temperature conditions for operating the INO-ICAL RPCs.

**Voltage-current characteristics**

The simple electrical equivalent circuit representation of a single gap RPC is shown in figure 5.16. The RPC gas gap is represented by a parallel combination of spacer resistance and gas ionization volume of the gap (represented by a Zener diode) [52]. Therefore, for a given bulk resistivity of the spacers, the current flowing in the circuit depends on the bulk resistivity of RPC electrodes.
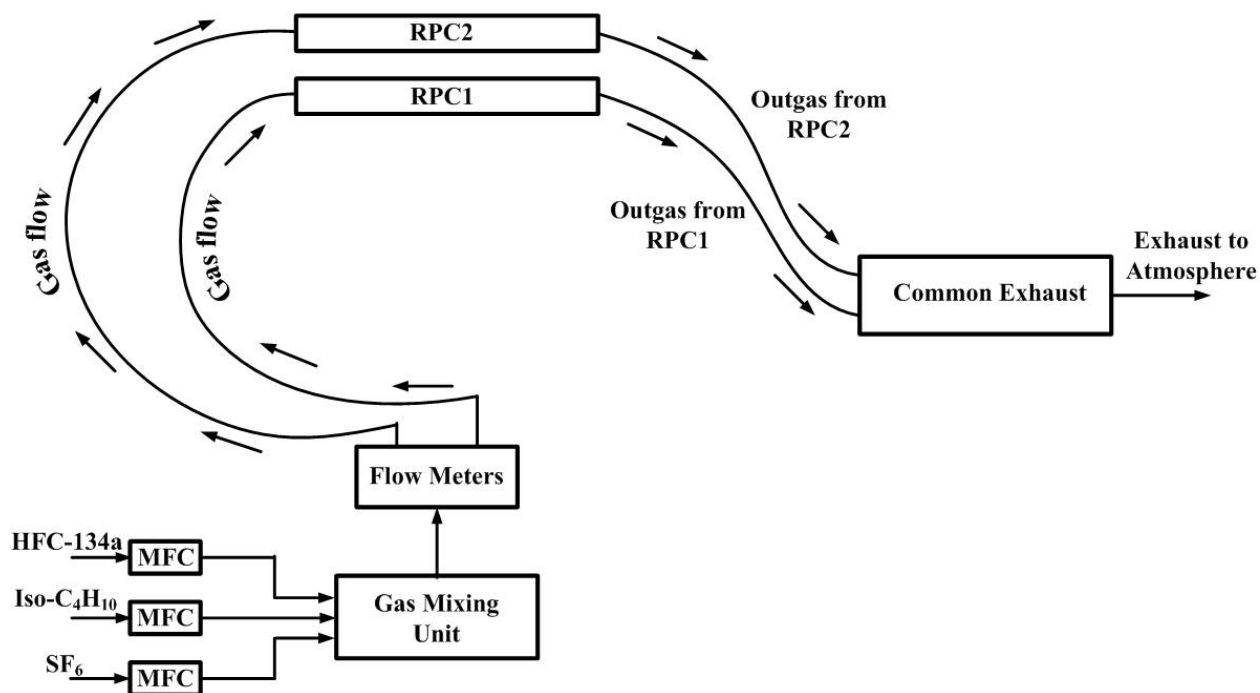
**Figure 5.15:** Schematic of the gas flow system for operating two RPCs.
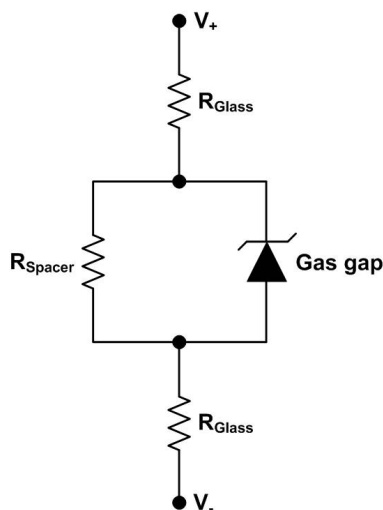


**Figure 5.16:** Electrical equivalent circuit representation of a single gap RPC.

The voltage-current characteristics of RPCs was measured using C.A.E.N Mod. N471A, 2 channel HV Power Supply. The current resolution of module is 1 nA. The currents drawn by RPCs

as a function of applied voltage are shown in figure 5.17. A-RPCs were found to draw lower bias currents compared to S-RPCs. This could be because of Asahi glass showed larger bulk resistivity compared to Saint-Gobain glass (table 3.3).
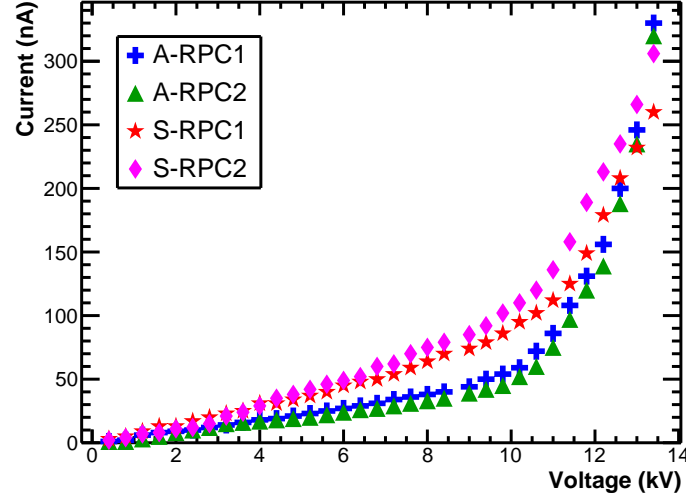


**Figure 5.17:** Currents drawn by the RPCs as a function of voltage.

**Efficiency studies**

The normal vector component of the electric field displacement is continuous at the electrode/gas interface of RPC. This boundary condition is expressed as:

$$\mathbf{D} = \varepsilon_p \mathbf{E_p} = \varepsilon_g \mathbf{E_g}, \tag{5.1}$$

where, $\varepsilon_p$ and $\varepsilon_g$ are the permittivities, and $\mathbf{E_p}$ and $\mathbf{E_g}$ are the electric fields of the electrode plate and the gas gap, respectively [77, 89]. From equation 5.1, it indicates that the RPCs made out of electrodes with larger relative permittivity (section 3.6.2) can be operated at lower bias voltages.

The experimental arrangement and electronic circuit for measuring the efficiencies of RPCs is shown in figure 5.14. The oscilloscope trace of pulses produced from the RPCs and the telescope trigger pulse are shown in figure 5.18. The efficiency measurements on RPCs were performed using C.A.E.N Mod. V830 Scaler. The telescope trigger pulse was recorded as 3-fold pulse. The

79

efficiency is defined as the ratio of the number of coincident pulses of RPC strip with that telescope trigger (i.e., 4-fold pulses) to the number of trigger pulses (3-fold pulses). This definition is written as:

$$\text{Efficiency} = \frac{\text{4-fold (4F) rate}}{\text{3-fold (3F) rate}} \times 100\%, \tag{5.2}$$

where, 3F is the telescope trigger pulse, which is generated by time coincidence of three scintillator counters, and 4F is the coincidence pulse of RPC under test and telescope trigger pulse.

The measured efficiency of RPCs as a function of applied high voltage are shown in figure 5.19. The four RPCs showed greater than 95% efficiency on the plateau. It is observed that the knee of efficiency plateau of A-RPCs starts at 10.8 kV, whereas that of S-RPCs starts at 12.0 kV. Therefore, A-RPCs can be operated at 1.2 kV lower bias voltage in comparison to S-RPCs. These results are in consistent with equation 5.1.
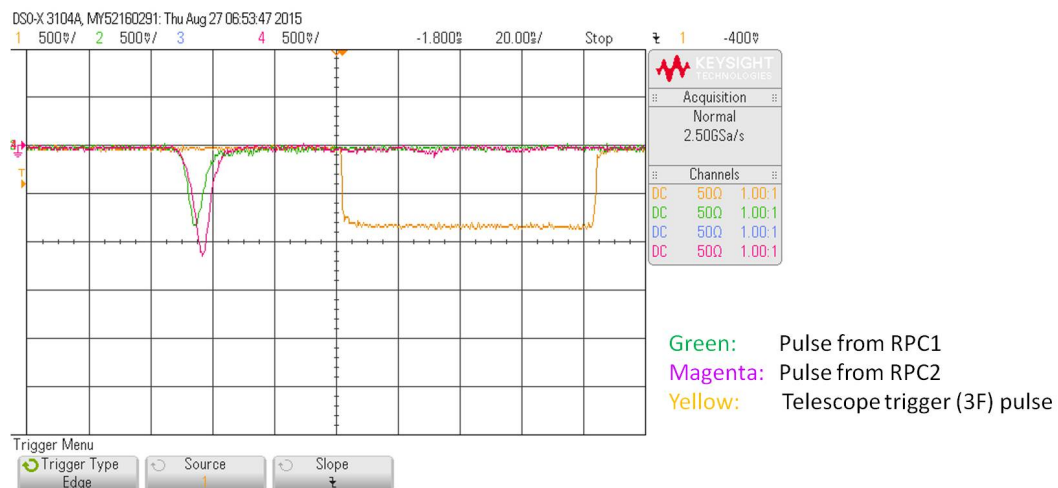


**Figure 5.18:** The Oscilloscope trace of pulses produced from RPC1, and RPC2 and the telescope trigger pulse.
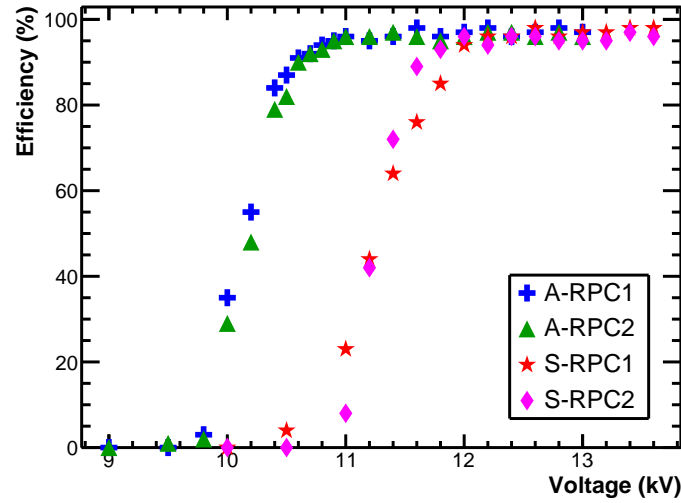
**Figure 5.19:** Efficiency of the RPCs as a function of high voltage.

**Time resolutions of the RPCs**

From equation 5.1, it is clear that for a given applied voltage, the RPC made out of electrodes with larger relative permittivity will generate a larger electric field in the gas gap. Therefore, the drift velocity of avalanche electrons will be greater, which leads to better time resolutions [90, 91].

The RPCs were operated at 12.0 kV, where they showed greater than 95% efficiency, and measured their time resolutions as follow. As shown in figure 5.14, the pulse from scintillator paddle 1 (S1) is delayed for 15 ns (3 m), using RG174 coaxial cable, and is used to produce the trigger pulse. Using this trigger pulse, the RPC pulses were recorded on the Agilent DSO-X 3104A. Therefore, here, S1 is the start counter (T0) to detect the RPC pulses. The time differences between the trigger pulse and RPC pulse were noted on around 1100 triggers and plotted the time distribution histogram. The plotted histograms are shown in figure 5.20. The obtained sigma from histogram is the quadratic sum of resolution of RPC and resolution of S1, i.e.,

$$\sigma = \sqrt{\sigma_{RPC}^2 + \sigma_{S1}^2} \implies \sigma_{RPC} = \sqrt{\sigma^2 - \sigma_{S1}^2}, \tag{5.3}$$

where, $\sigma$ is the resolution obtained from the histogram, $\sigma_{RPC}$ is the resolution of RPC and $\sigma_{S1}$ is the resolution of S1 = 0.74 ns.

Using equation 5.3, the time resolutions of A-RPC1, A-RPC2 are 1.64, 1.53 ns, and that of S-RPC1, S-RPC2 are 2.21, 2.17 ns, respectively. The time resolutions of A-RPC1 and S-RPC1 at their operating voltages 11 kV and 12.2 kV are 1.71 and 2.14 ns, respectively.
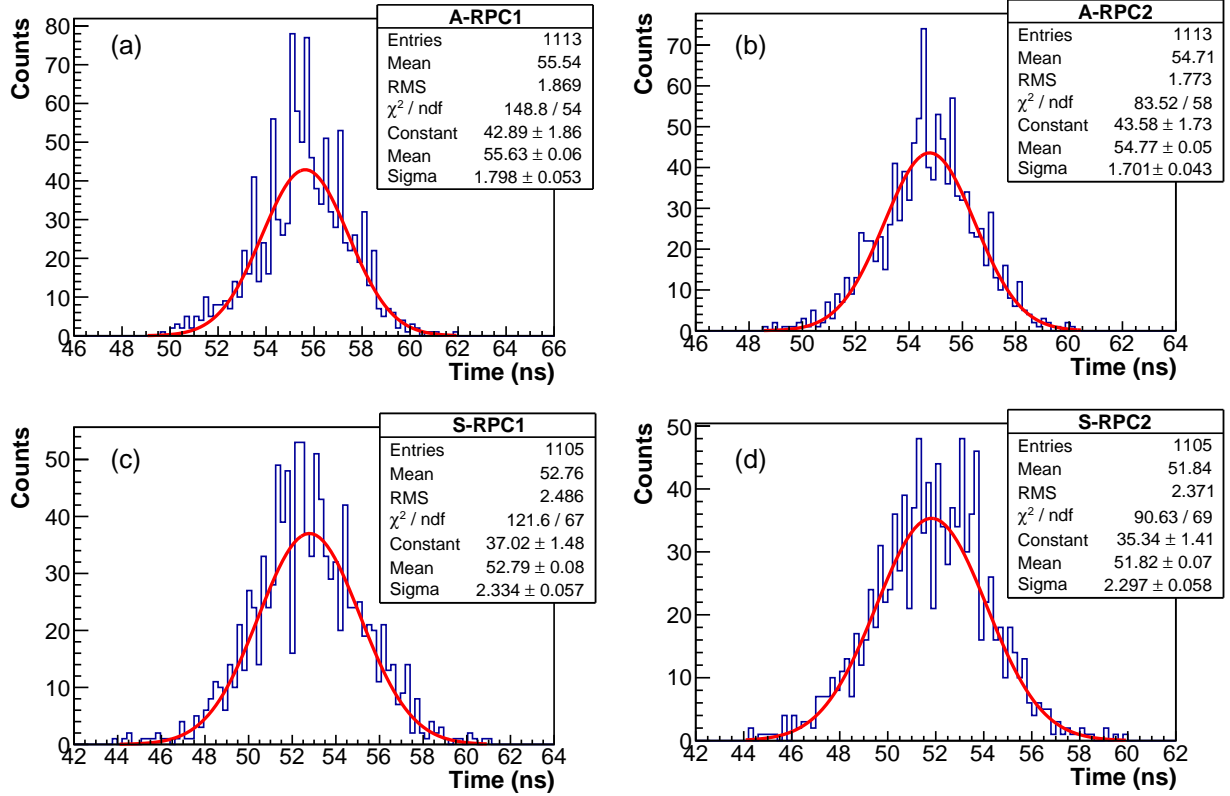


**Figure 5.20:** Time resolutions of the RPCs at 12 kV: (a), (b) A-RPCs; (c), (d) S-RPCs.

**Signal charge of the RPCs**

The analog pulses from Asahi RPC at 11 kV and Saint-Gobain RPC at 12.2 kV were recorded on Agilent DSO-X 3104A. The selected operating voltages were 200 V upstream of the knee of efficiency plateau (figure 5.19) of each RPC, respectively. These pulses were integrated and measured the signal charge of RPCs. The results are shown in figure 5.21. The obtained mean values from the charge distributions of Asahi and Saint-Gobain RPCs are 1.53 and 1.86 pC, respectively. The ratio of these means, i.e., 1.86/1.53 is close to the inverse ratio of the relative permittivities of the corresponding electrodes, i.e., 16.6/11.7 (figure 3.4).
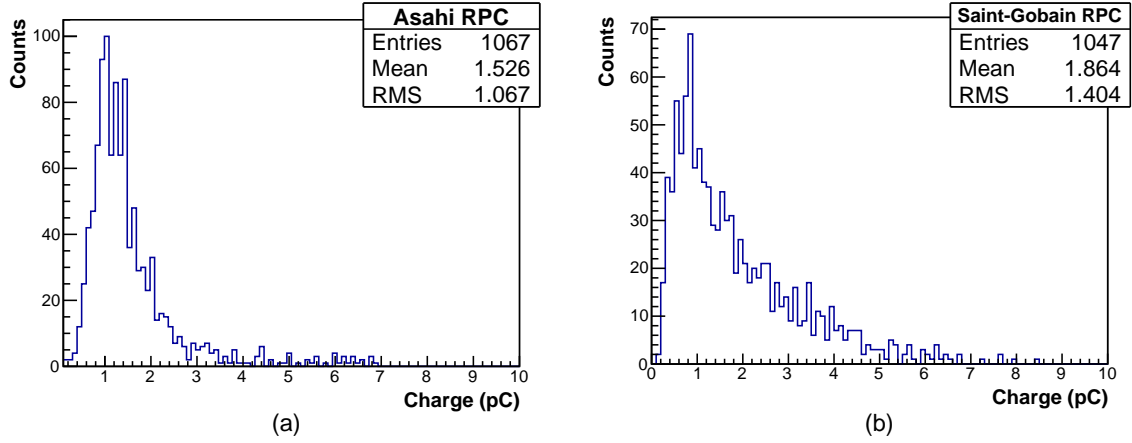
**Figure 5.21:** Mean signal charge of: (a) Asahi RPC at 11 kV and (b) Saint-Gobain RPC at 12.2 kV.

**Counting rate capability of the RPCs**

The relaxation time of RPC electrode is $\tau = RC = \rho \varepsilon_0 \varepsilon_r$. Therefore, as per the relative permittivity measurements in figure 3.4, we expect that under identical conditions Saint-Gobain RPCs offer better counting rate capability compared to Asahi RPCs. Even though, it is not of consequence in the case of INO-ICAL experiment, where the expected counting rate is much lower.

## 5.6   Chapter summary

Several numbers of $30 \times 30$ cm$^2$ RPCs were developed using the float glass plates from Asahi and Saint-Gobain manufacturers. The mass flow controllers were calibrated for freon, iso-butane and sulfur hexafluoride gases. Leak tests were performed on the constructed RPCs to make sure that they were leak tight from ambient environmental conditions. A cosmic-ray muon telescope was set up for characterizing the RPCs. Asahi RPCs were found to draw lower bias currents compared to Saint-Gobain RPCs. The knee of efficiency plateaus of Asahi RPCs and Saint-Gobain RPCs started at 10.8 and 12.0 kV, respectively. Therefore, Asahi RPCs can operate at 1.2 kV lower bias voltage in comparison to Saint-Gobain RPCs. At a given high voltage, Asahi RPCs showed better time resolutions compared to Saint-Gobain RPCs. Our study shows that the RPC made using Asahi glass will be better suited for the INO-ICAL detector.

<div align="center">83</div>

# Chapter 6

# Effect of water vapor on the performance of glass RPCs

The INO-ICAL RPCs will be operated in the avalanche mode with an optimized gas mixture of $C_2H_2F_4$/iso-$C_4H_{10}$/$SF_6$ = 95.2/4.5/0.3% [53]. The experiment is expected to run for more than 10 years in order to record statistically significant number of neutrino interactions to measure the neutrino mass hierarchy. Therefore, long-term stability and performance of the RPCs over the duration of the experiment are of prime concern.

About 200,000 liters of gas is going to be circulated in the RPCs during the experiment. The gas lines of about 135 km in total length are going to supply (receive) gas to (from) the RPC detectors. In spite of stringent QC during the RPC gas gap making or gas lines plumbing, it is impossible to prevent ambient air or water vapor entering into the gas circuit over these long periods of time. The contaminants are known cause for serious degradation in the performance or permanent damage of the RPCs. The studies reported in the literature [74, 92, 93, 94] indicate that while the RPCs are operating with the water vapor contamination, the decomposed freon ($C_2H_2F_4$) gas in the RPC can react with water vapor and produce hydrogen fluoride (HF). HF is an aggressive acid and is believed to play a major role in damaging the inner surface of RPC electrodes.

Considering the possibility of severe repercussions in the mammoth ICAL detector, a systematic study of this problem was undertaken [95]. Two glass RPCs of $30 \times 30$ cm$^2$ size (built using Saint-Gobain glass) were simultaneously operated with standard gas mixture in one and with gas mixture along with controlled amount of water vapor in the other. A common cosmic ray muon telescope was used for studying both the RPCs. Ambient parameters such as temperature and relative humidity (RH) as well as RPCs operating and performance parameters such as currents, efficiencies, singles rates, signal charges and time resolutions for cosmic ray muon detection were systematically recorded throughout the experiment. A significant deterioration was observed in the performance of RPC in which gas with water vapor was flown.
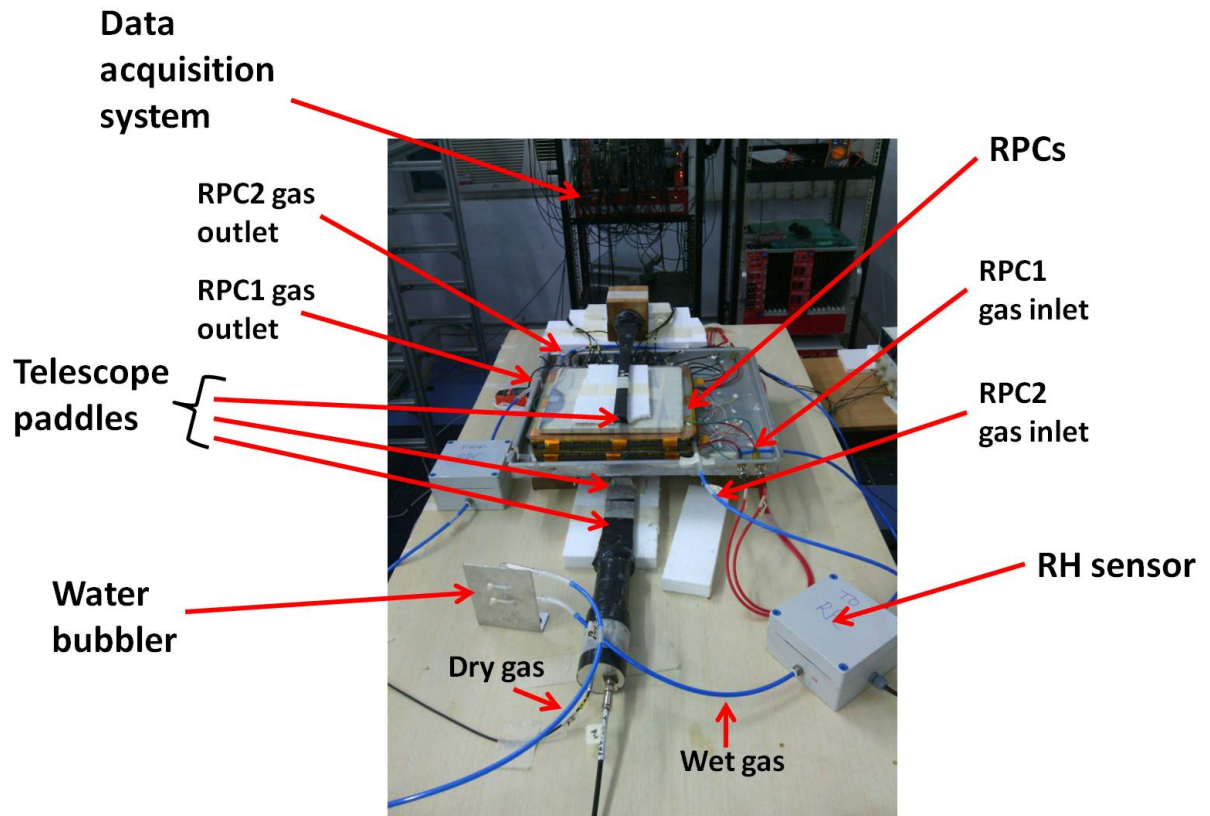


**Figure 6.1:** Schematic of the experimental arrangement for the effect of water vapor studies on glass RPCs in the avalanche mode operation.

# 6.1    Experimental setup

The cosmic-ray muon telescope, which was developed for characterizing the $30 \times 30$ cm$^2$ RPCs in section 5.5.1 was used for performing these studies. The detailed experimental arrangement is shown in figure 6.1 and its schematic is shown in figure 5.14. The schematic of gas flow system is shown in figure 6.2.
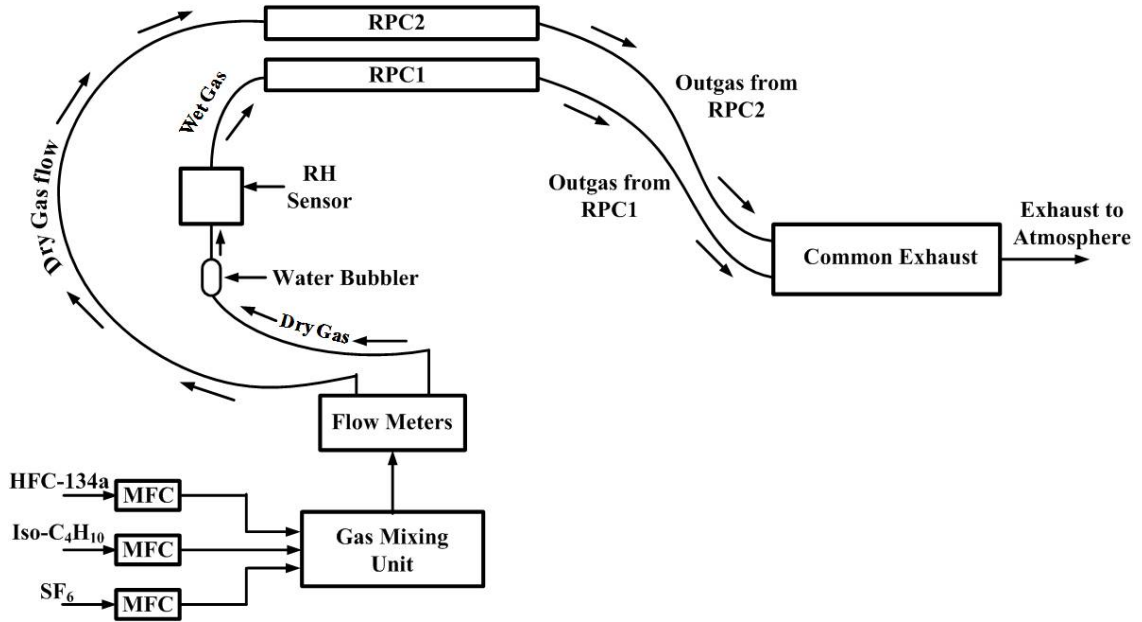


**Figure 6.2:** Schematic of the gas flow system for RPC1 operated with the wet gas and RPC2 operated with the standard (dry) gas.

# 6.2    Measurements and observations

## 6.2.1    Standard gas studies

The RPCs were operated with the standard (dry) gas at 10 SCCM rate and their currents, efficiencies and singles rates as a function of applied voltage were measured. The measured efficiencies of RPC1 and RPC2 as a function of applied voltage are shown in figure 6.3. The detectors showed greater than 95% efficiencies on the plateau. The measured signal charges and time resolutions of

the detectors are shown in figure 6.4. At the operating voltage of 12.2 kV, the signal charges of RPC1 and RPC2 are found to be 0.99 and 1.24 pC, and the time resolutions are 2.8 and 2.3 ns, respectively.

Then, the RPCs were operated at 12.2 kV and their performances monitored for 32 days. The efficiencies, singles rates and operating currents of the detectors for this time period are shown in figure 6.5. Their performances were stable throughout the period.

## 6.2.2    Wet gas studies

The water vapor was added to RPC1 gas mixture using a water bubbler as shown in figure 6.2. The amount of water vapor in the gas mixture was measured in a controlled way using a RH sensor and is shown in figure 6.6. Throughout these studies, RPC2 was continued with the standard gas flow itself and was a reference detector. Then, the performances of both the detectors were monitored continuously.

The Oscilloscope trace of pulses produced from RPC1 and RPC2 with standard gas operation are shown in figure 5.18. The pulses produced from RPC1 with wet gas operation and from RPC2 with standard gas operation are shown in figure 6.7. In the case of RPC1 operating with wet gas, the avalanche pulse was accompanied by an after-pulse with a delay of ∼10 ns. This after-pulse is could be due to the huge number of photons produced from the ionization and excitation of water
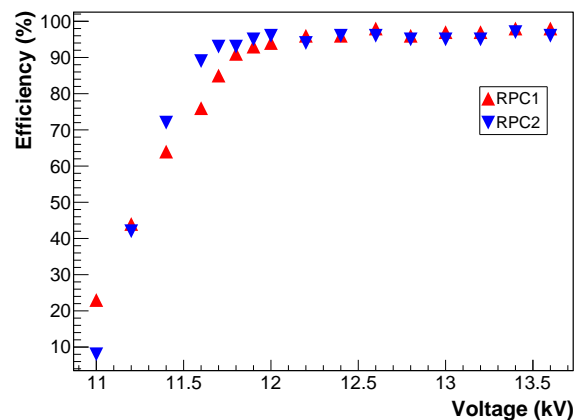


**Figure 6.3:** Efficiency of RPC1 and RPC2 with the standard gas operation as a function of applied voltage.
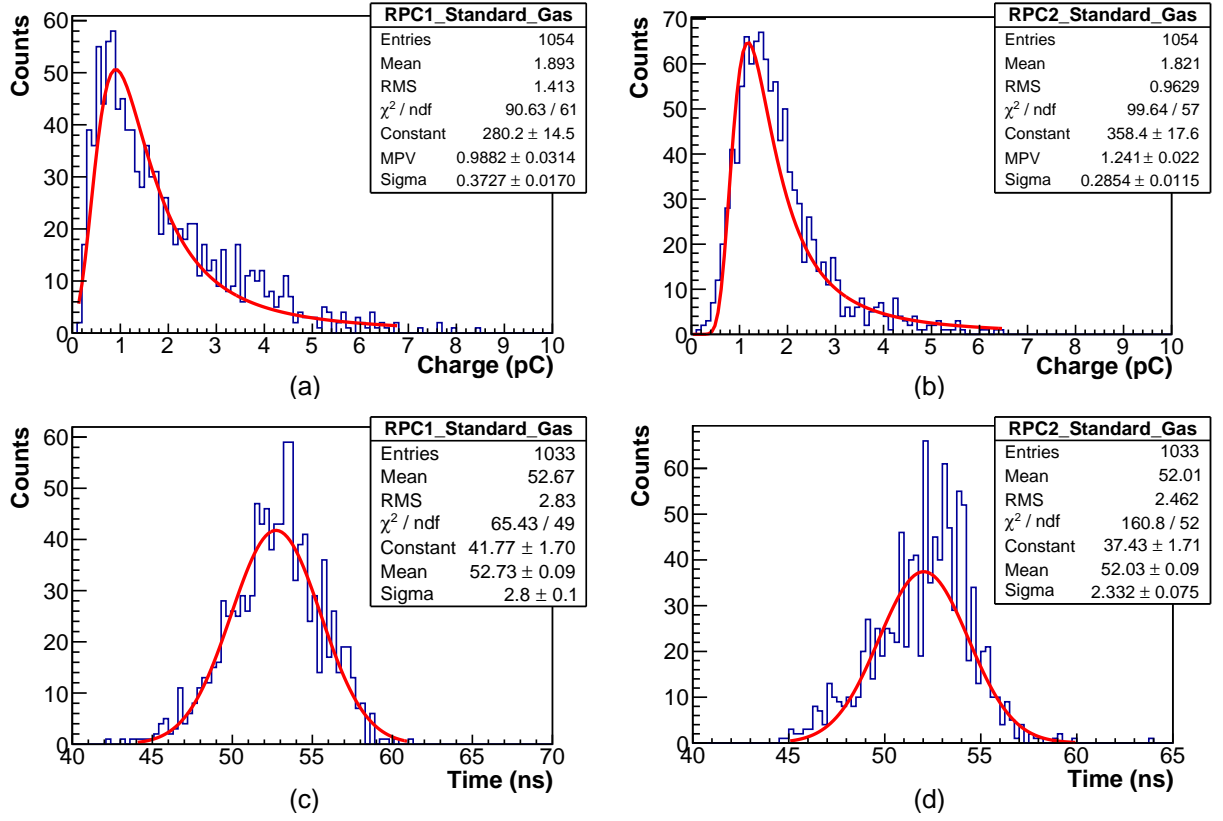
**Figure 6.4:** Signal charge: (a) and (b), and time resolution: (c) and (d) of RPC1 and RPC2, respectively, with the standard gas operation at 12.2 kV.
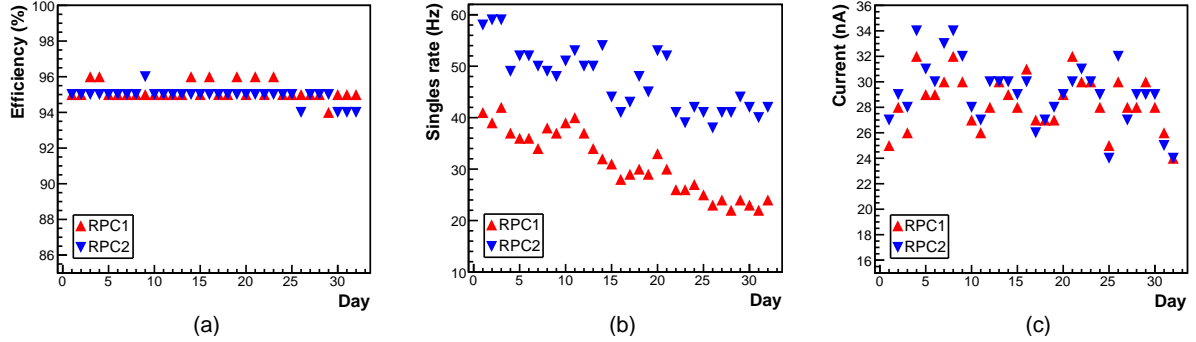


**Figure 6.5:** (a) Efficiency, (b) singles rate and (c) current of both the RPCs with the standard gas operation for 32 days.

molecules by the charged particles passing through the gas gap.

With the wet gas operation for a few days, the efficiency and singles rate of RPC1 degraded to
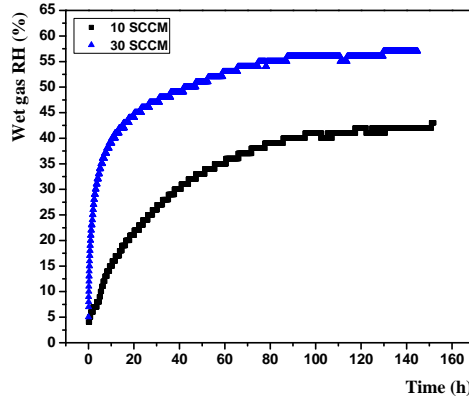
**Figure 6.6:** The quantity of water vapor addition to RPC1 for 10 SCCM and 30 SCCM gas flow rates.
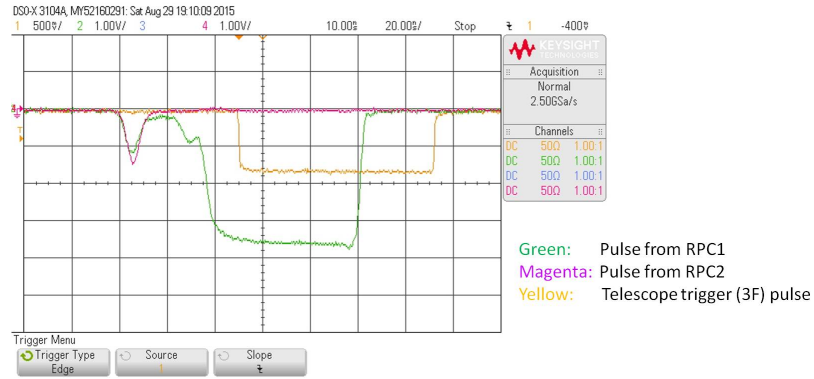


**Figure 6.7:** The Oscilloscope trace of pulses produced from RPC1 with the wet gas operation and from RPC2 with the standard gas operation. In the case of RPC1 operating with wet gas, the avalanche pulse was accompanied by an after-pulse with a delay of $\sim$10 ns.

0% and 1 Hz, respectively. The currents drawn by the detector increased gradually with time. The efficiency, singles rate and current drawn by RPC1 during the wet gas operation in comparison to RPC2 operated with the standard gas is shown in figure 6.8.

The signal charge of RPC1 became smaller (0.36 pC) with the wet gas operation, whereas that of RPC2 with the standard gas operation (1.19 pC) remained similar to its measured value shown in figure 6.4b (1.24 pC). The signal charge distributions of RPC1 with the wet gas and RPC2 with the standard gas operations are shown in figures 6.9a and 6.9b, respectively.

**90**
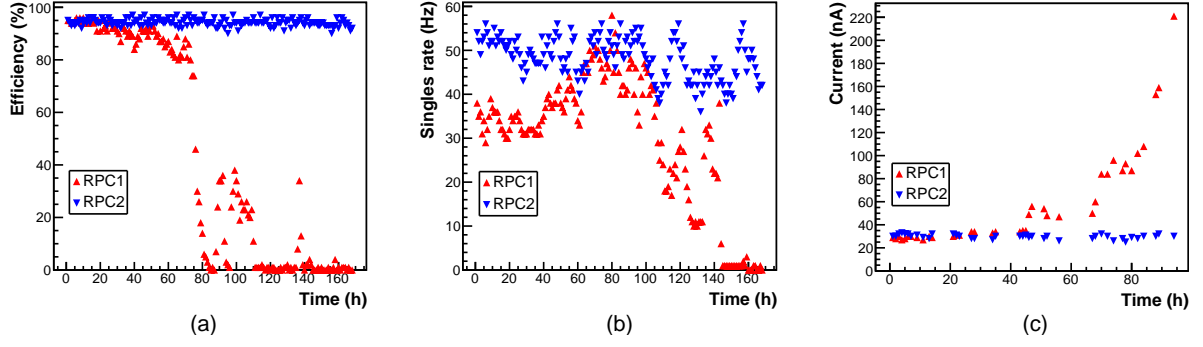
**Figure 6.8:** (a) Efficiency, (b) singles rate and (c) current of RPC1 with the wet gas operation, and those of RPC2 with the standard gas operation.
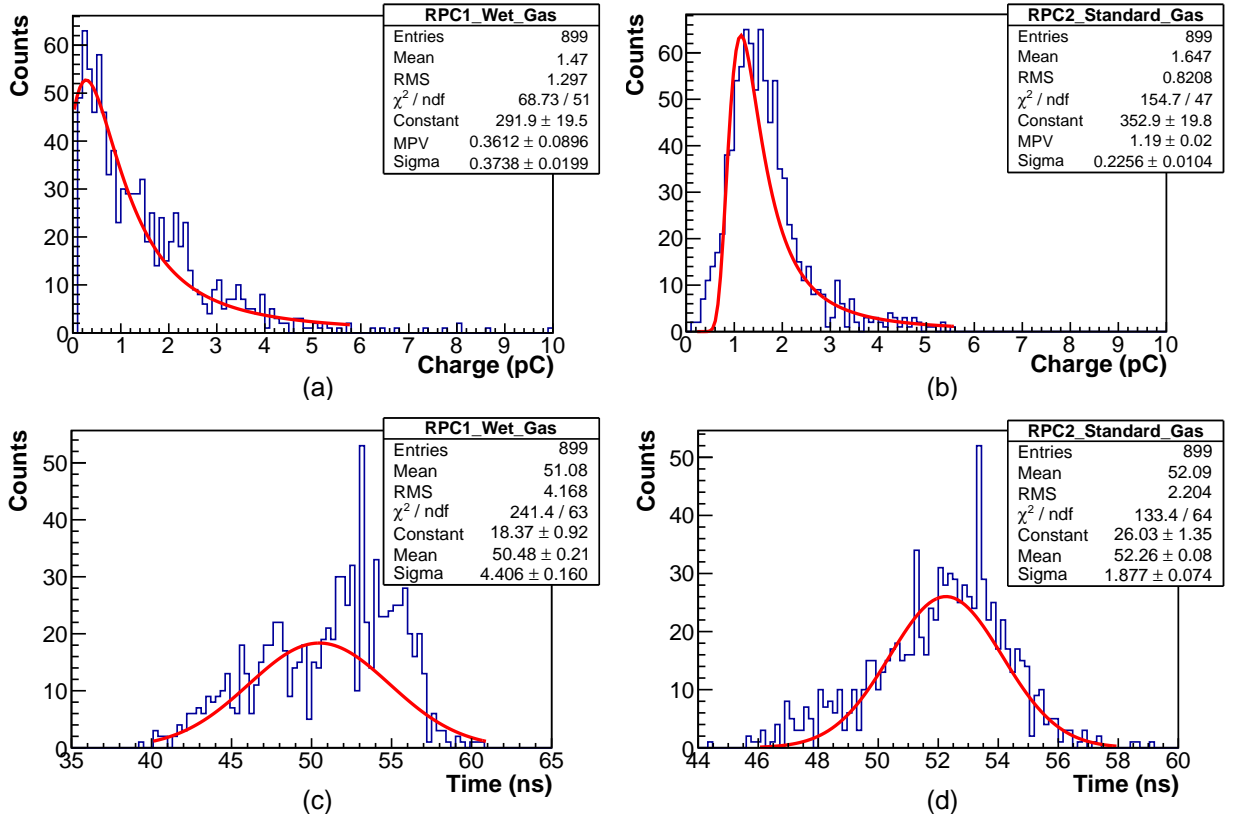


**Figure 6.9:** Signal charge of: (a) RPC1 with the wet gas operation and (b) RPC2 with the standard gas operation, and time resolution of: (c) RPC1 with the wet gas operation and (d) RPC2 with the standard gas operation.

The timing distribution of RPC1 with the wet gas operation deteriorated as shown in figure 6.9c.

Whereas, that of RPC2 with the standard gas operation (1.9 ns) remained similar to its measured value shown in figure 6.4d (2.3 ns).

### 6.2.3   Recovery studies

RPC1 was operated with the wet gas at various flow rates and the deterioration in the detector's efficiency was observed as a function of time. It was observed that higher the flow rate, faster the deterioration as shown in figure 6.10a. The detector was operated with the wet gas at 0% efficiency for a day and then switched to the standard gas. Then, the efficiency of detector recovered to greater than 95% in less than an hour as shown in figure 6.10b.
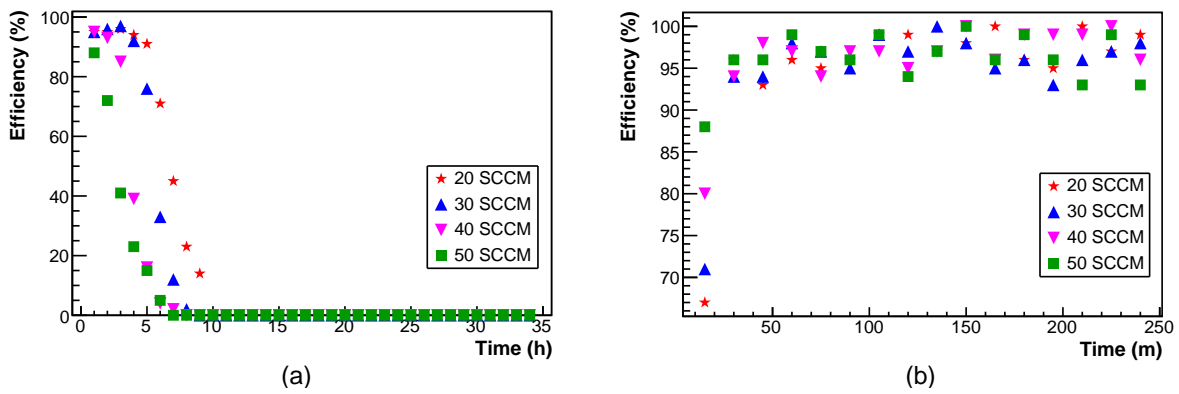


**Figure 6.10:** (a) Deterioration in efficiency of RPC1 with wet gas operation at various flow rates and (b) its recovery with standard gas operation.

## 6.3   Chapter summary and discussions

The effect of water vapor on the performance of glass RPC in the avalanche mode operation was studied. We used the optimized gas mixture of $C_2H_2F_4$/iso-$C_4H_{10}$/$SF_6$ = 95/4.5/0.5 for the studies. The detector showed greater than 95% efficiency with the standard gas operation, its signal charge and time resolution were 0.99 pC and 2.8 ns, respectively. The detector's efficiency decreased to 0% after a few days of operation using a gas mixture with a water vapor contamination larger

than 1000 ppm (1110 ppm is equal to 7.25% of RH). Its signal charge became 0.36 pC and timing distribution deteriorated. The RPC was operated at 0% efficiency with the wet gas for a day and then switched to the standard gas, recovering back to an efficiency greater than 95%. Therefore, it indicates that no damages occurred to the inner surfaces of RPC electrodes.

These results are similar to the performance of type III chambers discussed in Ref. [92]. In the studies, the RPCs were operated in the streamer mode. If the RPCs were operated with higher level of water contamination (> 1000 ppm), they stopped generating the signals after a short period of time and recovered fully after returning to dry gas. In the present studies, we could reproduce the similar performance of RPCs in the avalanche mode operation.

In the case of type I chambers in Ref. [92], the RPCs were operated with about 1000 ppm of water vapor contamination. After a month time of operation, the performance of RPCs deteriorated and permanent damages to the electrodes were observed. For the avalanche mode operation, the signal discharges in RPC are smaller compared to the streamer mode operation. Therefore, similar permanent damages to the electrodes can be expected to occur after operating the RPCs for several months in the avalanche mode with lower level of water vapor contamination.

# Chapter 7

# A simulation study of the response of ICAL geometry to muons

One of the main aims of the ICAL detector is to address the fundamental issue of neutrino mass hierarchy, i.e., to determine the sign of $\Delta m_{32}^2$ ($= m_3^2 - m_2^2$). This can be achieved by observing the charged-current (CC) interactions of atmospheric muon neutrinos and anti-neutrinos ($\nu_\mu$ and $\overline{\nu}_\mu$) in the ICAL detector. The atmospheric $\nu_\mu$ and $\overline{\nu}_\mu$ produce the muons ($\mu^-$ and $\mu^+$, respectively) from the CC interactions in the detector through either $\nu_\mu \rightarrow \nu_\mu$ or $\nu_e \rightarrow \nu_\mu$ oscillation channels. An accurate determination of the muon energy and direction is crucial to achieve the neutrino oscillation physics goals. As $\nu_\mu$ and $\overline{\nu}_\mu$ pass through the earth matter, they undergo different interactions depending on the mass hierarchy. Hence, the hierarchy may be determined by observing individual event rates for $\nu_\mu$ and $\overline{\nu}_\mu$, which produce $\mu^-$ and $\mu^+$, respectively, in CC reactions. Therefore, the ICAL detector must be optimised to correctly identify the charge of muons [96].

For the ICAL detector, the INO collaboration has proposed two geometries 1) default, where the dead space, due to the support structures in the detector volume, is localized to the neutrino event and 2) staggered, where the support structure is redistributed throughout the volume. The schematics of default and staggered geometries of the ICAL detector are shown in figures 7.1a

and 7.1b, respectively.  In this chapter, the response of these two geometries to muons ($\mu^-$s) was studied and compared using Geant4-based simulation data.  This study can provide valuable input for deciding in mechanical design of the support structure for the ICAL detector.
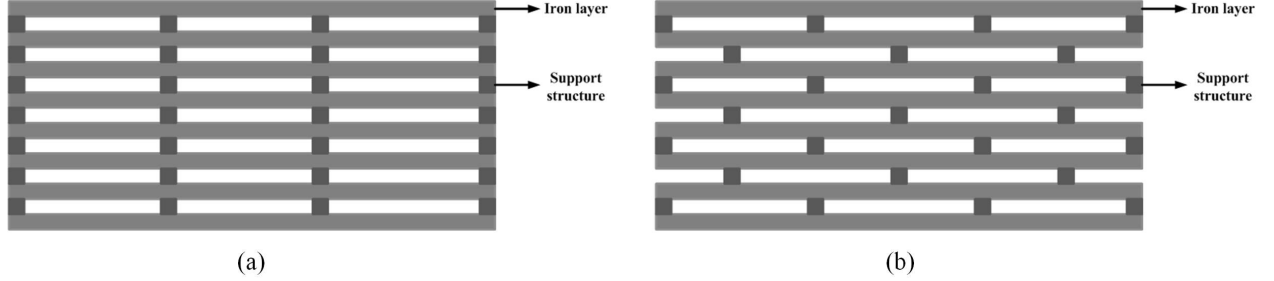


**Figure 7.1:** Schematics of the (a) default and (b) staggered geometries of the ICAL detector.

# 7.1   Simulation framework

The default and staggered geometries for the ICAL detector were developed by the INO collaboration using Geant4-based detector simulation toolkit [97]. A 10000 $\mu^-$s were first propagated inside the detector for both the geometries, taking into account the energy losses, multiple scattering, and magnetic field. This gives the hit positions of the muons in the RPCs. The muons produce tracks in the detector in the presence of magnetic field. The hit position information was digitized and used as an input for the reconstruction of the muon energy and direction. A Kalman Filter-based algorithm was used to reconstruct the muon tracks in the detector [98]. The muon-like tracks must have at least 5 hits in the event [96]. The ROOT data analysis framework was used to analyze the data.

The atmospheric neutrino flux peaks at a few hundred MeVs, and then falls rapidly with neutrino energy with roughly an $E^{-2.7}$ dependence. In contrast, the interaction cross-section increases linearly with energy. The result is that the events in the detector are dominantly of lower energy, below 20 GeV [96]. Here, therefore, the momentum reconstruction efficiency, relative charge identification efficiency, momentum resolution and zenith angular resolution of muons in the 1-25 GeV

momentum regime were studied. The results were compared for both the default and staggered geometries of the ICAL detector.

## 7.2    Response of the ICAL geometry to muons

In the case of default geometry (figure 7.1a), the vertical high energy muon which passes all the way through the support structures losses most of its energy and can be misidentified as low energy muon. This results the wrong information of momentum resolution. Whereas in the case of staggered geometry (figure 7.1b), the support structures are redistributed throughout the detector volume. If the muon misses giving hit in one layer due to the support structure, it gives the hit in the subsequent layer. Which implies no information loss of the event. The reconstructed momentum distributions for 25 GeV $\mu^-$s of the zenith angle $\cos\theta = 0.95$ using the default and staggered geometries of the ICAL detector are shown in figures 7.2a and 7.2b. The momentum misidentified entries of $\mu^-$s are observed at the low momentum region of distribution in the case of default geometry. Whereas, they are correctly identified in the case of staggered geometry.



| (a) | (b) |
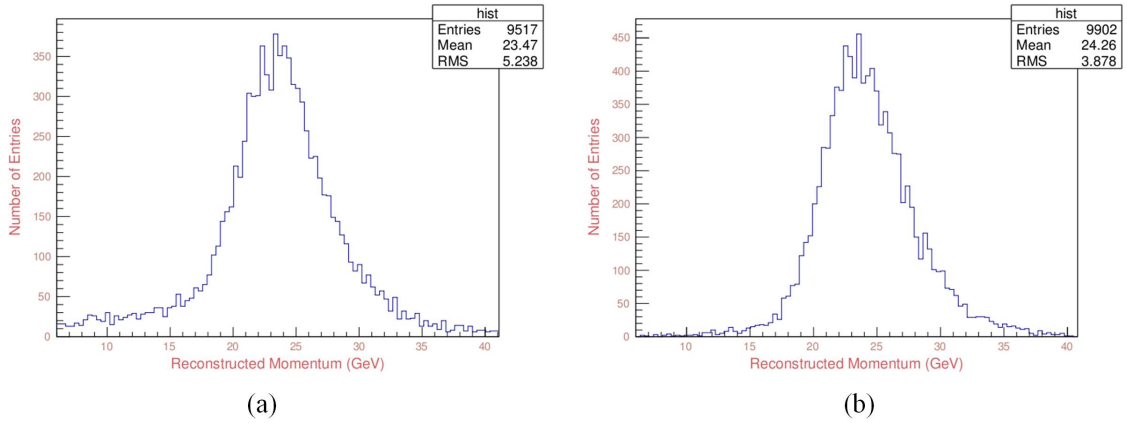
**Figure 7.2:** Reconstructed momentum distributions of 25 GeV $\mu^-$s for the zenith angle $\cos\theta = 0.95$ using (a) default and (b) staggered geometries. The misidentified entries are observed at the low momentum region of default geometry and are correctly identified in the case of staggered geometry.

## 7.2.1  Momentum reconstruction efficiency

The momentum reconstruction efficiencies for $\mu^-$ events of $1 - 25$ GeV momentum regime were computed using both the geometries. The histograms of reconstructed momentum were plotted for the events with the quality of fit such that $\chi^2/ndf < 5$. This quality was obtained by fitting histograms for $5\sigma$ data. The momentum reconstruction efficiency ($E_{rec}$) is defined as following:

$$E_{rec} = \frac{n_{rec}}{N_{total}} \times 100\%, \tag{7.1}$$

and its error is

$$\delta E_{rec} = \sqrt{E_{rec}(1 - E_{rec})/N_{total}} \times 100\%. \tag{7.2}$$

Here, $n_{rec}$ are the number of reconstructed events of the histogram for $5\sigma$ data and $N_{total}$ are the total number of propagated events.
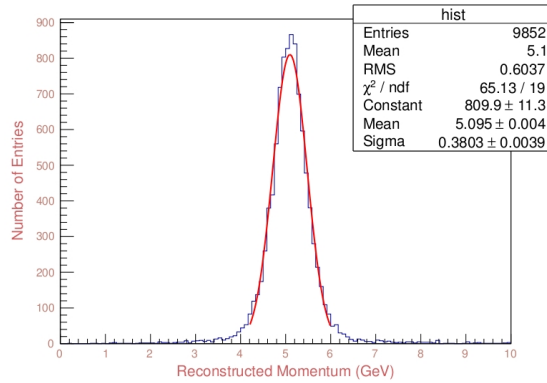


**Figure 7.3:** Reconstructed momentum distribution of 5 GeV $\mu^-$ events for zenith angle $\cos\theta = 0.95$ using staggered geometry.

The analysis was performed for the zenith angles $\cos\theta = 0.65$, 0.85 and 0.95. The histogram of reconstructed momentum for 5 GeV $\mu^-$ events of zenith angle $\cos\theta = 0.95$ using staggered geometry is shown in figure 7.3. The comparison studies of momentum reconstruction efficiencies for $\mu^-$s using the default and staggered geometries are shown in figure 7.4. We observed an

improvement in the $\mu^-$ momentum reconstruction efficiency using the staggered geometry for the zenith angles $\cos\theta = 0.65$ and $0.85$.
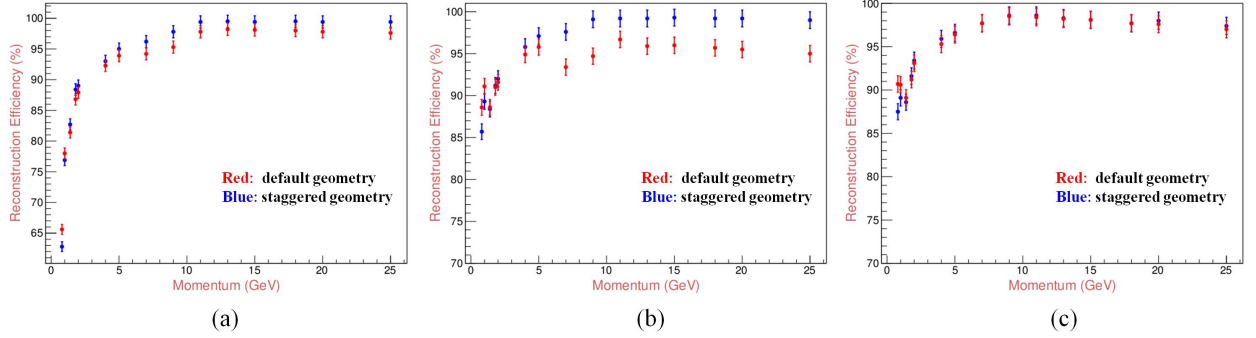


**Figure 7.4:** Comparison of the momentum reconstruction efficiencies for $\mu^-$s using default and staggered geometries of the ICAL detector. The results are for the zenith angles (a) $\cos\theta = 0.65$, (b) $\cos\theta = 0.85$ and (c) $\cos\theta = 0.95$.

### 7.2.2   Relative charge identification efficiency

The charge identification of particle in the magnetic field distinguishes neutrino from anti-neutrino induced events. Hence, it plays a crucial role in the determination of the neutrino mass hierarchy. The charge of the particle is determined from the direction of curvature of the track in the magnetic field. The muon undergoes multiple scattering during propagation in the detector. In the case of small momentum muons, the number of layers with hits is small. This may lead to an incorrectly reconstructed direction of bending in the magnetic field, resulting in the wrong charge identification. The charge miss-identified $\mu^+$ events though 1 GeV $\mu^-$s were propagated inside the detector for $\cos\theta = 0.95$ are shown in figure 7.5.

The relative charge identification efficiency ($E_{cid}$) is defined as following:

$$E_{cid} = \frac{n_{cid}}{n_{rec}} \times 100\%,\qquad(7.3)$$

and its error is

**99**

$$\delta E_{cid} = \sqrt{E_{cid}(1 - E_{cid})/n_{rec}} \times 100\%. \tag{7.4}$$

Here, $n_{cid}$ are the number of events with correct charge identification for $5\sigma$ data and $n_{rec}$ are the total number of reconstructed events.
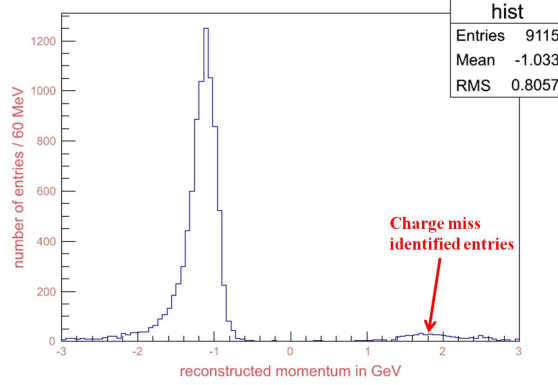


**Figure 7.5:** The charge miss-identified $\mu^+$ events though 1 GeV $\mu^-$s were propagated inside the detector for $\cos\theta = 0.95$.

The analysis was performed for the zenith angles $\cos\theta = 0.65$, 0.85 and 0.95. The comparison studies of relative charge identification efficiencies for $\mu^-$s using the default and staggered geometries are shown in figure 7.6. It was observed that both the geometries showed identical relative charge identification efficiencies for $\mu^-$s.
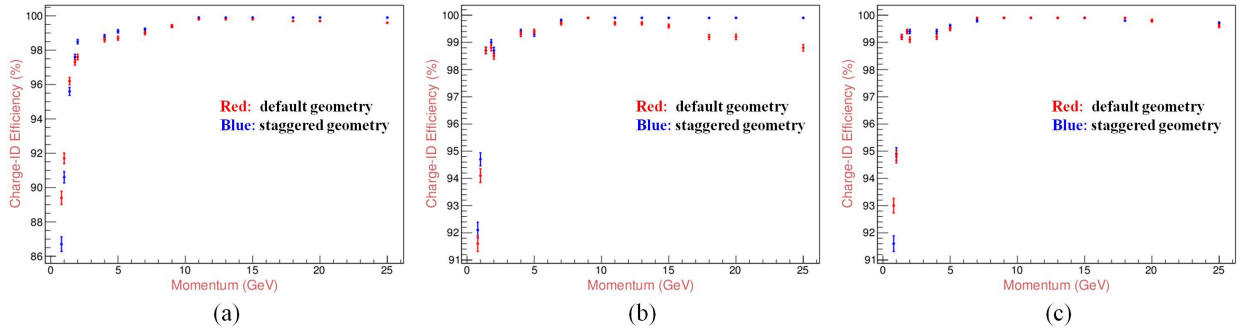


**Figure 7.6:** Comparison studies of the relative charge identification efficiencies for $\mu^-$s using the default and staggered geometries of the ICAL detector. The results are for the zenith angles (a) $\cos\theta = 0.65$, (b) $\cos\theta = 0.85$ and (c) $\cos\theta = 0.95$.

### 7.2.3   Muon momentum resolution

The momentum resolution $(R)$ of the detector is defined as following:

$$R = \frac{\sigma_R}{E_\mu}, \tag{7.5}$$

and its error $(\delta R)$ is

$$\frac{\delta R}{R} = \frac{\delta \sigma_R}{\sigma_R}. \tag{7.6}$$

Here, $\sigma_R$ is the sigma of reconstructed momentum histogram (figure 7.3) and $E_\mu$ is the muon input momentum propagated on the detector. The comparison studies of the muon momentum resolutions for $\mu^-$s using the default and staggered geometries are shown in figure 7.7. The analysis was performed for the zenith angles $\cos\theta = 0.65$, 0.85 and 0.95. The detector showed best momentum resolutions for 7 GeV $\mu^-$s. The staggered geometry showed better momentum resolutions compared to default geometry.
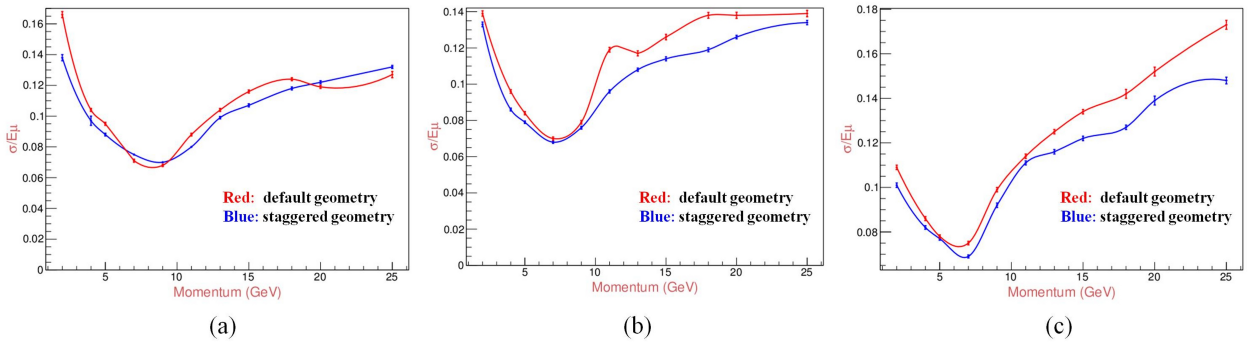


**Figure 7.7:** Comparison studies of the muon momentum resolutions for $\mu^-$s using the default and staggered geometries of the ICAL detector. The results are for the zenith angles (a) $\cos\theta = 0.65$, (b) $\cos\theta = 0.85$ and (c) $\cos\theta = 0.95$.

### 7.2.4   Zenith angle resolution

The zenith angle resolution $(Z)$ is defined as following:

**101**

$$Z = \frac{\sigma_Z}{\cos\theta} \times 100\%,\tag{7.7}$$

where, $\sigma_Z$ is the sigma of reconstructed angular ($\cos\theta$) distribution of the detector as shown in figure 7.8.
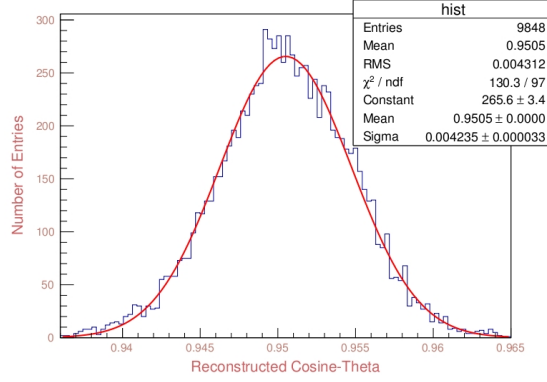


**Figure 7.8:** Reconstructed angular ($\cos\theta$) distribution of 5 GeV $\mu^-$ events for zenith angle $\cos\theta = 0.95$ using staggered geometry.

The analysis was performed for the zenith angles $\cos\theta = 0.65$, 0.85 and 0.95. The comparison studies of the zenith angle resolutions for $\mu^-$s using the default and staggered geometries are shown in figure 7.9. It was observed that both the geometries showed identical zenith angle resolutions for $\mu^-$s.
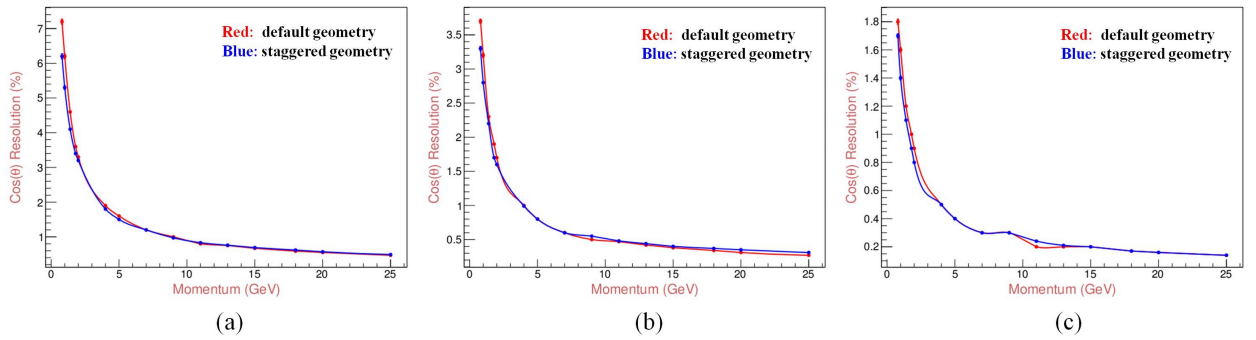


**Figure 7.9:** Comparison studies of the zenith angle resolutions for $\mu^-$s using the default and staggered geometries of the ICAL detector. The results are for the zenith angles (a) $\cos\theta = 0.65$, (b) $\cos\theta = 0.85$ and (c) $\cos\theta = 0.95$.

## 7.3   Chapter summary

For the ICAL detector, the INO collaboration has proposed two geometries 1) default and 2) staggered. The response of both these ICAL geometries to muons ($\mu^-$s) was studied for the detector optimization parameters, *viz.,* momentum reconstruction efficiency, relative charge identification efficiency, momentum resolution and zenith angle resolution. The analysis was performed for the zenith angles $cos\theta$ = 0.65, 0.85 and 0.95 and the results were compared for both the geometries. Staggered geometry showed better $\mu^-$ momentum reconstruction efficiency for the zenith angles $cos\theta$ = 0.65 and 0.85 and better momentum resolutions for the three zenith angles compared to default geometry. Both the geometries showed identical results for relative charge identification efficiency and zenith angle resolutions.

# Chapter 8

# Conclusions and outlook

The India-based Neutrino Observatory (INO) is an upcoming underground project in India. The Iron Calorimeter (ICAL) experiment is one of the INO experimental facilities. The weight of ICAL detector will be 50 kiloton comprising with 1.5 T magnetic field to detect the atmospheric neutrinos and antineutrinos separately. The main aims of ICAL experiment are to make precision measurements on the atmospheric neutrino oscillation parameters and thus to address the fundamental issue of neutrino mass hierarchy. The INO collaboration has chosen $2 \times 2$ m$^2$ size glass resistive plate chambers (RPCs) as the active detector elements for the ICAL detector. The ICAL will use 28,800 such RPCs and they will be operated in the avalanche mode. The experiment is expected to run for more than 10 years in order to record statistically significant number of neutrino interactions to measure the neutrino mass hierarchy. Hence, long-term stability and performance of the RPCs over the duration of experiment are of prime concern.

Operation and performance of the RPC detectors mostly depend on the quality and characteristics of the electrode materials. Therefore, systematic characterization studies were performed on the glasses from Asahi and Saint-Gobain manufacturers. The elemental composition studies showed that Asahi glass is having $\sim 2\%$ larger sodium (Na) component compared to Saint-Gobain glass and therefore Asahi glass showed larger relative permittivity. Asahi glass has larger bulk resisitivity compared to Saint-Gobain glass.

Several numbers of plastic scintillator paddles of the dimensions $30 \times 2 \times 1$ cm$^3$, $30 \times 3 \times 1$ cm$^3$ and $30 \times 5 \times 1$ cm$^3$ were developed and characterized. A cosmic-ray muon telescope was set up using these scintillator paddles. A large number of $30 \times 30$ cm$^2$ RPCs were constructed using the glass plates from Asahi and Saint-Gobain manufacturers. An optimized gas mixture of C$_2$H$_2$F$_4$/iso-C$_4$H$_{10}$/SF$_6$ = 95/4.5/0.5% was flown through the RPCs with a total flow rate of 10 standard cubic centimeters per minute (SCCM) and operated in the avalanche mode. The currect-voltage characteristics, efficiency, signal charge and time resolution of the Asahi and Saint-Gobain RPCs were measured using the telescope. A qualitative agreement in the comparison of RPCs performances and electrical properties of the glasses was observed.

The effect of water vapor on the performance of glass RPC in the avalanche mode operation was studied. With the standard gas operation, the RPC showed greater than 95% efficiency, its signal charge and time resolution were 0.99 pC and 2.8 ns, respectively. With the wet gas (very large contamination of water vapor) operation for a few days, the detector's efficiency decreased to 0%, its signal charge became 0.36 pC and timing distribution deteriorated. The RPC was operated at 0% efficiency with the wet gas for a day and then switched to the standard gas, recovering back to an efficiency greater than 95%.

In the case of RPC was operating with very large contamination of water vapor, it stopped generating the signals after a few days and recovered fully when returned to dry gas. Therefore, it indicates that no damages occurred to the inner surfaces of the RPC electrodes. These studies can be conducted with a water vapor contamination of $\sim$1000 ppm in the RPC gas mixture [92]. The RPC can be operated for several months to observe the deterioration in its performance. It can be expected to occur permanent damages, due to the produced hydrogen fluoride, to the inner surface of RPC electrodes as observed in the streamer mode operation [74, 92]. In this thesis, the studies were performed using $30 \times 30$ cm$^2$ RPCs. In the case of mammoth ICAL detector operation with very huge lengths of gas pipelines, it is impossible to prevent ambient air or water vapor entering into the gas circuit over the long periods of time. Therefore these studies can be extended to $2 \times 2$ m$^2$ RPCs, where we can have the information on RPC performance with water

vapor contamination in beforehand itself.

As part of the INO-ICAL detector simulation studies, the response of default and staggered ICAL geometries to muons ($\mu^-$s) was studied for the detector optimization parameters, *viz.,* momentum reconstruction efficiency, relative charge identification efficiency, momentum resolution and zenith angle resolution. Staggered geometry showed better $\mu^-$ reconstruction efficiencies and momentum resolutions compared to default geometry.

# Bibliography

[1] Alessandro Bettini, Introduction to Elementary Particle Physics, *Cambridge University Press* (2008).

[2] Martinus Veltman, Facts and Mysteries in Elementary Particle Physics, *World Scientific* (2003).

[3] Carlo Giunti and Chung W. Kim, Fundamentals of Neutrino Physics and Astrophysics, *Oxford University Press* (2007).

[4] Francis Halzen and Alan D. Martin, Quarks and Leptons: An Introductory Course in Modern Particle Physics, *John Wiley & Sons* (1984).

[5] David Griffiths, Introduction to Elementary Particles, *John Wiley & Sons, Inc.* (1987).

[6] B. P. Abbott et al., Observation of Gravitational Waves from a Binary Black Hole Merger, *Phys. Rev. Lett.* 116, 061102 (2016).

[7] *https://summerofhpc.prace-ri.eu/a-short-tour-of-lattice-qcd/*.

[8] Carsten Jensen, Controversy and Consensus: Nuclear Beta Decay 1911-1934, *Springer Basel AG* (2000).

[9] F. Reines and C. L. Cowan, Jr., Detection of the Free Neutrino, *Phys. Rev.* 92, 830 (1953).

[10] Kai Zuber, Neutrino Physics, Second Edition, *CRC Press* (2010).

[11] Raymond Davis, JR., Attempt to Detect the Antineutrinos from a Nuclear Reactor by the $Cl^{37}$ ($\bar{\nu}$, $e^-$) $A^{37}$ Reaction, *Phys. Rev.* 97, 766 (1955).

[12] C V K Baba, Survey of Experiments with Reactor Neutrinos, *Proc. Indian Natn. Sci. Acad.* 70, 53 (2004).

[13] Raymond Davis, Jr., Don S. Harmer and Kenneth C. Hoffman, Search for Neutrinos from the Sun, *Phys. Rev. Lett.* 20, 1205 (1968).

[14] M. Schwartz, Feasibility of Using High-Energy Neutrinos to Study the Weak Interactions, *Phys. Rev. Lett.* 4, 306 (1960).

[15] G. Danby et al., Observation of High-Energy Neutrino Reactions and the Existence of two kinds of Neutrinos, *Phys. Rev. Lett.* 9, 36 (1962).

[16] J. K. Bienlein et al., Spark Chamber Study of High-Energy Neutrino Interactions, *Phys. Lett.* 13, 80 (1964).

[17] DONUT collaboration: K. Kodama et al., Observation of tau neutrino interactions, *Phys. Lett. B* 504 (2001) 218.

[18] C.V. Achar et al., Detection of muons produced by cosmic ray neutrinos deep underground, *Phys. Lett.* 18, 196 (1965).

[19] F. Reines et al., Evidence for high-energy cosmic-ray neutrino interactions, *Phys. Rev. Lett.* 15, 429 (1965).

[20] R.S. Raghavan et al., Measuring the Global Radioactivity in the Earth by Multidetector Antineutrino Spectroscopy, *Phys. Rev. Lett.* 80, 635 (1998).

[21] U.F. Katz and Ch. Spiering, High-energy neutrino astrophysics: Status and perspectives, *Progress in Particle and Nuclear Physics* 67 (2012) 651.

[22] C. Patrignani et al., (Particle Data Group), *Chin. Phys. C* 40, 100001 (2016).

[23] D Indumathi, Physics from Neutrino Factories, *Proc. Indian Natn. Sci. Acad.* 70, 1 (2004) 79.

[24] D.S. Ayres et al., NOνA Proposal to Build a 30 Kiloton Off-Axis Detector to Study Neutrino Oscillations in the Fermilab NuMI Beamline, *arXiv:hep-ex/0503053*.

[25] LBNE collaboration: C. Adams et al., The Long-Baseline Neutrino Experiment: Exploring Fundamental Symmetries of the Universe, *arXiv:1307.7335 [hep-ex]*.

[26] Andre Rubbia, LAGUNA-LBNO: design of an underground neutrino observatory coupled to long baseline neutrino beams from CERN, 2013 *J. Phys.: Conf. Ser.* 408 012006.

[27] M. G. Aartsen et al., Letter of Intent: The Precision IceCube Next Generation Upgrade (PINGU), *arXiv:1401.2046 [physics.ins-det]*.

[28] Ulrich F. Katz for the KM3NeT Collaboration, The ORCA Option for KM3NeT, *arXiv:1402.1022 [astro-ph.IM]*.

[29] JUNO collaboration: Yu-Feng Li, Overview of the Jiangmen Underground Neutrino Observatory (JUNO), Int. J. Mod. Phys. Conf. Ser. 31 (2014) 1460300 [*arXiv:1402.6143* [physics.ins-det]].

[30] International Workshop on "RENO-50" toward Neutrino Mass Hierarchy, 2013, *http://home.kias.re.kr/MKG/h/reno50/*.

[31] K. Abe et al., Letter of Intent: The Hyper-Kamiokande Experiment – Detector Design and Physics Potential, *arXiv:1109.3262 [hep-ex]*.

[32] T. Ishida for the Hyper-Kamiokande working group, T2HK: J-PARC upgrade plan for future and beyond T2K, *arXiv:1311.5287 [hep-ex]*.

[33] ICAL collaboration: S. Ahmed et al., Physics Potential of the ICAL detector at the India-based Neutrino Observatory (INO), *arXiv:1505.07380*.

[34] D.N. Spergel et al., First Year Wilkinson Microwave Anisotropy Probe (WMAP) Observations: Determination of Cosmological Parameters, Astrophys. J. Suppl. 148 (2003) 175 [*arXiv:astro-ph/0302209*].

[35] Steen Hannestad, Neutrino physics from precision cosmology, Prog. Part. Nucl. Phys. 65 (2010) 185 [*arXiv:1007.0658* [hep-ph]].

[36] J. Lesgourgues and S. Pastor, Neutrino mass from Cosmology, Adv. High Energy Phys. (2012) 608515 [*arXiv:1212.6154* [hep-ph]].

[37] H.V. Klapdor-Kleingrothaus et al., Latest results from the HEIDELBERG-MOSCOW double beta decay experiment, *Eur. Phys. J. A* 12, 147 (2001).

[38] EXO collaboration: N. Ackerman et al., Observation of Two-Neutrino Double-Beta Decay in $^2$Xe with the EXO-200 Detector, *Phys. Rev. Lett.* 107, 212501 (2011).

[39] Ch. Kraus et al., Final results from phase II of the Mainz neutrino mass search in tritium $\beta$ decay, *Eur. Phys. J. C* 40, 447 (2005) *[hep-ex/0412056]*.

[40] KATRIN collaboration: J. Wolf et al., The KATRIN neutrino mass experiment, *Nucl. Instrum. Meth. A* 623, 442 (2010) *[arXiv:0810.3281 [physics.ins-det]]*.

[41] Kai Zuber, Non-accelerator neutrino physics, *IOP HEPP Meeting Brighton*, 22nd March, 2016.

[42] S. S. Kapoor, and V.S. Ramamurthy, Nuclear Radiation Detectors, *Wiley Eastern Limited* (1986).

[43] Fabio Sauli, Gaseous Radiation Detectors Fundamentals and Applications, *Cambridge University Press* (2014).

[44] Syed Naeem Ahmed, Physics & Engineering of Radiation Detection, *Second Edition, Elsevier* (2015).

[45] William R. Leo, Techniques for Nuclear and Particle Physics Experiments A How-to Approach, *Second Revised Edition, Springer International Edition* (1994).

[46] Glenn F. Knoll, Radiation Detection and Measurement, *Third Edition, John Wiley & Sons, Inc.* (2009).

[47] R. Santonico and R. Cardarelli, Development of Resistive Plate Counters, *Nucl. Instrum. and Meth.* 187 (1981) 377.

[48] Archana Sharma, Muon tracking and triggering with gaseous detectors and some applications, *Nucl. Instrum. and Meth. A* 666 (2012) 98.

[49] R. Cardarelli, R. Santonico, A. Di Biagio and A. Lucci, Progress in resistive plate counters, *Nucl. Instrum. and Meth. A* 263 (1988) 20.

[50] A. Jash, N. Majumdar, S. Mukhopadhyay and S. Chattopadhyay, Numerical studies on electrostatic field configuration of Resistive Plate Chambers for the INO-ICAL experiment, *JINST* 10 (2015) P11009.

[51] K. Raveendrababu, P.K. Behera and B. Satyanarayana, Effect of electrical properties of glass electrodes on the performance of RPC detectors for the INO-ICAL experiment, *JINST* 11 (2016) P08024.

[52] Satyanarayana Bheesette, Design and Characterisation Studies of Resistive Plate Chambers, Ph.D Thesis (2009).

[53] M. Salim, R. Hasan, N. Majumdar, S. Mukhopadhayay and B. Satyanarayana, Experimental and numerical studies on the effect of $SF_6$ in a glass RPC, *JINST* 7 (2012) P11019.

[54] Christian Lippmann, Detector Physics of Resistive Plate Chambers, Ph.D Thesis (2003).

[55] M. Yamaga et al., RPC systems for BELLE detector at KEKB, *Nucl. Instrum. and Meth. A* 456 (2000) 109.

[56] C. Gustavino, A. Candela, M. De Deo, M. D'Incecco and R. Moro, Performance of glass RPC operated in streamer mode with four-fold gas mixtures containing $SF_6$, *Nucl. Instrum. and Meth. A* 517 (2004) 101.

[57] P. Fonte, Applications and New Developments in Resistive Plate Chambers, *IEEE Trans. Nucl. Sci.* 49 (2002) 881.

[58] M. Abbrescia et al., Recent results and developments on double-gap RPCs for CMS, *Nucl. Instrum. and Meth. A* 409 (1998) 43.

[59] E. Cerron Zeballos et al., A new type of resistive plate chamber: The multigap RPC, *Nucl. Instrum. and Meth. A* 374 (1996) 132.

[60] Saikat Biswas, Development of High Resolution Gas Filled Detector for High Energy Physics Experiments, Ph.D Thesis (2010).

[61] S. Narita , Y. Hoshi, K. Neichi and A. Yamaguchi, Construction and performance of multigap RPC in streamer and avalanche modes, *Nucl. Instrum. and Meth. A* 602 (2009) 814.

[62] S. An et al., A 20 ps timing device–A Multigap Resistive Plate Chamber with 24 gas gaps, *Nucl. Instrum. and Meth. A* 594 (2008) 39.

[63] S. Narita et al., Time properties of multigap RPC with glass electrodes operated in streamer and avalanche modes, *Nucl. Instrum. and Meth. A* 661 (2012) S206.

[64] P. Fonte, A. Smirnitski and M.C.S. Williams, A new high-resolution TOF technology, *Nucl. Instrum. and Meth. A* 443 (2000) 201.

[65] M. Fontana et al., Performance of the ALICE muon trigger RPCs during LHC Run I, *JINST* 9 (2014) C08019.

[66] G. Bruno, Resistive plate chambers in running and future experiments, *Eur. Phys. J. C* 33 (2004) s1032.

[67] P. Fonte et al., High-resolution RPCs for large TOF systems, *Nucl. Instrum. and Meth. A* 449 (2000) 295.

[68] A. Blanco et al., Development of large area and of position-sensitive timing RPCs, *Nucl. Instrum. and Meth. A* 478 (2002) 170.

[69] M.C.S. Williams, The multigap RPC: the time-of-flight detector for the ALICE experiment, *Nucl. Instrum. and Meth. A* 478 (2002) 183.

[70] Jose Lamas V, The multigap resistive plate chamber as time-of-flight detector for the STAR experiment at RHIC, *Rev. Inv. Fis.* 5 (2002) 44.

[71] Z. Wu et al., First results of the new endcap TOF commissioning at BESIII, *JINST* 11 (2016) C07005.

[72] K. Raveendrababu, P.K. Behera, B. Satyanarayana and J. Sadiq, Study of glass properties as electrode for RPC, *JINST* 11 (2016) C07007.

[73] A. C. P. Galvao, A. C. M. Farias and J. U. L. Mendes, Characterization of waste of soda-lime glass generated from lapping process to reuse as filler in composite materials as thermal insulation, *Ceramica* 61 (2015) 367.

[74] C. Lu, RPC electrode material study, *Nucl. Instr. and Meth. A* 602 (2009) 761.

[75] G. Aielli et al., Electrical conduction properties of phenolic–melaminic laminates, *Nucl. Instrum. and Meth. A* 533 (2004) 86.

[76] T. Dai et al., Low resistance bakelite RPC study for high rate working capability, *JINST* 9 (2014) C11013.

[77] David J. Griffiths, Introduction to Electrodynamics, *3rd Edition, Prentice-Hall of India Private Limited* (2006).

[78] C. H. Hsieh et al., Correlation between dielectric constant and chemical structure of sodium silicate glasses, *J. Appl. Phys.* 80 (1996) 1704.

[79] Horst Scholze, Glass: Nature, Structure, and Properties, *Springer-Verlag* (1991).

[80] Maxim Titov, Radiation damage and long-term aging in gas detectors, ICFA Instrum. Bull. 26 (2004) 002 [*arXiv:physics/0403055*]].

[81] Paul Garrett, Lecture 21: Absorption and Transmission of light and the Beer-Lambert Law, *www.physics.uoguelph.ca/~pgarrett/Teaching.html*.

[82] Emmanuel Rosencher and Borge Vinter, Optoelectronics, *Cambridge University Press* (2004).

[83] Thomas K. Gaisser, Cosmic Rays and Particle Physics, *Cambridge University Press* (1990).

[84] S. Cecchini and M. Spurio, Atmospheric muons: experimental aspects, *arXiv:1208.1171*.

[85] *www.ibs.fr*.

[86] *https://en.wikipedia.org/wiki/Scintillation_counter*.

[87] M. Bhuyan et al., Development of 2 m × 2 m size glass RPCs for INO, *Nucl. Instrum. and Meth. A* 661 (2012) S64.

[88] M.R. Bhuyan et al., Preliminary results on optimisation of gas flow rate for ICAL RPCs, *Nucl. Instrum. and Meth. A* 736 (2014) 135.

[89] M. Morales, C. Pecharroman, G. Mata-Osoro, L.A Diaz and J.A. Garzon, Conductivity and charge depletion aging of resistive electrodes for high rate RPCs, *JINST* 8 (2013) P01022.

[90] W. Riegler and C. Lippmann, Detailed models for timing and efficiency in resistive plate chambers, *Nucl. Instrum. and Meth. A* 508 (2003) 14.

[91] Tapasi Ghosh and Subhasis Chattopadhyay, A Monte Carlo simulation to study the effect of surface roughness on the performance of RPC, *Nucl. Instrum. and Meth. A* 661 (2012) S177.

[92] H. Sakai, H Sakaue, Y Teramoto, E Nakano and T Takahashi, Study of the effect of water vapor on a resistive plate chamber with glass electrodes, *Nucl. Instrum. and Meth. A* 484 (2002) 153.

[93] T. Kubo, H Sakaue, Y Teramoto, E Nakano and T Takahashi, Study of the effect of water vapor on a glass RPC with and without freon, *Nucl. Instrum. and Meth. A* 508 (2003) 50.

[94] A. Candela et al., Ageing and recovering of glass RPC, *Nucl. Instrum. and Meth. A* 533 (2004) 116.

[95] K. Raveendrababu, P. K. Behera, B. Satyanarayana, S. Mukhopadhayay and N. Majumdar, Effect of water vapor on the performance of glass RPCs in avalanche mode operation, *JINST* 11 (2016) C08001.

[96] A. Chatterjee et al., A simulations study of the muon response of the Iron Calorimeter detector at the India-based Neutrino Observatory, *JINST* 9 (2014) P07001.

[97] S. Agostinelli et al., Geant4—a simulation toolkit, *Nucl. Instrum. and Meth. A* 506 (2003) 250.

[98] Tarak Thakore, Anushree Ghosh, Sandhya Choubey and Amol Dighe, The reach of INO for atmospheric neutrino oscillation parameters, *JHEP* 05 (2013) 058 *[arXiv:1303.2534]*.